Experimental techniques for the study of the CMB anisotropy and polarization, and the Sunyaev-Zel'dovich effect.

by
Philippe Rossinot

A thesis submitted to the
University of Wales
for the degree of
Doctor of Philosophy

April, 2004

ProQuest LLC
789 East Eisenhower Parkway
P.O. Box 1346
Ann Arbor, MI 48106-1346

DECLARATION

This work has not previously been accepted in substance for any degree and is not being concurrently submitted in candidature for any degree.

Signed .....(candidate)
Date.....20 August 04.....

STATEMENT 1

This thesis is the result of my own investigations, except where otherwise stated. Other sources are acknowledged by footnotes giving explicit references. A bibliography is appended.

Signed .....(candidate)
Date.....20 August 04.....

STATEMENT 2

I hereby give consent for my thesis, if accepted, to be available for photocopying and for inter-library loan, and for the title and summary to be made available to outside organisations.

Signed .....(candidate)
Date.....20 August 04.....


CARDIFF UNIVERSITY
2 SEP 2004
PRIFYSGOL CAERDYDD

Abstract

Observational cosmology is one of the most active fields in modern astrophysics. Following the discovery of the microwave background by Penzias and Wilson (Penzias & Wilson 1965) and the success of COBE-DMR, research groups throughout the world have pursued the study of the primary and secondary anisotropies in the cosmic microwave background (CMB). Instrumentation designed specifically for these studies have resulted in ever more sensitive detections of the CMB fingerprints.

This thesis describes work on three bolometric instruments operating at cryogenic temperatures that have been designed to study the CMB. We present a design study with initial assembly and testing on the first of these, a new type of instrument - the millimetre-wave bolometric interferometer prototype (MBI-P). This instrument combines two well-known techniques: bolometric detection and interferometry, and could be used to observe the CMB on small angular scales with high sensitivity. Our investigation includes the design of the optics, cryogenics and mechanics of the prototype. We present a prototype that has a clear potential to demonstrate the technology involved.

We then describe our contribution to Polatron, a bolometric polarimeter designed to study the polarization of the CMB. We assess its performance by analysing the noise coupling between the mechanical cryocooler and the bolometers. We demonstrate that Polatron is not able to fulfil the technical requirements in terms of sensitivity, necessary to achieve its science goal.

Finally, we discuss the thermal behaviour of the cold-amplifier stage of Bolocam - a millimetre-wave bolometric camera, now operating at the Caltech sub-millimetre observatory (CSO), one of whose main scientific objective is the study of the CMB secondary signatures. Having modified the cryogenic design, we measure and analyse its performance which has significantly lowered the cryogen consumption.

Acknowledgements

I would first like to thank my advisor Lucio Piccirillo and Walter Gear for giving me the opportunity to be the first graduate student in the Astrophysics Instrumentation Group at Cardiff University. I am also very grateful to Andrew Lange for welcoming me to Caltech to work on Polatron after my two years spent in Wales working on MBI. My thanks also go to Peter Ade and Andrew for their supports and their encouragements during this period of time.

During my work on Polatron – which some would say was cursed - I had fantastic colleagues, namely Viktor Hristov, Georges and Adriana Sirbi, whose expertise and abilities I certainly benefited from, as well as their dedication to the Friday pub visits. After many attempts at exorcising the curse of Polatron, Sunil Golwala offered me the opportunity to become involved in Bolocam. What a novel pleasure it was to participate in an experiment that actually worked! For that and for offering me a position after my graduation, (no nepotism involved) I am very grateful to him.

During the time I spent in Cardiff and Caltech I was fortunate to meet friendly people who have made my stay here, and there, very enjoyable. In particular I thank 'mon pote' Olivier and 'my dude' Douglas for starting a life-long friendship (although I think Douglas isn't sure about this anymore) and helping me deal with my thesis up to the very last minute. A special note at this point should be made to acknowledge the instigation of what is now the institution known as BBT, or Balcony Beer Time. This 4pm daily occurrence during the marathon Bolocam observing runs on Mauna Kea kept Douglas and I from going completely insane. A tradition I will continue and encourage others to join, we just have to find some decent European beer; of course it was the drunken Scotsman's idea!

My thesis owes many thanks to Kate Isaac, who corrected my writing. I am sincerely grateful to her for the long hours she spent interpreting my French way of writing English.

These acknowledgements would not be complete without expressing my gratitude to my family for their supports as well as my friends JC, Vince, Denis and Jerome for always being there for me. Special thanks to Mimine, the only person I know who kept to her New Year's resolutions.

Contents

List of figures

List of tables

List of pictures

Chapter 1 Introduction

In the early nineties, measurement on large angular scales of the temperature anisotropies of the cosmic microwave background (CMB) by the DMR-COBE satellite (Smoot et al., 1992) marked the beginning of the golden age in observational cosmology. The development of state-of-the-art instrumentation boomed in astrophysics groups throughout the world, pushing the limits of detection even further. Measuring the power spectrum of the CMB temperature anisotropies not only enable us to learn about the history of the Universe but also about its contents, its size and fate, bringing new insights into the formation of large scale structures. In this chapter, we first give a general cosmological overview of the formation of the fossil radiation. Secondly, the features in the CMB power spectrum are discussed in more details, highlighting how they relate to important cosmological parameters. In the third section, we focus on observational concepts necessary to understand the specific instrumentation involved; this part will also briefly review major legacy or planned astronomical instruments and will clarify the need for new instrumentation. Finally, we outline the instrumentation work presented in this thesis.

References to this chapter (unless specified otherwise) can be found in reviews from Hu et al. (1997), Kosowsky (2002) or White et al. (1994) on CMB anisotropy, Kosowsky (1999) on CMB polarization, and Birkinshaw (1999) on the Sunyaev-Zel'dovich effect.

1.1 CMB anisotropy

As cosmologists and particle physicists trace back in time the history of the Universe, they inevitably encounter extreme conditions almost impossible to re-create and extremely complex to simulate. As we look further back in time, the denser, hotter and smaller the Universe is expected to be. At very early time, the Universe consisted of a soup of quarks and anti-quarks in continuous annihilation-materialization. However, at some point in this dense medium

flooded with very energetic photons, the equilibrium between annihilation and materialization was slightly broken, enough to trigger interactions that would later lead to the creation of matter. As the Universe expanded and cooled down, the quarks no longer had enough energy to exist on their own, and grouped into hadrons. Over a very short interval, the major constituents of the Universe became baryons (e.g. protons, and neutrons), leptons (e.g. electrons, neutrinos and their antiparticles) and photons, all of which being governed by the gravitation, electromagnetic, weak and strong interactions. Within minute after the Big Bang, the disequilibrium between neutron and proton favoured the creation of light nuclei, with a mixture of 75% of hydrogen, 25% of helium as well as a small proportion of their isotopes and lithium (Gawiser & Silk 2000). The medium was very dense and dominated by radiation. Under these conditions, photons were scattered off free electrons, making the early universe very opaque. When the Universe had cooled to below 3000 Kelvin, a new era in the history of the universe began, known as decoupling. At this point, electron's energy was low enough to bound with nuclei; the first hydrogen atoms were able to form, and in the absence of being scattered off electrons, photons freely escaped from the plasma after a very last scattering; this is known as the recombination.

Photons travelled from this last surface scattering (LSS) at a redshift of ~1089, without encountering any obstacles, carrying the imprints of density perturbations at the LSS. These photons, whose wavelength has stretched to the microwaves with the expansion, constitute the cosmic microwave background we observe today. Density perturbations at the time of recombination are seen today as minute temperature anisotropies, at levels of a part in 10^5, in the CMB spectrum. The study of power spectrum of the CMB temperature anisotropies can test inflationary models of structure formation. In particular it provides observational information on important key cosmological parameters such as the Hubble constant, H_0 – and so indirectly the age of the universe, the total density of the universe, Ω_0, the physical density of the constituents in the early universe such as baryons, $\Omega_b h^2$, matter $\Omega_m h^2$, dark energy Ω_Λ, the size of the sound horizon and the re-ionization epoch. The exciting goal is to constrain these parameters

accurately enough to obtain a unique cosmological model. In this way, the Universe formation, evolution and fate can be statistically determined based on observations.

1.2 CMB power spectrum

1.2.1 Density perturbation

In a cold dark matter (CDM) model scenario, quantum density fluctuations expanded into cosmic sizes faster than the speed of light during the inflation[1], resulting in scale-invariant density disturbances. Matter, under gravitational pressure, agglomerated on very local scales. Radiation pressure worked in the opposite sense, pushing the particles out of the potential wells formed under gravity. The competing forces of gravitational compression and radiation pressure resulted in oscillation in the primeval radiation-baryon fluid, evolving with the expansion. Their phases and amplitudes froze at the last scattering surface (LSS) when the matter decoupled from the radiation, giving an acoustical nature to the primordial fluctuations, characterised by a fundamental mode and corresponding harmonics, a concept illustrated in Figure 1.1. On small angular scales, the power spectrum of the CMB anisotropies is shaped by the scale-size of the density perturbation that evolved from the inflation to the LSS. To contribute to the CMB power spectrum, they must be almost equal to or smaller than the size of the sound horizon, since perturbations on scales larger than the horizon will not appear in the spectrum since those perturbations have not had the time to compress (or rarefy) since the Big Bang. Regions of compression (more dense) and rarefaction at this epoch represent hot and cold spots respectively (Hu, Sugiyama & Silk 1997).

Having established the overall features of the CMB power spectrum (cf. illustration of the main concepts in Figure 1.1), we now investigate how constraints on the cosmological parameters can be extracted from it.

[1] The inflation is a short period of time lasting from 10^{-35} to 10^{-32} seconds after the singularity, when the universe is believed to have expanded dramatically.

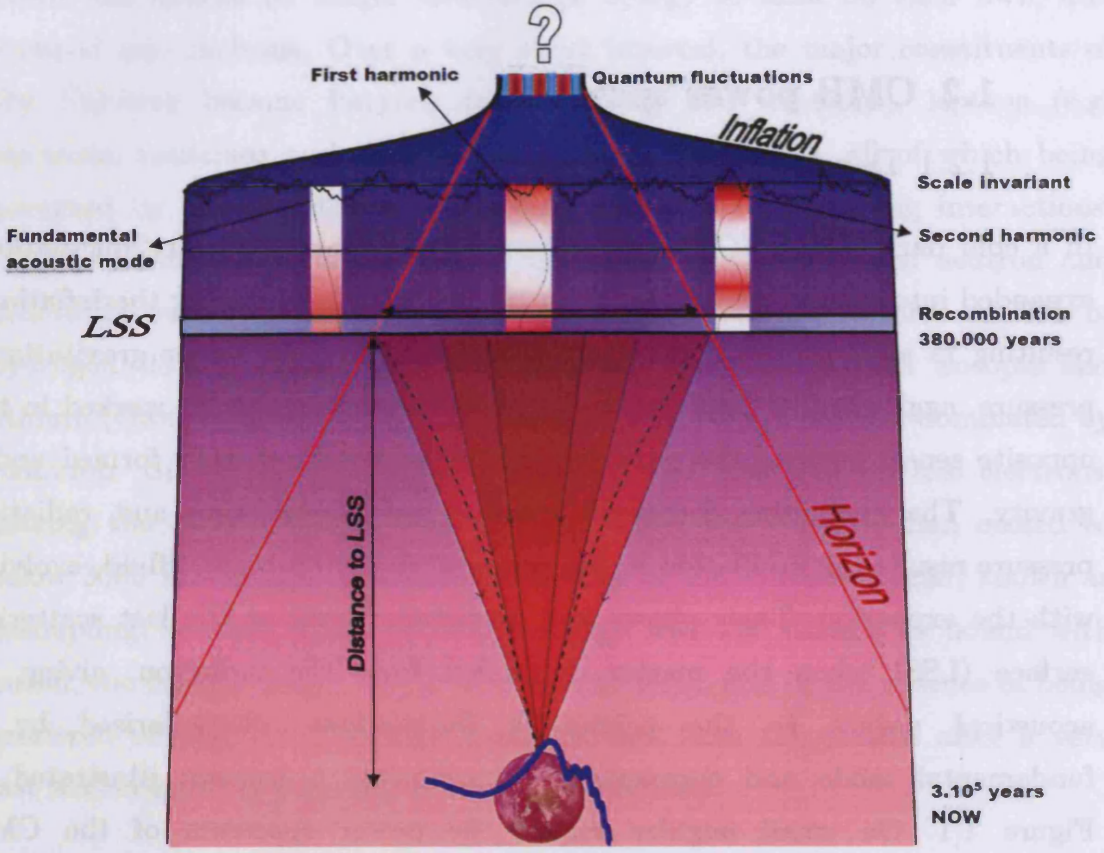

Figure 1.1: Evolution of CMB fluctuations.
Quantum fluctuations in the very early Universe expanded to cosmic sizes during the *inflation*, resulting in density disturbances of equal magnitudes and phases on all scales. Radiation tightly coupled to matter, constituted a plasma that cooled with the expansion. Perturbations in this gas - in the form of compressions and rarefactions – behave like sound waves between the period of inflation and the *last scattering surface* (LSS) , characterised by a fundamental and corresponding harmonics. As the Universe expanded, the temperature sufficiently cooled down for protons to capture electrons and form the first atoms (*Recombination*). Photons decoupled from matter and freely travelled towards us, carrying the imprints of the early Universe that froze at the LSS, 380,000 years after the initial singularity (*Decoupling*). Redshifted into the millimetre region, these photons constitute the *cosmic microwave background* (CMB) and reveal the Universe formation and fate from their temperature anisotropies *power spectrum* (shown in red).

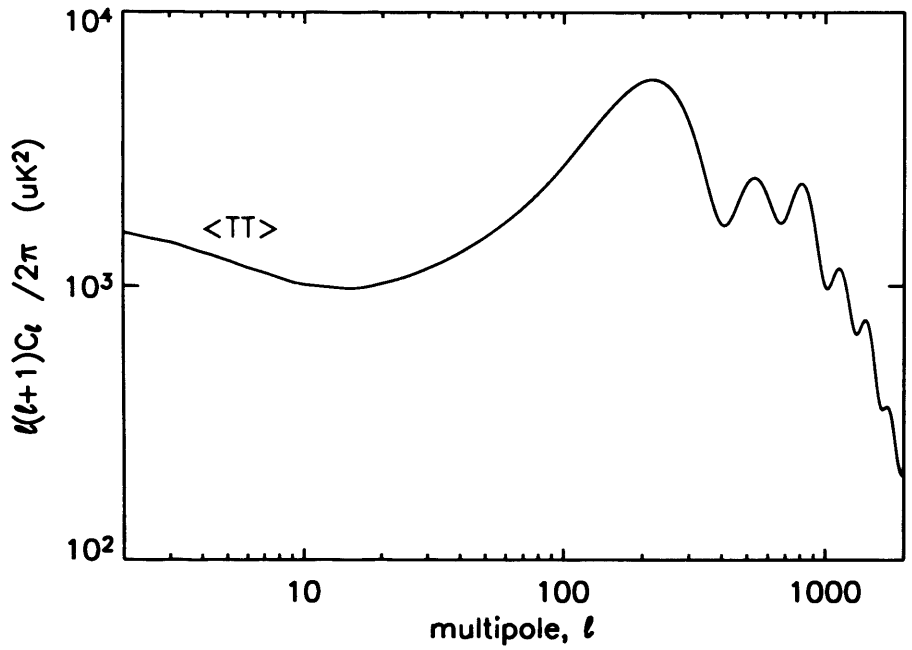

Figure 1.2: CMB temperature power spectrum <TT>.
This plot is based on cosmological parameters from WMAP (cf. Table 1.1)

Shown in Figure 1.2 is the density power spectrum of the CMB temperature anisotropy. Features highlighted above, provide very strong evidences for an inflationary CDM model. The positions of the peaks are relevant to the curvature of the universe space-time, whereas their relative amplitudes give the content of matter in the early universe. The position of the first acoustic peak relates to the size of the horizon at LSS. Thus, it plays an important role in determining both the curvature and the total density, Ω_0, of the Universe. The position of the first peak is consistent with an (almost) spatially flat Universe of total energy density close to critical, or $\Omega_m + \Omega_\Lambda = 1$. It has been located at an angular scale of $\ell \sim 200$ by many experiments (cf. §1.3.3), more recently by WMAP[1] (Bennett et al. 2003).

However, the possible mismatch between the distances sound and CMB photons have travelled since recombination means that it is not possible to determine the Hubble constant from the study of the 1st compression peak alone. This reflects the lack of information on the physical density of dark matter compared with $\Omega_{rad}h^2$. This is important, as an inability to constrain H_0 prevents the determination of the curvature of the Universe with sufficient

[1] Wilkinson Microwave Anisotropy Probe

accuracy to differentiate between cosmological models. Higher peaks such as the second and third one (cf. Figure 1.1), need to be studied. The existence of other peaks located at harmonics of the fundamental is an evidence for inflationary acoustic oscillations. Both their positions and amplitudes are needed to constrain cosmological parameters. The relative heights of the peaks reflect the amount of baryons and therefore help to constrain $\Omega_b h^2$ and $\Omega_m h^2$. An excess of baryons would have loaded down the photon-baryon oscillations; more baryons would enhance odd peaks (i.e. compressions) over even peaks (rarefactions). From determining the amount of baryons, information on the speed of sound, and thus the distance sound travelled by recombination, are also available – more baryons would slow down the speed of sound, and thus the distance sound would have travelled by recombination.

Unlike the fundamental compression that was enhanced at recombination, the first harmonic (with half the fundamental wavelength) was caught in an opposite phase where gravity (compressing the plasma) opposed gas pressure (expanding the plasma). So the temperature variations as seen today resulting from harmonics are smaller than those resulting from fundamental perturbations. Since both dark matter and ordinary matter enhance gravitational pull but only the baryons are affected by the acoustic compression and rarefaction, the comparisons of the heights of both the first and second peaks can be used to determine the energy density ratio of dark matter to radiation. Raising the amount of dark matter would increase the height of the peaks. In contrast, lowering the amount of dark matter counteracts the effects of an excess in baryons.

Higher peaks probe even smaller angular scales and so provide good consistency checks (Hu & White 1997a). When fluctuations size-scales were comparable to the mean-free path of CMB photons during recombination, photons from hot and cold regions smeared out (Silk 1967). As a consequence, the acoustic peaks at high ℓ are exponentially damped on distance-scales smaller than the distance photon travelled during recombination. A significant damping would be indicative of an excess in baryons. The measurement of the damping tail, serves as a check in consistency since an increase in $\Omega_b h^2$ would shift the tail peaks to higher multipole, whereas an increase in $\Omega_m h^2$ would shift the damping tail peaks to lower ones.

After recombination, photons issued from denser regions lost more energy by climbing the gravitational potential wells than photons released from less dense regions. Consequently, as CMB photons travelled from the LSS towards us, they are blue-shifted as they enter gravitational potentials, before being red-shifted (referred to as the Sachs-Wolfe effect) upon leaving them (Sachs & Wolfe 1967, White & Hu 1997). In a universe not baryon-dominated gravitational wells evolve, or deepen, with time as the universe expanded. When observed today, the two effects no longer cancel, resulting in a net redshift of the radiation. Imprinted in the CMB temperature spectrum at large angular scale, this physical process is known as the integrated Sachs-Wolfe (ISW) effect. Although this could be used in theory to study dark energy, statistical fluctuation in the CMB data based on the study of a single universe limits the interest of the ISW effect. The ISW effect is seen in the temperature CMB spectrum at larger scales than the first peak.

1.2.2 Polarization

We discussed previously the particular features of the CMB autocorrelation temperature anisotropy spectrum $\langle TT \rangle$, given explicitly in equation (1.1) in section 1.3.1. However, the CMB power spectrum is also expected to feature polarized signatures arising from the presence of velocity gradients in the baryon-photon fluid. A detailed description of this physical process can be found in Kosowsky's review (1999). Near decoupling, velocity gradients across the mean free path of the CMB photons induced a quadrupole in the density (scalar) perturbations (velocity alone would produce just a dipole) which, when associated with Thomson scattering, generated linear polarization as shown in Figure 1.3. On scales larger than the thickness of the LSS, we expect the quadrupole (i.e. the polarization component) to couple more strongly to the dipole component than to the density.

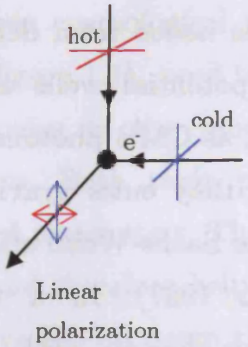

Figure 1.3: Thomson scattering.
A net linear polarization results from photons in a quadrupole anisotropy being scattered off an electron.

The corresponding Doppler shift from the peculiar velocity of the baryon-photon fluid imprints peaks in the E-mode[1] autocorrelation spectrum $\langle EE \rangle$ out of phase with those of the $\langle TT \rangle$ spectrum, in which the higher peak corresponds to the diffusion scale at $\ell \sim 1000$. This free path is an important concept as it models the polarization spectrum. Since initially Thomson scattering only occurred in a finite space-time region (LSS), we expect the polarized signal to be at a level of few micro-Kelvin, less than 10% of the anisotropy. For the polarization to be observable today, the right amount of scatterers and low optical depth was necessary to avoid smearing out the direction of polarization. Moreover, no polarized signal is seen on larger scales since the quadrupole would not have occurred for structures larger than the diffusion scale. Therefore, one may not expect any polarized signal on large scale. This holds unless re-ionization of the hydrogen by the first stars contributed to the Thomson scattering of the CMB photons at a much later time than the LSS. Such a mechanism would translate to a peak at low ℓ in the $\langle EE \rangle$ power spectrum since the diffusion scale would have increased considerably across the entire visible Universe. This re-ionization signature, due to the low scattering probability of the CMB photons is expected to be very small, of the level of a tenth of a micro-Kelvin as measured by WMAP (cf. section 1.3.3). Acoustic peaks in the polarization power spectrum would

[1] Polarization pattern in which the orientation of polarization vectors are radial or tangential around cold and hot spots.

give information on the width of the LSS at $\ell \sim 1089$ and information about re-ionization of the hydrogen from the formation of the first stars.

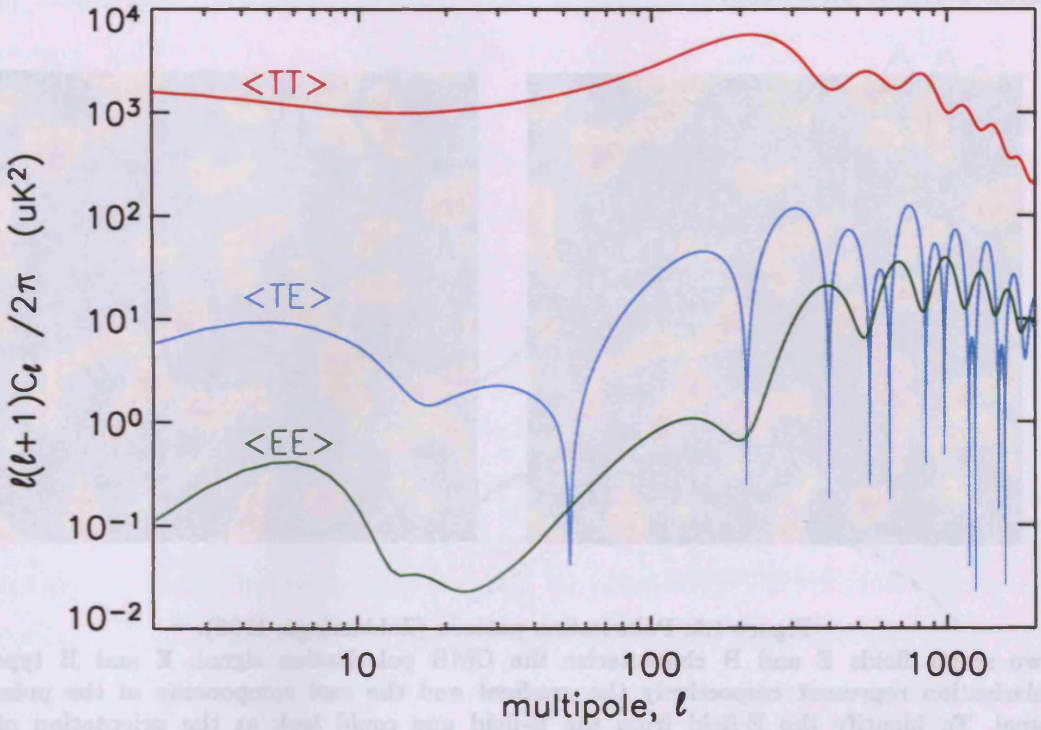

Figure 1.4: CMB <TT>, <EE>, <TE> power spectra.
These plots are based on cosmological parameters from WMAP (cf. Table 1.1)

We can also define a correlation spectrum between scalar density perturbation $\langle TT \rangle$ and the polarization power spectrum $\langle EE \rangle$, known as the cross-correlation $\langle TE \rangle$ as shown in Figure 1.4. Indeed, such correlation is expected since the E-mode is modulated in the direction of (or perpendicular to) its axis of polarization. As we will discuss in section 1.3.3, WMAP has been able to put an upper limit of the re-ionization period of ~180 million years after the initial singularity, using this $\langle TE \rangle$ spectrum (Kogut et al. 2003).

In addition to scalar density perturbations, tensor perturbations induced by gravitational waves evolving in the plasma are expected to have polarized CMB photons. Gravity waves induced anisotropic stretches in the space and produced a quadrupole in the temperature field. Unlike the scalar perturbations, tensor perturbations are modulated by primordial plane-waves and do not posses any symmetry under rotation or reflection creating E-mode

and B-mode [1] polarization patterns, as shown in Figure 1.5 (Seljak & Zaldarriaga 1997, Kamionkowski et al. 1997). The B-mode signal is expected to be as faint as tenths of a micro-Kelvin, on a very small range of angular scales centred on $\ell \sim 100$.

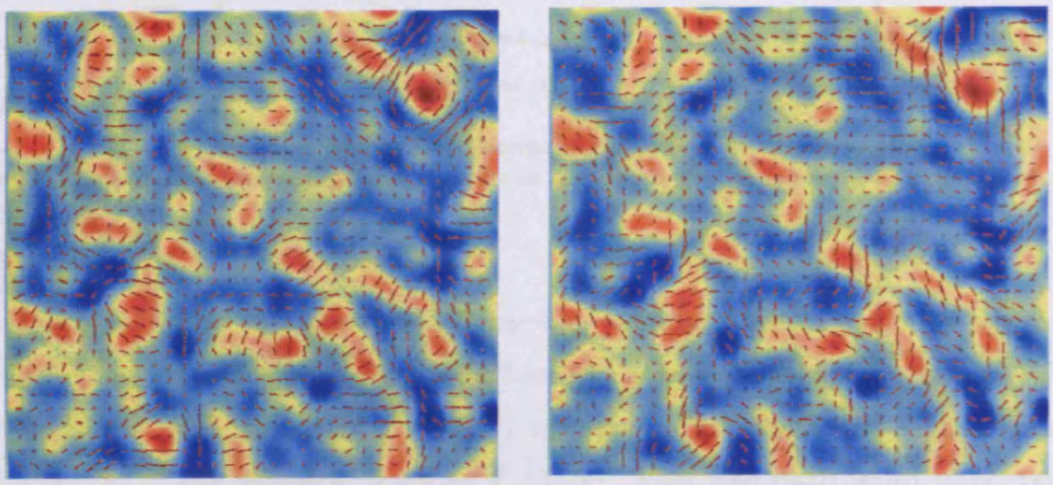

Figure 1.5: Polarization pattern (Zaldarriaga, 1998).
Two scalar fields E and B characterize the CMB polarization signal. E and B types of polarization represent respectively the gradient and the curl components of the polarized signal. To identify the E-field from the B-field one could look at the orientation of the polarization pattern, as shown on the left (E-field) and the right (B-field).

On scales larger than $\ell \sim 100$, the amplitude of the gravitational wave that entered the horizon before the last scattering decreased as the universe expanded. The amplitude autocorrelation power spectrum $\langle BB \rangle$, plotted in Figure 1.6 (dashed-blue line), depends on the ratio between the power in the gravitational wave and density modes, i.e. the tensor to scalar ratio $r = T/S$. WMAP gave an upper limit at 0.90 with 95% CL (Bennett et al. 2003). Gravitational waves are the only process which can form B-mode polarization in the CMB photons in the early universe up to recombination. However, later in the universe history, when large-scale structure has formed, the gravity fields in massive galaxy clusters are expected to deflect the trajectory of the CMB photons. This gravitational lensing alters the direction from which the

[1] Polarization pattern in which the polarization vectors are oriented at 45° to the radial around cold and hot spots.

photons appear to come from, as well as their polarization vector field so that an E-field becomes B polarized.

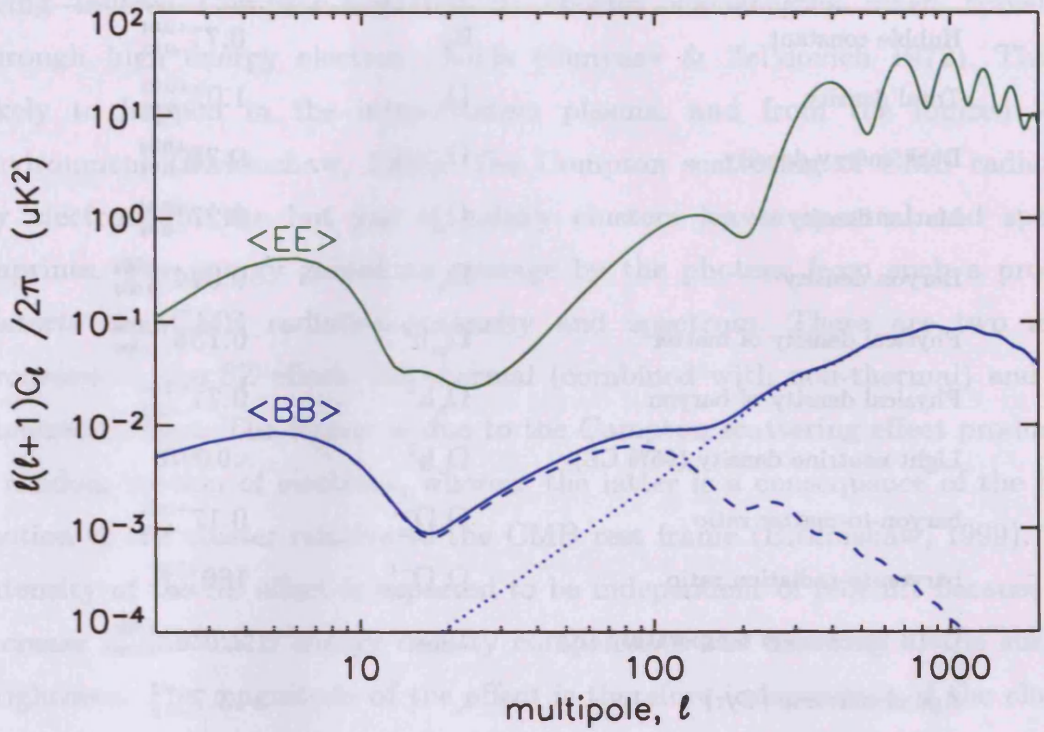

Figure 1.6: Polarization temperature power spectra.
These plots show the linear polarization spectra (green) and the B-modes generated by gravitational lensing (dotted line) and gravitational wave (dashed line). The total B-mode contribution is shown in plain blue. Those plots are based on cosmological parameters from WMAP first year of data in (cf. Table 1.1), with r=0.1.

The power spectrum predicted for such a signal in the polarization of the CMB is shown by dotted-blue line in Figure 1.6. A measurement of the gravitational wave would provide strong evidence of an inflationary scenario (Hu 2002, and Polnarev 1985) as well as an important consistency check of acoustics features.

Table 1.1: Cosmological parameter discussed in this thesis. Values are from WMAP 1-year data (Bennett et al., 2003)

Description	Symbol	Value
Hubble constant	H_0	$0.71^{+0.04}_{-0.03}$
Total density	Ω_0	$1.02^{+0.02}_{-0.02}$
Dark energy density	Ω_Λ	$0.73^{+0.04}_{-0.04}$
Matter density	Ω_m	$0.27^{+0.04}_{-0.04}$
Baryon density	Ω_b	$0.044^{+0.004}_{-0.004}$
Physical density of matter	$\Omega_m h^2$	$0.135^{+0.008}_{-0.009}$
Physical density of baryon	$\Omega_b h^2$	$0.71^{+0.04}_{-0.03}$
Light neutrino density (95% CL)	$\Omega_\nu h^2$	<0.0076
baryon-to-matter ratio	$\Omega_b \Omega_m^{-1}$	$0.17^{+0.01}_{-0.01}$
baryon-to-radiation ratio	$\Omega_b \Omega_{rad}^{-1}$	180^{+220}_{-80}
CMB black-body temperature (K)	T_{CMB}	$2.725^{+0.002}_{-0.002}$
Age of universe (Gyr)	t_o	$13.7^{+0.2}_{-0.2}$
Age at decoupling (kyr)	t_d	379^{+8}_{-7}
Age at re-ionization (95%CL,Myr)	t_r	180^{+220}_{-80}
Decoupling interval (kyr)	Δt_d	118^{+3}_{-2}
Redshift at matter-radiation equality	z_{eq}	3233^{+194}_{-210}
Redshift of re-ionization (95% CL)	z_r	20^{+10}_{-9}
Redshift at decoupling	z_{dec}	1089^{+1}_{-1}
Thickness of decoupling	Δz_{dec}	195^{+2}_{-2}
Ttensor to scalar ratio	$_r$	0.1
Sound horizon (°)	θ_A	$0.598^{+0.002}_{-0.002}$
Sound horizon (Mpc)	r_s	147^{+2}_{-2}
Acoustic scale	$_A$	301^{+1}_{-1}

1.2.3 The Sunyaev-Zel'dovich effect

The Sunyaev-Zel'dovich effect (SZE) is a result of low energy CMB photons being inverse Compton-scattered to shorter wavelengths when travelling through high energy electron clouds (Sunyaev & Zel'dovich 1972). This is likely to happen in the intra-clusters plasma, and from the ionized local environment (Birkinshaw, 1999). The Compton scattering of CMB radiation by electrons in the hot gas of galaxy clusters leaves spectral and spatial imprints. The energy gained on average by the photons from such a process distorts the CMB radiation intensity and spectrum. There are two main processes in the SZ effect: the thermal (combined with non-thermal) and the kinematic effect. The former is due to the Compton scattering effect producing a random motion of electrons, whereas the latter is a consequence of the bulk motion of the cluster relative to the CMB rest frame (Birkinshaw, 1999). The intensity of the SZ effect is expected to be independent of redshift because the increase in the CMB energy density compensates the dimming of the surface brightness. The magnitude of the effect is therefore independent of the cluster distance, and depends principally from the properties of the cluster gas. The thermal effect shortens the CMB photons wavelength, increasing the CMB radiation intensity at shorter wavelengths and decreasing it at longer ones. On the other hand, the kinematic (or velocity) effect would give a structure to the cosmic photons, annihilating its isotropic characteristic. This is illustrated in Figure 1.7 below. Since the number of photons in this process is conserved, the spectrum of the CMB photons alters, presenting a decrement in the CMB temperature between 10 GHz and 200 GHz and an increment between 200 GHz and 1000 GHz (Carlstrom et al. 2002).

Associated with X-ray observations, measurement of the thermal effect in clusters of galaxies can be used to probe cosmological parameters such as the Hubble constant, and the baryon mass fraction of the X-ray emitting gas, as well as providing information on the formation and evolution of large-scale structures. Measurement of the kinetic SZ effect through the radial cluster velocity can provide information in the evolution of clusters. Cluster counts in blank surveys can lead to evaluation of the matter density in the Universe.

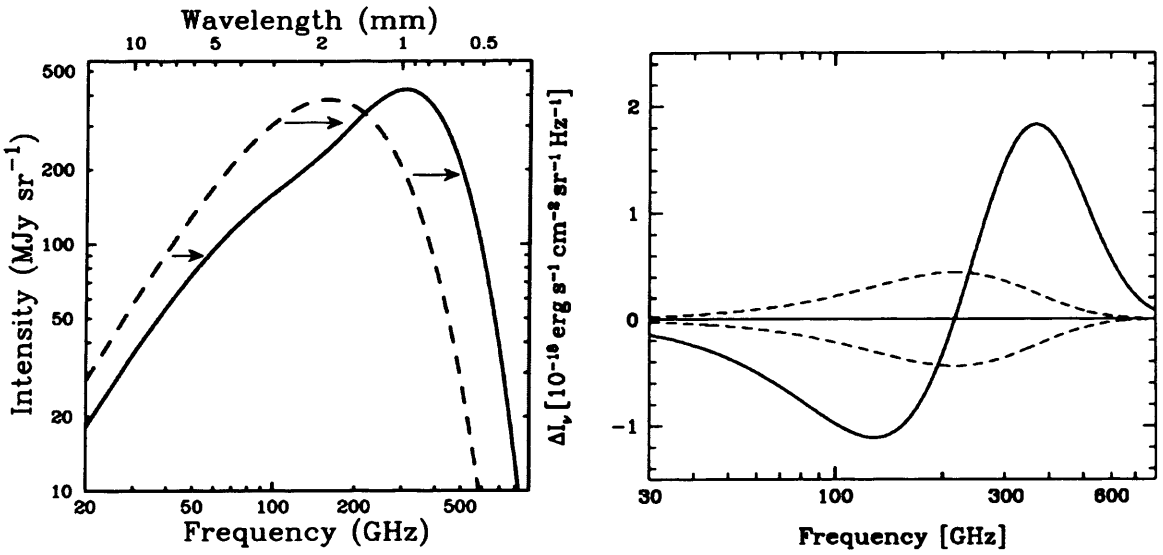

Figure 1.7: The SZ effect on CMB spectrum.
(Left) SZE intensity shift. The lines showed are the spectrum of the CMB before (dotted-line) and after (plain) being scattered by the hot gas in a cluster. (Right) Intensity change to the CMB spectrum caused by the SZ effect. The black line represents the thermal effect with a null at 218 GHz; the dotted-line is the kinematic SZ effect. (Carlstrom et al. 2002).

1.3 Observation of the CMB anisotropy

1.3.1 Formalism

The CMB fluctuations are commonly predicted and analysed statistically based on temperature differences $\Delta T(\vec{x}_i)/T$, where $\vec{x}_i$ is a polar position vector on the celestial sphere. The two-point correlation function between two observations $\vec{x}_i$ and $\vec{x}_j$ on the sky is given by:

$$C_{i,j}^{CMB}(\vec{x}_{i,j}) = \left\langle \frac{\Delta T(\vec{x}_i)}{T} \frac{\Delta T(\vec{x}_j)}{T} \right\rangle \tag{1.1}$$

The temperature anisotropy in one direction on the sky can be conveniently considered on a frame co-moving with the earth and decomposed into spherical harmonics[1]:

$$\frac{\Delta T}{T}(\vec{x}) = \sum_{\ell=1}^{\infty} \sum_{m=-\ell}^{\ell} a_{\ell m} Y_{\ell m}(\vec{x}) \tag{1.2}$$

The spherical harmonic multipole ℓ represents the angular (spatial) frequency and is related to the angular wavelength θ by $\ell = 2\pi/\theta$ so that large

[1] On a small patch of the sky where curvature is negligible, Fourier analysis can be applied, with ℓ being the Fourier wave-number.

multipoles correspond to small angular scales. It follows that the angular correlation function can be written as:

$$C(\vec{x}) = \frac{1}{4\pi}\sum_{\ell}\sum_{m}\left\langle a_{\ell m}^2\right\rangle P_\ell \cos(\vec{x}) \tag{1.3}$$

where P_ℓ is the Legendre polynomial. It can be shown that the corresponding angular power spectrum in ℓ-space as a function of multipole moment can be expressed as:

$$C_\ell = \frac{1}{(2\ell+1)}\sum_{m}\left\langle a_{\ell m}^2\right\rangle \tag{1.4}$$

in unit of $\left(\Delta T/T\right)^2$ (see e.g. Knox, 1995). The C_ℓ are observable quantities of the temperature variation signal of the microwave background. Since the spherical harmonics expansion of the sky temperature fluctuation is only possible with full sky coverage the C_ℓ values would not be statistically independent. Therefore rather than looking for errors in individual C_ℓ one usually look for covariance of the full set of C_ℓ values. Since there are only $(2\ell+1)$ m-samples of the power in each multipole moment, the minimal error in the spectrum measurement (i.e. the cosmic variance [1]), is given by $\Delta C_\ell = \sqrt{2/(2\ell+1)}C_\ell$. It is the variance of the multipoles that encodes information about the perturbations. Indeed, cosmological model predicts statistics of the coefficient $a_{\ell m}$ of the spherical harmonics. They have a mean value of zero with variance C_ℓ.

The observed power spectrum is biased by the instrument characteristics, such as the finite resolution from antenna pattern, the observing strategy, sky coverage, and intrinsic pixel noise – since maps are generated by pixelizing the sky. These details are typically expressed in the form of a window function (White & Srednicki 1994), which can be seen as a measurement of the sensitivity of the instrument to various multipoles. Following White and Srednicki (1994), it can be shown that:

---

[1] We are reminded here that a finite sampling of a random process leads to an uncertainty in the variance (sampling variance) no matter how precisely each event is measured. It is equal to twice the square of the variance divided by the number of samples. For each ℓ there are 2l+1 samples drawn from a Gaussian distribution of variance C_ℓ.

$$\left(\frac{\Delta T}{T}\right)^2 = \frac{1}{4\pi}\sum_{\ell=1}^{\infty}(2\ell+1)\left[C_\ell W_\ell + C_\ell^{pix}\right] \tag{1.5}$$

where C_ℓ^{pix} is the pixel noise (local event).

For a single dish experiment, it can be shown that the sensitivity to power at different angular multipoles is (White & Srednicki 1994):

$$\Delta C_l = \sqrt{\frac{2}{(2l+1)f_{sky}\Delta\ell}}\left[C_\ell + \frac{\sigma_{pix}^2 f_{sky}}{W_\ell \tau_{int}}\right] \tag{1.6}$$

with $f_{sky} = f_{field}\Omega/4\pi$. Adding more signal from different detectors would just increase the integration time. Equation (1.6) highlights two conflicting factors between the sample variance and the pixel noise that require a large and a small survey area respectively.

1.3.2 Foregrounds

For ground based and balloon-borne instruments, the primary source of contamination to detect primordial anisotropy is generally attributed to atmospheric emission. Observations from the Earth are performed within atmospheric windows, as shown in Figure 1.8. Amongst the multitude of molecular lines present in the atmosphere, water vapour is usually the dominant cause of opacity at millimetre wavelengths. To minimize atmospheric perturbations, dry and high-altitude locations such as the Atacama Desert in Chile, Mauna Kea in Hawaii, or the South-Pole host many CMB-dedicated instruments.

In addition to atmospheric contamination, the distinctive fingerprint of the CMB is blurred by numbers of astrophysical mechanisms at various frequencies, involving asymmetric emission, absorption or scattering of photons. However, the microwave background and foreground signals are distinguishable from their different spectral and spatial distributions. Multi-frequency observations are often required to allow post-detection subtraction of foreground signals (Brandt et al. 1994, Tegmark & Efstathiou 1996).

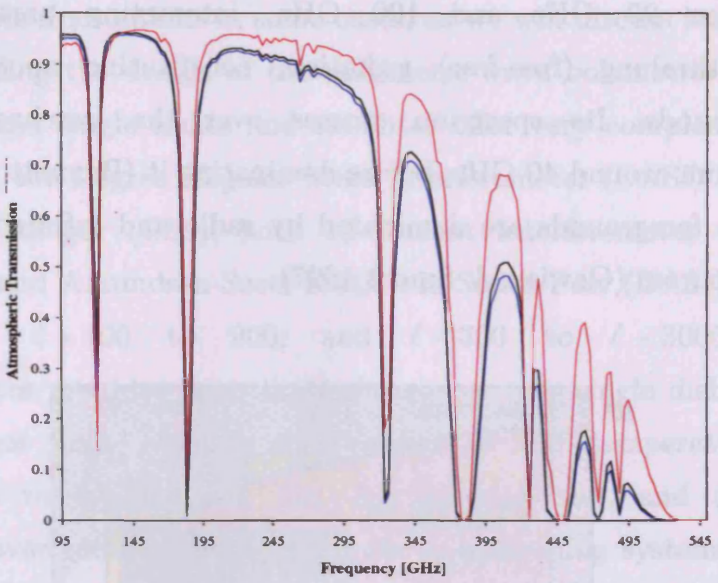

Figure 1.8: Atmospheric transmission
Atmospheric transmittance Mauna Kea, Atacama, and South Pole. The blue curve is from Mauna Kea (Hawaii in winter), the black from the Atacama plateau (Chile in summer) and the red one is from the South Pole (Antarctica winter). (Piccirillo, private communication).

Although CMB anisotropy dominates in the frequency range of 30 to 150GHz, its observation is highly constrained in a frequency window delimited by known sources of Galactic and extra-galactic foregrounds (Tegmark & Efstathiou 1996, Tegmark et al. 2000). These contaminants govern the choice of operational frequency of CMB experiments. Figure 1.9 shows the various foreground contaminants for the CMB signal at various angular scales and frequencies, together with the observation windows of various experiments.

- In the Galactic region, we distinguish three main sources of millimetre and microwave foregrounds present at all scales. The predominant source at millimetre wavelengths (above 100 GHz) comes from thermal dust emission. Elongated dust clouds in star-forming regions emit and absorb photons with polarization directed orthogonally to the local magnetic field (Glenn 1997).
- Highly energetic electrons spiralling within the Galactic magnetic field emit synchrotron radiation. Its contribution to CMB emission is estimated to be at most 20% at 15GHz and 0.1% at 90 GHz (Brandt et al. 1994), becoming negligible at frequencies above 20 GHz (Toffolatti et al. 1995).

- Between 20 GHz and 120 GHz, interacting particles generate Bremsthralung (free-free) radiation, constituting another source of foregrounds. Its spectrum crosses over the synchrotron emission spectrum around 40 GHz, before dominating it (Bennett et al. 1992).

Extragalactic foregrounds are dominated by radio and infrared point sources and cluster sources (Gawiser & Smoot 1997).

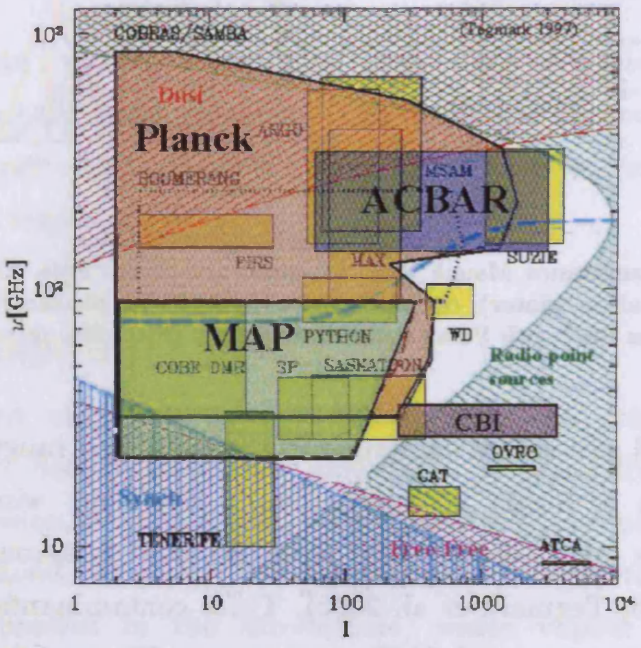

Figure 1.9: Observing frequency windows.
Shown in the graph is frequencies windows through galactic and extragalactic foregrounds (cf. text) Data are plotted in function of both the frequency and angular scale (from M. Tegmark's web page).

1.3.3 Instrumentation

Measuring minute temperature fluctuations of the CMB over a large range of angular scales requires state-of-the-art instrumentation. The intensity of the CMB 2.725 K black-body spectrum (Fixsen et al. 1996) peaks in the microwave at a frequency of ~170 GHz according to Wien's law (cf. Figure 1.10). Two types instruments are commonly used to resolve features in the CMB power spectrum: total power instruments, which would favour low angular multipole observations, and interferometers, which would efficiently resolve smaller angular scale (higher multipoles) while offering good rejection

to atmospheric fluctuations in some cases, as we will discuss later in Chapter 1 when presenting the design of the millimetre-wave bolometric interferometer. Interferometers, single-dishes and satellites offer very complementary results. For instance, the Degree Angular Scale Interferometer (DASI) and the Cosmic Background Imager (CBI), both 13-element interferometer operating from Chile (CBI) and Amundsen-Scott Station in South Pole (DASI), cover angular scales from $\ell \sim 100$ to 900, and $\ell \sim 300$ to $\ell \sim 3000$ respectively. Interferometers provides important advantages over single dish; they are able to (i) recover high angular scale signal in the temperature correlation spectrum to resolve features like the damping tail, and (ii) offer great advantages over total power instruments in controlling systematics, necessary to resolve very faint signals such as the polarized E and B-modes.

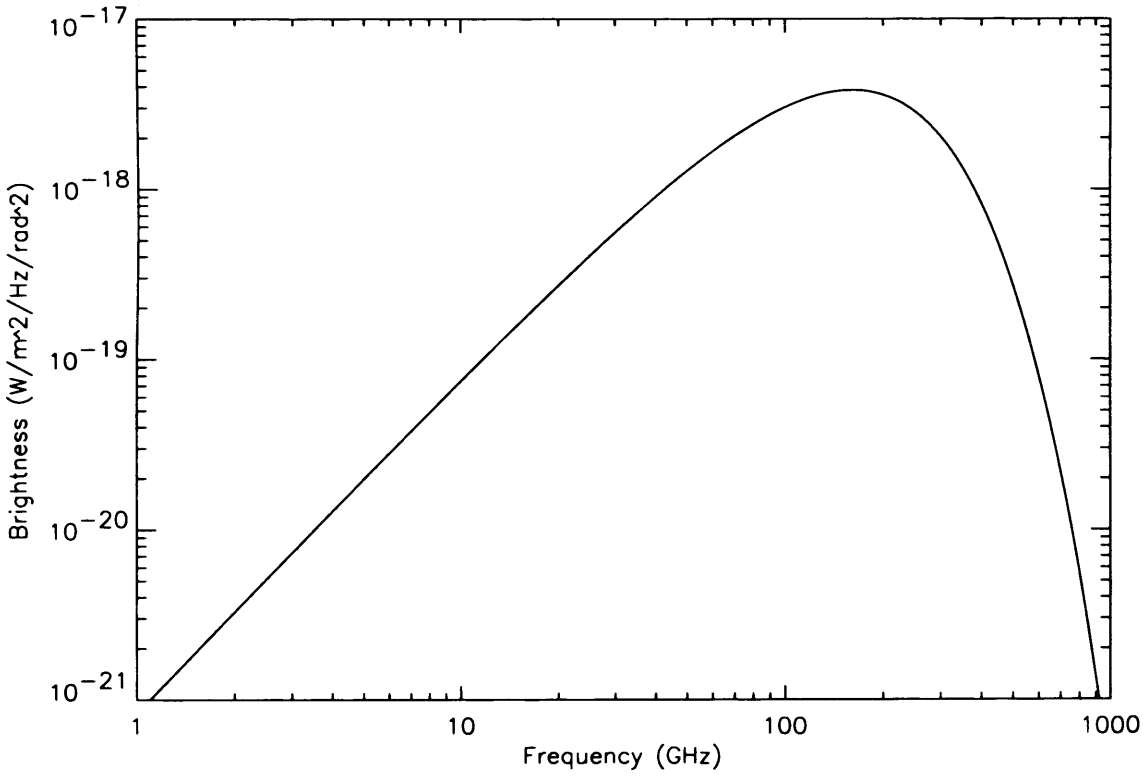

Figure 1.10: 2.725 Kelvin CMB black body – it peaks at ~170 GHz.

In 1998, the stratospheric long duration balloon Boomerang[1], a millimetre-wave bolometric instrument coupled to a 1.2 metre off-axis parabolic telescope, intended to resolve the power spectrum at degree and sub-degree scales between $100 < \ell < 600$ (Netterfield et al. 2002). Its operation from within the stratosphere, gives high sensitivities over the observing angular range and measured from Antarctica the fundamental acoustic peak in the temperature power spectrum at $\ell \sim 200$, confirming the theory of a flat Universe.

Many ground-based instruments serve as technological test-beds for satellite experiments. Space instruments produce cosmological datasets free of atmospheric distortions. Others key advantages of space instruments result from the sky coverage, as the entire celestial sphere can be observed, and the limitation of instrumental noise as they operate in a cool environment (lower telescope temperature compared to ground-based instruments). The uncertainty on the measurement is then statistically limited by the fact that observations are only done on one sky. The WMAP satellite's first-year of data reports measurements of the CMB temperature power spectrum on large and medium angular scales revealing the first acoustic peak at $\ell \sim 200$ and the second peak at $\ell \sim 600$ in $\langle TT \rangle$ with an accuracy never achieved by previous experiments (Bennett et al. 2003). These new measurements listed in Table 1.1 provide greater constraints on important cosmological parameters highlighted before and strongly favour an adiabatic flat universe of age 13.7 Giga-years. So far, one data point from WMAP in the polarization-temperature (Kogut et al. 2003) cross-correlated power spectrum strongly suggests the re-ionization of Hydrogen by the first galaxies 180^{+220}_{-80} million years after the initial singularity at a redshift of 17 ± 5 (Spergel et al. 2003), as shown in Figure 1.11. These results are in strong accordance with other experiments suggesting an inflationary flat universe dominated with dark energy (Page et al. 2003).

[1] Balloon Observations Of Millimetric Extragalactic Radiation ANd Geophysics

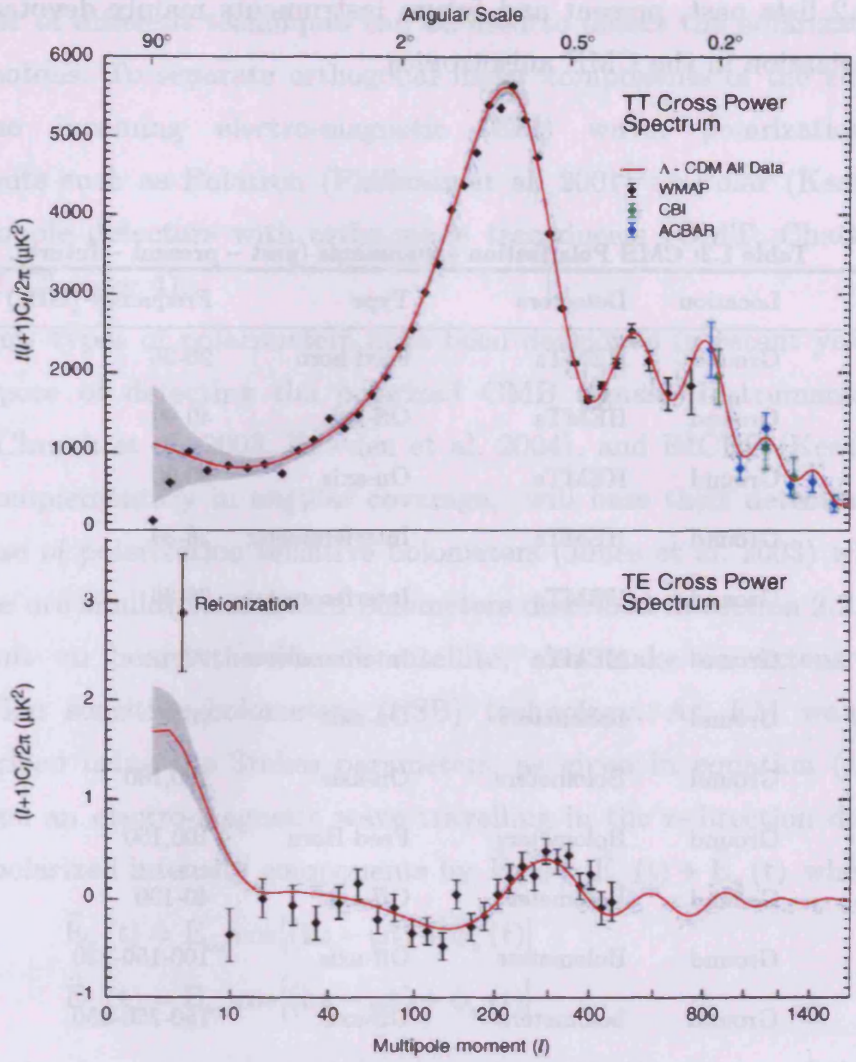

Figure 1.11: Measured WMAP TT and TE Power spectrum (Bennett et al., 2003)

1.4 Observation of the CMB polarization

Upper limits on the CMB polarization spectrum on medium and large angular scales already existed prior to WMAP detection (cf. section 1.3) from PIQUE (Hedman 2001), and POLAR (Keating 2001), both ground-based polarimeters. In 2001-2002, DASI first measured the polarization in the CMB spectrum revealing polarized features as predicted by CDM inflationary model (Kovac et al. 2002).

Table 1.2 lists past, present and future instruments mainly devoted to study the polarization in the CMB anisotropies.

Table 1.2: CMB Polarization experiments (past – present – future).

Experiments	Location	Detectors	Type	Frequency (GHz)	Status
POLAR	Ground	HEMTs	Feed horn	26-36	Completed
PIQUE	Ground	HEMTs	Off-axis	40,90	Completed
COMPASS	Ground	HEMTs	On-axis	30,90	Completed
DASI	Ground	HEMTs	Interferometer	26-36	Completed
CBI	Ground	HEMTs	Interferometer	26-36	Observing
AMIBA	Ground	HEMTs	Interferometer	90	Building
POLATRON	Ground	bolometers	On-axis	96	Stopped
QUaD$^{\diamond}$	Ground	Bolometers	On-axis	100,150	Building
BICEP$^{\diamond}$	Ground	Bolometers	Feed-Horn	100,150	Building
CAPMAP	Ground	Bolometer	Off-axis	40-100	Observing
CLOVER$^{\diamond}$	Ground	Bolometers	Off-axis	100-150-230	Proposed
PolarBear	Ground	bolometers	Off-axis	150-250-350	Proposed
ARCHEOPS	Balloon	Bolometers	Off-axis	353	Completed
MAXIPOL	Balloon	Bolometers	Off-axis	140-420	Completed
B2K	Balloon	Bolometers	Off-axis	145-245-345	Completed
EBEX	Balloon	--	--	150-250-350-450	Proposed
WMAP	Space	HEMTs	off-axis	22,30,40,70,90	Observing
SPORT$^{\diamond}$	Space	HEMTs	Feed-horn	22-32-90	Building
PLANCK-HFI$^{\diamond}$	Space	HEMTs/bolos	off-axis	30, 44, 70, 100, 143, 217, 353	Building
NASA inflation probe program$^{\diamond}$	Space	--	--	--	--

$^{\diamond}$ Although B-mode remains undetected, these instruments may present sensitivity capability that might lead to their detection, depending on their faintness.

A number of different techniques can be used to detect the polarization of the CMB photons. To separate orthogonal linear components of the electric field from the incoming electro-magnetic (EM) wave, polarization-sensitive instruments such as Polatron (Philhour et al. 2001) or Polar (Keating et al. 2001), couple detectors with ortho-mode transducers (OMT, Chattopadhyay 1998) (cf. Chapter 4).

New types of polarimeters have been developed in recent years for the sole purpose of detecting the polarized CMB signals. Instruments such as QUaD (Church et al. 2003, Bowden et al. 2004), and BICEP (Keating et al., 2003), complementary in angular coverage, will base their detection systems on the use of polarization sensitive bolometers (Jones et al. 2003) whose basic principles are similar to standard bolometers described in section 2.2. The HFI instrument on board the Planck satellite, also make an extensive use of polarization sensitive bolometers (PSB) technology. An EM wave is fully characterized using the Stokes parameters, as given in equation (1.7). Here, we assume an electro-magnetic wave travelling in the z-direction decomposed into its polarized intensity components by $\vec{E}(t) = \vec{E}_x(t) + \vec{E}_y(t)$ where:

$$\begin{aligned} \vec{E}_x(t) &= E_{0x}\cos\left[(kz - \omega t) + \phi_x(t)\right] \\ \vec{E}_y(t) &= E_{0y}\cos\left[(kz - \omega t) + \phi_y(t)\right] \end{aligned} \tag{1.7}$$

where k is the wave vector, $\phi_x(t)$ and $\phi_y(t)$ the phase shift of each component, and ω the angular frequency. The degree and type of polarization of the observed EM wave depends on the relationship between both phasors in (1.7) given by the Stokes parameters[1]: I represents the time-average of the power of the electric fields, Q and U characterize the linear polarization and V the circular polarization.

$$\begin{aligned} I &= \langle E_x^2 \rangle + \langle E_y^2 \rangle \\ Q &= \langle E_x^2 \rangle - \langle E_y^2 \rangle \\ U &= 2\langle E_x \rangle \langle E_y \rangle \cos(\phi_y - \phi_x) \\ V &= 2\langle E_x \rangle \langle E_y \rangle \sin(\phi_y - \phi_x) \end{aligned} \tag{1.8}$$

[1] It is usual to convert the Stokes parameters from intensity unit to brightness temperature by cross-correlating the signal with an astrophysical source of know temperature and emissivity.

The polarization angle θ_p in terms of Q and U is given by:

$$\theta_p = \frac{1}{2}\tan^{-1}\left(U/Q\right) \tag{1.9}$$

where $0 < \theta_p < \pi$. The observation of the polarized signature of the CMB has first been considered by various techniques originating from radio and IR instrumentation. For reasons highlighted previously in section 1.2, the CMB is not expected to be circularly polarized, and so Q and U are sufficient to characterize the linear polarization of the CMB anisotropies.

The measurement of the polarization power spectra certainly confirms the acoustic nature of the anisotropies. Measurements of the amplitudes of the gravitational waves would provide a test to inflationary models. Polarization measurements will enhance precision in determining cosmological parameters by breaking degeneracy (peaks of the polarization spectra provide information on the baryon abundances and the Hubble constant), for example by isolating the recombination and the re-ionization epoch.

For a comprehensive derivation of the formalism used to describe to polarization of the CMB we direct the reader to Kamionkowski (Kamionkowski, Kosowsky & Stebbins, 1997).

1.5 Observing the SZ effect

The Sunyaev-Zel'dovich distortion of the CMB spectrum is observed in many ways using a broad range of instrumentation. Observations of the SZ effect often require a long integration time, and therefore a good mapping speed. Interferometers, due to their mapping and resolution capabilities are particularly efficient to retrieve the structural information, while offering a good rejection of confusing radio sources and systematics.
Bolometric receivers are capable of a better mapping speed. They offer a broad frequency range, even coupled to a single dish (e.g. Bolocam, ACBAR, SuZIE and SCUBA). Observations at different frequencies improve the subtraction of foreground contamination from the SZ spectrum, and allow

extraction of the CMB structure to distinguish the increment, decrement and null of the SZ effect (cf. section 1.2.3).

Listed in Table 3.1 are past, current and future SZ experiments.

Table 1.3: Main SZ experiments (past, present, future)

experiment	location[◊]	frequency (GHz)	type[+]	detectors/antennas[X]	status
ACBAR	South Pole (VIPER)	345,274,219,150	On-axis	Bolometers (16)	Completed
Bolocam	Hawaii (CSO)	272,214,143	On-axis	Bolometers (144)	Operating
SCUBA	Hawaii (JCMT)	353,667	On-axis	Bolometers (37-91)	Operating
SuZIE	Hawaii (CSO)	350,220,150	On-axis	Bolometers (4)	Operating
SCUBA2	Hawaii (JCMT)	450, 850	On-axis	Bolometers (>10,000)	Building
ACT-MBAC	Chile (ACT)	145-225-265	Off-axis	Bolometers (3072)	Building
OCRA	Poland	30	On-axis	Heterodyne	Building
SPT-BA	South Pole (SPT)	150-220	On-axis	Bolometers (1024)	Building
AMiBA	Chile	95	Interferometer 19 elements	Heterodyne	Building
AMI-Ryle	UK	12-18	Interferometer 8x13m-10x3.7m	Heterodyne	Building
BIMA	US	70-90,90-115, 130-170,210-270	Interferometer 10x6.1m	Heterodyne	Building
OVRO-BIMA	US	30	Interferometer 6x10.4m	Heterodyne	Observing
SZA	US	26-36,85-115	Interferometer 8x3.5m	Heterodyne	Building
VSA	Canary Islands	26-36	Interferometer 14 elements	Heterodyne	Operating
APEX-SZ	Chile (APEX)	150-143	On-axis	Bolometers (330)	Building
Planck-HFI	Space	100, 143, 217, 353, 545, 857	Off-axis	Bolometers (50)	Building
Planck-LFI	Space	30,44,70	Off-axis	Heterodyne	Building

[◊]where applicable, the name of the telescope from which the instrument operates is given in brackets.
[+]where applicable, the numbers of antennas and their diameters that composed an interferometer are given.
[X]where applicable, the total number of detectors is given in brackets.

1.6 Thesis outline

In this chapter, we have set the scientific scene in which the instrumentation we discuss in the following chapters sits. Thus far, the observations outlined throughout this introduction tend to confirm the scenario of a dark matter dominated universe. Instruments built in the last decade have produced data that tighten the cosmological parameters. The challenge now has turned towards the design of experiments capable of measuring the electric and magnetic polarization signatures of the relic photons. In parallel, the study of secondary anisotropies, in particular those attributed to the SZ effect, are being carried out by a wide range of instruments, whilst also being at the heart of current design studies (cf. Table 1.3 for existing and upcoming principal SZ dedicated experiments). In this context, we outline in Chapter 2 the main instrumentation techniques related to the experimental work presented in this thesis. We emphasize the principles of interferometry to provide a theoretical background to the discussion of a bolometric radio-interferometer. We also summarize the principle of operation of a bolometer as well as cryogenic sorption fridges, necessary to achieve high sensitivity at millimetre wavelengths.

In Chapter 3, we discuss the prototype design and development of a new type of ground-based instrument able to achieve high sensitivity at small angular resolution by taking advantages of interferometry and bolometric techniques: the millimetre-wave bolometric interferometer (MBI). This new type of instrumentation is believed to be particularly useful to studies of the SZ effect, a strong contributor to secondary anisotropies at high ℓ, as well as the CMB anisotropy at larger angular scales.

We investigate in Chapter 4, the noise performance of Polatron, in terms of its technical capability to study the polarization of the relic radiation. Polatron had been conceived as a bolometric polarimeter coupled to a close-loop cooling system. Our interest in the context of this thesis is focussed on the operation and behaviour of the bolometers with the original mechanical cryocooler.

Finally in Chapter 5, we present work undertaken to improve the thermal circuit of the cold amplifier stage of Bolocam, a bolometric camera operated from the CSO in Hawaii, whose key science goal in respect to this thesis is to study secondary anisotropies in the CMB.

Chapter 2 Instrumentation Techniques

This chapter aims to provide the theoretical background related to the work performed on the three bolometric instruments – MBI-P, Polatron and Bolocam - discussed in chapter 3, 4 and 5 respectively.

We first give a detailed introduction to interferometry, relevant for the design of the bolometric interferometer prototype. We then discuss two key aspects in bolometric instrumentation, namely the principles of operation of bolometers and sorption cryogenic fridges.

2.1 Principles of interferometry

2.1.1 Interference

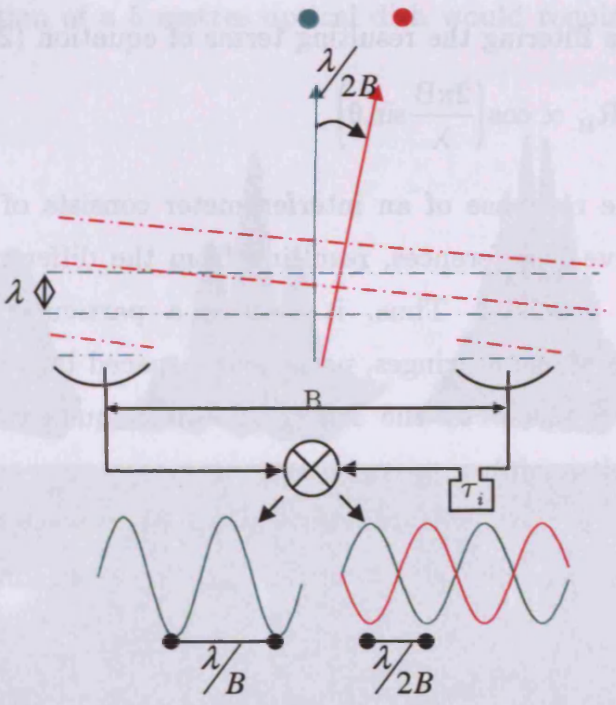

Figure 2.1: Constructive and destructive interferences.
Note that the interference pattern does not take into account the diffraction of light through the two circular apertures. The destructive interference occurs when both signal are out-of-phase, i.e. coming from two point distant of $\beta = \lambda/(2B)$ radian, where β is integer.

Astronomical interferometry consists of observing electromagnetic radiation E(t) emitted from a source, with several distinct apertures; each pair of telescopes (or horns) defines a baseline B. Following the illustration of a two-element interferometer depicted in Figure 2.1, photons of wavelength λ are incident on two telescopes at a slightly different time τ_g. The difference in arrival time is a function of the incoming wave direction θ. The induced voltages of the form V(t) from each aperture are correlated together, resulting in a time-averaged product of the two signals. The ideal response of the correlator to a point source is thus the auto-correlation[1]:

$$R_c(\tau) = \langle V(t)V(t-\tau)\rangle = \int_{-\infty}^{+\infty} V(t)V(t-\tau)dt \tag{2.1}$$

where we introduced the quantity τ such as $\tau = \tau_g - \tau_i$ with τ_i the instrumental delay necessary to compensate for the geometrical delay (cf. Figure 2.1). The ideal interference (fringe) term of the interferometer output can be easily worked out. The planar wavefront from the source reaches the instrument such that the output of the multiplier is proportional to:

$$R_M \propto \sin(2\pi\nu t)\sin\left[2\pi\nu\left(t-\tau_g\right)\right]. \tag{2.2}$$

After low-pass filtering the resulting terms of equation (2.2), we obtain:

$$R_M \propto \cos\left(\frac{2\pi B}{\lambda}\sin\theta\right). \tag{2.3}$$

Therefore, the response of an interferometer consists of periodic constructive and destructive interferences, resulting from the different optical path length both signals travelled. Thus, it creates a particular illumination pattern composed of a series of fringes, periodically spaced by λ/B radians, equivalent in the Fourier space to the fringe spatial frequency denoted by $u = B/\lambda$ (fringe per unit angle).

Introducing l as the direction cosine of θ with respect to the direction of the interferometer baseline (i.e. $l = \sin\theta$), equation (2.3) simplifies to:

$$R_M \propto \cos(2\pi ul) \tag{2.4}$$

---

[1] The approximation of the time averaging between $\pm\infty$ denoted by the brackets, suppose the correlator time-constant to be much larger than the bandwidth (or equivalently much bigger than the fringe period) so that a significant number of interferences occurs during one time constant occurrence.

This sets the interesting relationship between the angular period and the spatial frequency. The one-dimensional aperture distribution and its far-field distribution (angular and spatial domains) are related by their Fourier transform $E(l,t) \rightleftharpoons \tilde{E}(u,t)$:

$$\begin{aligned} \tilde{E}(u,t) &= \int E(l,t)e^{-i2\pi ul}dl \\ E(l,t) &= \int \tilde{E}(u,t)e^{i2\pi ul}du \end{aligned} \tag{2.5}$$

Following the Rayleigh criterion, it can be shown that the diffraction-limited resolution of an interferometer $\Delta\theta_{interf}$ is given by the angular distance between the centre and the first null of the fringe pattern (fringe tracking centre):

$$\Delta\theta_{interf} \propto \lambda/2B \tag{2.6}$$

Hence, at a given wavelength, a better resolution is achieved on longer baselines. As the baseline increases, more details are resolved characterized by the presence of more fringes in the interference illumination pattern, as illustrated in Figure 2.2. The enhanced resolution that interferometers provide, make measurements at optical and radio wavelength comparable. For example, the resolution of a 5 metres optical dish would require a 40 km dish in the radio-domain.

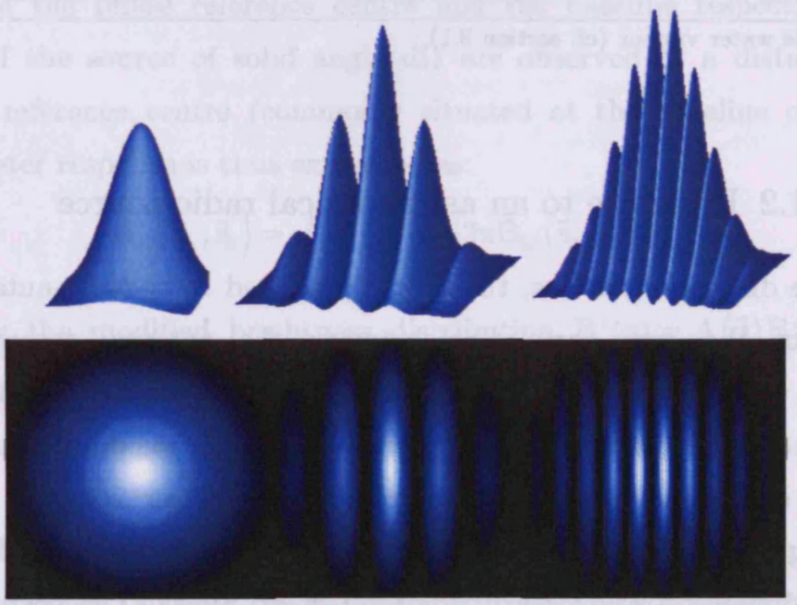

Figure 2.2: Illumination patterns
Representation of the illumination patterns of a Gaussian-like circular aperture on the left, and the additive combination of two such primary beam at a small baseline (middle) and at a longer baseline, or shorter spatial-frequency (right) resolving smaller angular distances.

In the optical, the contrast of the fringes is usually considered when studying the interferometer response, and is expressed as the fringe visibility. The visibility V_M of a Michelson-type interferometer is defined by the normalized fringe amplitudes differences:

$$V_M = \frac{I_{max} - I_{min}}{I_{max} + I_{min}}, \tag{2.7}$$

where I_{max} and I_{min} refer to as the maximum and minimum fringe intensities respectively. A totally constructive or destructive interference leads to a visibility of one or zero respectively. It is relevant to note here that the Michelson visibility as stated in (2.7) does not contain any information about the phase of the fringes. The comparison between interferometry in the optical and radio domain is interesting and is partially given in Table 2.1 below.

Table 2.1: Optical versus millimetre interferometry

	radio (millimetre)	optical
frequency	30 - 450 GHz	10 – 600 THz
noise limited	Photon limited	Background limited
instrumental noise	Receiver	Detector readout
seeing origin	PWV* fluctuations	Temperature fluctuations
atmosphere coherence time	Several tens of minutes	~ 10 milliseconds
Measurements	Complex visibility	Fringe contrast

*precipitable water vapour (cf. section 3.1).

2.1.2 Response to an astronomical radio source

For single dish observations, the power produced by a radio-antenna receiver consists of the cross-correlation between the antenna reception pattern $A(l'-l_0)$ with the brightness, $B(l')$, of an extended source (or flux density for a point source) where l_0 is the antenna pattern maximum and l' is the direction of the source. In interferometry, the power received per baseline differs slightly since the reception pattern of a two-element interferometer has now the dimension of power (Thompson et al. 1998). The correlator output from Equation (2.4) now includes this cross-correlation:

$$R_c(l_0) \propto \Delta\nu \int_{source} dl' B(l') A(l' - l_0) \cos\left[2\pi u (l_0 - l')\right] \qquad (2.8)$$

Expressed differently, the coverage of the antenna pattern scanning the source (i.e. convolution including displacement, multiplication and integration) relates the brightness distribution of the source with the mirror image of the interferometer power reception pattern $\hat{A}(l_0 - l')$:

$$R_c(l_0) \propto \Delta\nu \int_{source} dl' B(l') \hat{A}(l_0 - l') \cos\left[2\pi u (l_0 - l')\right] \qquad (2.9)$$

The spatial power spectrum of the measured brightness distribution is computed by the Fourier transform of the previous convolution. So, from the convolution theorem, and with $\tilde{R}_c(u) \rightleftharpoons R_c(l_0)$, it can be shown that (Thompson et al. 1998):

$$\tilde{R}_c(u) = \frac{A\Delta\nu}{2}\left[\delta(u - u_0) + \delta(u + u_0)\right]\tilde{B}(u) \qquad (2.10)$$

Equation (2.10) shows that at a particular baseline, the (spatial) frequency spectrum is filtered at $\pm u_0$, a concept that will prove its importance later in studying the advantages of interferometry in Chapter 3.

Following Thompson (Thompson, Moran & Swenson 1998), we extend our discussion to a three-dimensional space. We express equation (2.9) using vectorial notation, so that the directional vectors $\vec{s}_0$ and $\vec{B}_\lambda$ are in the direction of the phase reference centre and the baseline respectively. Small elements of the source of solid angle $d\Omega$ are observed at a distance $\vec{\sigma}$ from the phase reference centre (commonly situated at the baseline centre). The interferometer response is thus expressed as:

$$R_c\left(\vec{B}_\lambda, \vec{s}_0\right) = \int_{4\pi} B'(\vec{\sigma}) \cos\left[2\pi \vec{B}_\lambda . (\vec{s}_0 + \vec{\sigma})\right]. \qquad (2.11)$$

Introducing the modified brightness distribution $B'(\sigma) = A(\vec{\sigma})B(\vec{\sigma})$ and the complex visibility $V = |V| e^{j\varphi}$ so that:

$$V = \int_{4\pi} B_N'(\vec{\sigma}) e^{-i2\pi \vec{B}_\lambda . \vec{\sigma}} d\Omega, \qquad (2.12)$$

it can be shown that the modulus and phase of the visibility corresponds to the amplitude and phase of the measured fringes. The correlator output given by equation (2.11) is rewritten as a function of the visibility fringe amplitude and phase to:

$$\tilde{R}_c\left(\vec{B}_\lambda, \vec{s}_0\right) = A_0 \Delta\nu |V| \cos\left(2\pi \vec{B}_\lambda . \vec{s}_0 - \varphi\right), \tag{2.13}$$

where the visibility phasor is indicated by φ. By making observations at different baselines - or equivalently at different spatial frequencies - one can construct the complex visibility function, or equivalently the Fourier transform of the brightness distribution of the source as indicated by equation (2.12).

2.1.3 Aperture synthesis

Figure 2.5 depicts the particular case of an interferometer with a baseline oriented east-west. In this case, an extended source passes the interferometer power pattern from east to west as the earth rotates. Therefore, each baseline corresponds to a particular spatial frequency and thus to a certain angle between the source and the baseline projected on the sky. It is difficult, and certainly very slow, to synthesis a two-dimensional map without a two-dimensional (spatial)-frequency spectrum. As an illustration, one can think of the beam in the Fourier space that corresponds to a single baseline. Since the beam is not azimuthally symmetric, the interferometer response to the (temperature) fluctuation is diluted as shown in Figure 2.5. On the other hand, the instrument would be less sensitive to fluctuations aligned with the baseline vector. This lack of mapping capabilities can be overcome by adding N apertures to the array, to form $N(N-1)/2$ baselines[1].

By convention the geometry involved in interferometry is referred to as the (uv) plane and consists of a coordinate system where spatial frequencies represents distances measured in wavelength unit. The (uv) plane is a right-handed plane, normal to the direction of pointing s_0. The u direction is oriented toward the east, where as v is directed towards the north as illustrated in Figure 2.4.

[1] Note that the aperture synthesis technique was pioneered by Sir Martin Ryle, which earned him the 1974 Nobel Prize in Physics.

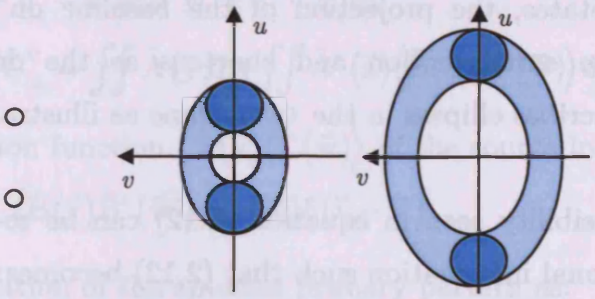

Figure 2.3: Fourier-space coverage of an east-west two-element interferometer. The light blue areas represent the spatial frequencies in the (uv) plane to which the interferometer is sensitive; its width is a result of the cross correlation of the antenna apertures. The corresponding spatial resolution for cross-correlated signals is represented by the dark blue filled areas. The denser are the loci, the more sensitive the interferometer is.

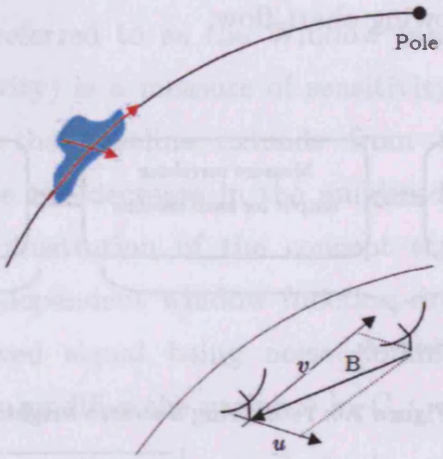

Figure 2.4: the right-handed (uv) plane. The *uv* plane is normal to the source direction. The *v-axe* is oriented north and the *u-axe* is oriented towards the east.

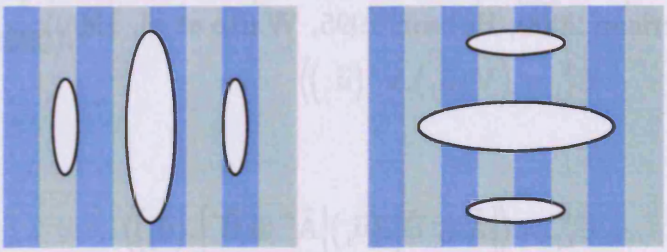

Figure 2.5: orientation of fluctuation (blue and green) and interferometer in the Fourier plane. a) shows the case where the baseline is oriented orthogonally to the fluctuations, resulting in a maximum response. in b) the fluctuations are aligned with the baseline and the response of the interferometer is minimum.

As the earth rotates, the projection of the baseline on the celestial sphere rotates from the earth motion and shortens as the declination decreases. Therefore, it describes ellipses in the (uv) plane as illustrated in Figure 2.3.

The complex Visibility seen in equation (2.12) can be re-arranged to include the two-dimensional information such that (2.12) becomes:

$$V(u,v) = \iint \mathrm{dldm}\, B'(l,m) e^{-i2\pi(ul+vm)} \tag{2.14}$$

This last equation sets the basis of interferometry. Indeed, it shows that the response of an interferometer is a direct measure of the Fourier transform of the source brightness distribution, relationship known as the Van Cittert-Zernike theorem[1]. The process of recovering the brightness of the source is shown in the following chart flow:

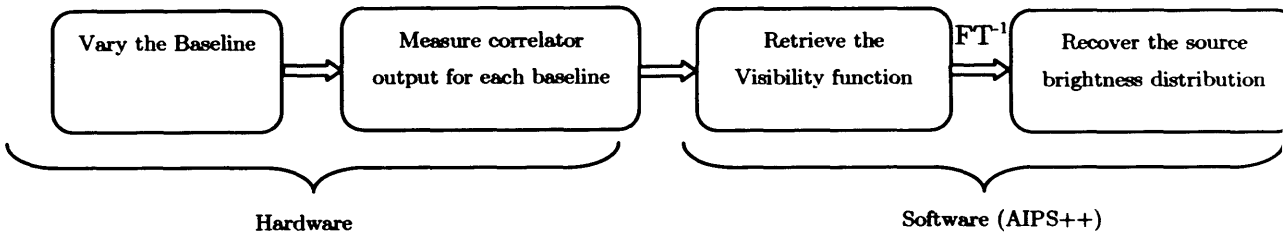

Figure 2.6: recovering a source brightness distribution

In synthesis mapping, the covariance matrix constitutes a measure of the level of coherence in different visibilities sampled over a source. It is a common relation used to evaluate the noise in the visibilities. The auto-correlation function between two visibilities from 2 directions in the (uv) plane is written as follow (Harrison 2000, Hobson 1995, White et al. 1999):

$$C^V_{i,j} = \left\langle V(\vec{u}_i).V^*(\vec{u}_j) \right\rangle \tag{2.15}$$

Hence,

$$\begin{aligned} C^V_{i,j} &= \left\langle \left[\tilde{A} \otimes \tilde{B}\right].(\vec{u}_i)\left[\tilde{A}^* \otimes \tilde{B}^*\right].(\vec{u}_j) \right\rangle \\ &= \left\langle \iint \tilde{A}(\vec{y})\tilde{B}(\vec{u}_i - \vec{y})d^2y \iint \tilde{A}^*(\vec{z})\tilde{B}(\vec{u}_j - \vec{z})d^2z \right\rangle \end{aligned} \tag{2.16}$$

[1] The Van Cittert-Zernike theorem is the spatial equivalent to the Wiener-Khinchin equations in the temporal domain where the correlator response is the Fourier transform of the source power spectrum (Thompson, Moran & Swenson 1998, and Hecht 2002).

simplifies with $\vec{v} = \vec{u}_i - \vec{y}$ and $\vec{w} = \vec{u}_j - \vec{z}$ to:

$$C_{i,j}^{V} = \iint \tilde{A}(\vec{y}) d^2y \iint \tilde{A}^*(\vec{z}) \left\langle \tilde{B}(\vec{v}) \tilde{B}^*(\vec{w}) \right\rangle d^2z \tag{2.17}$$

If the autocorrelation function $\left\langle \tilde{B}(\vec{v}) \tilde{B}^*(\vec{w}) \right\rangle$ of the source intensity is set to:

$$\left\langle \tilde{B}(\vec{v}) \tilde{B}^*(\vec{w}) \right\rangle = S(\vec{v}) \delta(\vec{v} - \vec{w}), \tag{2.18}$$

and the autocorrelation of the antenna primary pattern as:

$$W(\vec{v}) = \tilde{A}(\vec{u}_i - \vec{v}) \tilde{A}^*(\vec{u}_j - \vec{v}), \tag{2.19}$$

it can be shown that the covariance matrix is (Hobson, 1995):

$$C_{i,j}^{V} = \iint W(\vec{v}) S(\vec{v}) d^2\vec{v} \tag{2.20}$$

where the power spectrum has a maximum amplitude peak when $u = v$. Equation (2.19) is usually referred to as the Window function. The window function (or spectral sensitivity) is a measure of sensitivity of the instrument to spatial frequencies. As the baseline extends from the most compact configuration, one can notice the decrease in the amplitude of the sensitivity spectral function, a direct illustration of the concept stated above. In the CMB analysis, the baseline-dependent window function drops off at larger ℓ, characteristic of the observed signal being noise dominated. The window function of an interferometer modifies the variance in C_ℓ:

$$\Delta C_\ell = \sqrt{\frac{2}{(2l+1) f_{sky} \Delta\ell}} \left[C_\ell + \frac{\sigma_{base}^2 f_{field}}{W_\ell \tau_{int}} \right] \tag{2.21}$$

where $\Delta\ell$ is the actual binning in ℓ-space[1], σ_{pix} and σ_{base} are the detector noises respectively per pixel and per baseline in $\mu K_{CMB}\sqrt{s}$ (White et al. 1999, Harrison et al. 2000).

[1] The final resolution will always be limited by the sky coverage, e.g. $\Delta\ell \simeq 180/\Delta\theta$. Only satellites like WMAP and Planck are all-sky experiments.

2.2 Bolometers: principles of operation

Since this thesis is only dealing with bolometric instruments, we examine in this section the basic principle of the operation of a bolometer (Jones 1953). A complete description can be found in Mather (1982), Richards (1994), and also in Rieke (2003).

2.2.1 Steady state equation

Shown in Figure 2.7 is a schematic illustration of a bolometer operation and a typical readout circuit. A typical bolometer consists of an absorber and a thermistor, connected to a heatsink held at a temperature T_0 through a small thermal conductance $G_S(T)$. A bolometer absorbs the energy of the incident radiation and converts it into heat - i.e. variations in the power incident on the bolometer are directly observable in variations of the bolometer temperature. This results in a rise of the temperature, T1, of the absorber - characterized by its heat capacity C - until the power flowing into the absorber equals the power P_0 flowing through the thermal link.

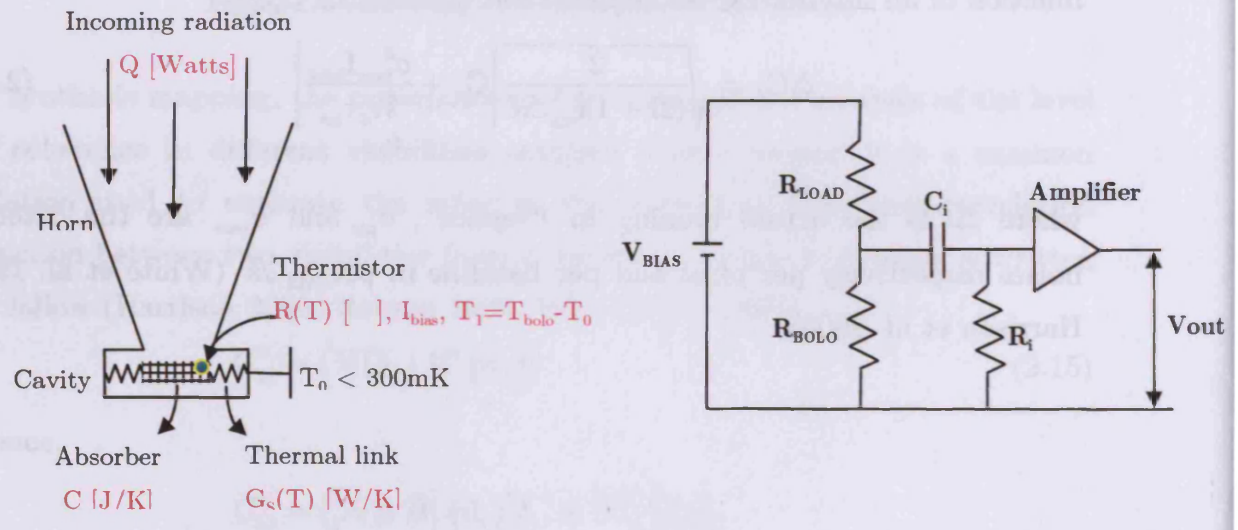

Figure 2.7: (Left) schematic of a typical bolometer
It is composed of an absorber and a thermistor heat-sunk through a thermal conductance. (Right) Bias readout electronic.

The bolometer is mounted in a bridge circuit with a load resistor R_L , so that a bias current I_{bias} flows through the bolometer. Thus, fluctuations in bolometer temperature translate into changes in the resistance of the thermistor. These in turn are converted into voltage variations. In a steady state, it can be shown that:

$$P_0 = G_S T_1 \tag{2.22}$$

$$P_I(t) = C\,{}^{dT_1}\!/_{dt} \tag{2.23}$$

$$P_T(t) = G_S T_1 + C\,{}^{dT_1}\!/_{dt} \tag{2.24}$$

where $P_I(t)$ is the power deposited on the absorber, and T_1 the rise in temperature above the heat sink base temperature (cf. Figure 2.7). Following Rieke (2003) and Richards (1994), the sudden change in the amount of power from a steady state can be described by a step function:

$$\eta P_I(t) = \begin{cases} 0\,, & t < 0 \\ P_1, & t \geq 0 \end{cases} \tag{2.25}$$

so that equation (2.24) can be solved:

$$T_1(t) = \begin{cases} {}^{P_0}\!/_{G_S}\,, & t < 0 \\ \dfrac{P_0}{G_S} + \dfrac{\eta P_1}{G_S}\left(1 - e^{-{}^{t}\!/_{\tau}}\right)\,, & t \geq 0 \end{cases} \tag{2.26}$$

from which it can be deduced the bolometer thermal time constant is:

$$\tau = {}^{C}\!/_{G_S}\,. \tag{2.27}$$

The time response of the device is constrained by the absorber heat capacity and the thermal conductivity of the thermal link.

2.2.2 Bolometer performance

The performance of a bolometer is typically expressed in terms of a noise-equivalent-power (NEP) - the amount of power needed to achieve a unity signal-to-noise ratio (SNR) in a 1 Hz frequency bandwidth. Therefore, the NEP in $W/\sqrt{Hz}$ can be expressed by the ratio of the rms noise voltage fluctuations e_{rms} to the voltage responsitivity $S(\omega) = dV/dP$ (in volts per

watts, where ω is the angular frequency) of a bolometer with a current biased thermistor:

$$NEP = \frac{e_{rms}}{S(\omega)} \tag{2.28}$$

The ultimate sensitivity per pixel is achieved whenever the bolometer noise is equal to or less than the fluctuation of the photon noise. There are a number of noise sources that limit a bolometer performance, which can be categorised from their frequency-dependence. In some cases, it is possible to minimize their respective NEP, so that their effects can be attenuated, or even neglected.

Three noise sources dominate the NEP of an ideal bolometer (Mather 1982, Richards 1994):

- the *Johnson noise*, arising from the random thermal motion in the conductive material that generates random charge distribution. It has a power spectral density over an infinite range of frequency (white noise) and is proportional to the temperature T of the device. The Johnson NEP (which includes the electro-thermal effect) is given by Mather (Mather 1982):

$$NEP_J^2 = kT\frac{(R+Z)^2}{R.S^2}, \tag{2.29}$$

  where Z, R and S are the bolometer dynamic impedance, resistance, and voltage responsivity at zero frequency respectively, and k the Boltzmann's constant. NEP_J^2 is highly dependent to the temperature T, which motivates the need to cool the bolometer at a very low cryogenic temperature. Following the treatment given in (Rieke 2003), it can be shown that:

$$NEP_J \propto \begin{cases} G_s T^2 & \text{for } \alpha(T) \approx T^{-3/2} \\ G_s T^{3/2} & \text{for } \alpha(T) \approx T^{-1} \end{cases} \tag{2.30}$$

  where $\alpha(T)$ is bolometer thermal coefficient as described later in 2.2.3.

- the *phonon noise*, caused by random energy fluctuation occurs in the thermal link due to the flow of phonons. The integration over the

phonon distribution leads to the frequency independent relationship (Richards 1994):

$$NEP_P^2 = 4kG_dT^2 \tag{2.31}$$

- the *Photon noise*, arises from the random arrival of photons onto the absorber, leading to a variation in the mean-squared energy detected by the bolometer (Lamarre 1989, Richards 1994). It is a frequency independent source of noise, depending in the number of photons per mode, n, and consists in two terms:
  - the shot noise (BLIP[1]): it occurs when n is much less than 1 (i.e. $h\nu/kT \gg 1$). This noise is dominant at high frequency in the optical and near-infrared.
  - the wave noise: in this case photons are considered to arrive in bunches which occur at lower frequency and $n \gg 1$.

  It can be shown (Richards 1994) that the photon NEP consists in:

$$NEP_\gamma^2 = P_{srce}h\nu + \frac{P_{srce}^2}{\Delta\nu}, \tag{2.32}$$

where h is the Planck's constant, P_{srce} is the detected power in watts, and $\Delta\nu$ is the frequency bandwidth. Expanding equation (2.32) (Richards 1994) for a source at a temperature T being observed by an experiment with an optical efficiency η and a throughput $A\Omega$ in a background temperature T_{bkg}, and emissivity ε:

$$NEP_\gamma^2 = \frac{4A\Omega(kT_{bkg})^5}{c^2h^3}\int_0^\infty dx \frac{\eta\varepsilon x^4}{(e^x-1)}\left[1+\frac{\eta\varepsilon}{e^x-1}\right], \tag{2.33}$$

where k is the Boltzmann's constant and $x = h\nu/kT$. In the Rayleigh-Jeans regime (i.e. $h\nu \ll kT_{bkg}$), equation (2.33) simplify to:

$$NEP_\gamma^2 = 2Q(h\nu_0 + \eta\varepsilon kT_{bkg}), \tag{2.34}$$

where Q is the incident radiative power loading given by $Q = A\Omega(\eta\varepsilon)B(\nu_0, T_{bkg})\Delta\nu$, and the frequency bandwidth $\Delta\nu$ centred on ν_0.

[1] Background Limited Infrared Power

Since the Johnson, phonon, and photon noise are uncorrelated, the total bolometer NEP is given by (Mather 1982, Richards 1994):

$$NEP^2_{total} = NEP^2_{\gamma} + NEP^2_J + NEP^2_P + NEP^2_N, \tag{2.35}$$

where NEP^2_N is an additional term to take into account electronic noise described in Mather (1982) (e.g. microphonics and 1/f noise) that occurs at different stages in the electronics (e.g. from the cold amplifier stage, load resistor).

2.2.3 Characterization of an ideal bolometer

Following Griffin & Holland (1988), an ideal bolometer can be characterized by assuming that (i) the bias current is constant, and (ii) the resistance of the bolometer only depends on the temperature – i.e. no electro-thermal feedback, and $R_L \gg R_{BOLO}$ so that the current flowing in the bolometer is independent from the bolometer resistance. In this case, the relationship between the resistance and the temperature follows a power law given by:

$$R_{bolo}(T) = R_0 e^{-\sqrt{\Delta/T}}, \tag{2.36}$$

where R_0 and Δ are material dependent properties (typical values are respectively 150-200Ω and 50K for germanium thermistor at 300mK.

The temperature-dependent voltage across the bolometer can be written as:

$$\frac{dV(T)}{dT} = \frac{R(T)}{dT} I_{bias} = \alpha(T) R I_{bias}, \tag{2.37}$$

with the thermal coefficient factor:

$$\alpha(T) = \frac{1}{R}\frac{dR}{dT} = -\sqrt{\frac{\Delta}{4T^3}}, \tag{2.38}$$

describing the change of the resistance with temperature.
The relationship between temperature and the thermal conductivity of an ideal thermal link can be also expressed as a power law:

$$k(T) = k_0 \left(T/T_0\right)^{\beta} \tag{2.39}$$

where β is the thermal conductivity index and k_0 the thermal conductivity at T_0.

The performances of an ideal bolometer can be characterized with 3 dimensionless parameters:

- the bias parameter $\phi = T/T_0$ 1
- the material parameter $\delta = T_g/T_0$
- the loading parameter $\gamma = \eta Q/(GT_0)$ (cf. equation (2.34)).

Electrical and thermal properties of a bolometer can be derived from the analysis of load curves (response of a bolometer voltage to a variation of the current flowing through it) as shown in Figure 2.8. Parameters such as the thermal conductance, the bolometer temperature, the optical and instrumental loading, and the optimum bias level I_{bias} can be derived from the I-V curves. Typically, a load curve analysis consists of acquiring a set of I-V curves under different known optical loads, (e.g. blanked, room and nitrogen temperature), and various bath temperatures. The local slope of the I-V curve is given by the inverse of the dynamic impedance $Z^{-1} = dI/dV$.

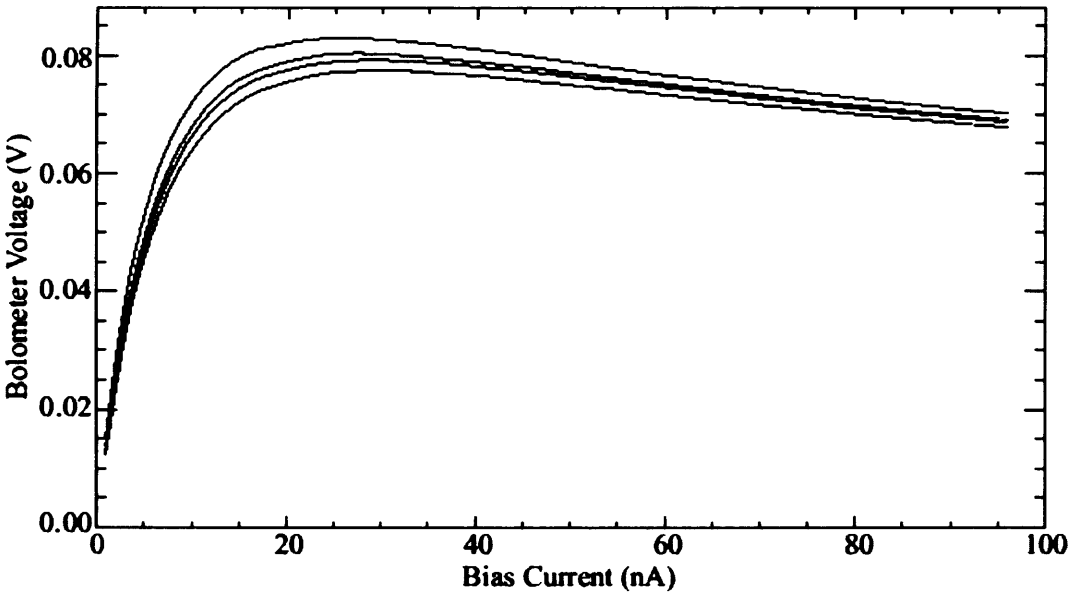

Figure 2.8: Typical bolometer load curves.
From top to bottom, the curves represent the receiver looking at 4K, 73K, 290K, 338K (Gom et al. 1999). The bolometer becomes less sensitive when exposed to (excess) loading.

2.3 Cryogenic techniques

To maximise their performance, bolometers require operation at cryogenic temperatures. The bolometer NEP decreases with the operating temperature, as shown in Table 2.2 below.

Table 2.2: Bolometers typical sensitivity figures.

Temperature	Fridge	NEP* (in $W/\sqrt{Hz}$)
4.2	^{4}He	$5.0x10^{-13}$
1.5	^{4}He at 1 mbar	$2.0x10^{-14}$
0.32	^{3}He at 5 μbar	$2.0x10^{-16}$
0.10	ADR	$5.0x10^{-18}$

***The NEP given in this table are given to express to order of magnitude difference between various temperatures. (Hargrave P., private communications)**

To achieve sub-Kelvin temperature, the first step is typically to minimise the heat transfer throughout the cryostat where the detector is located.

2.3.1 Heat transport

Heat is usually transferred via three principal mechanisms (convection, conduction and radiation) from hot to cold environment, changing the internal energy of both systems according to the first law of thermodynamics. We are mostly interested by heat being transported via conduction through a solid, and radiation following Stefan's law.

- Convection is made negligible by enclosing the detector system in a vacuum pumped cryostat. By decreasing their probability to collide with each other - i.e. increasing the mean free path of the particles, heat transfer through conduction via gas molecules can be dramatically reduced. Indeed, for particles in motion it can be shown that the mean free path is a function of the number of molecules per unit volume n_v:

$$\lambda = \left(\sqrt{2}\pi d^2 n_v\right)^{-1} \tag{2.40}$$

where d represents the molecular diameter. Using Avogadro's number, N_A and the ideal gas law - so that $n_v = nN_A/V = N_AP/(RT)$, we can express equation (2.40) as a function of the temperature and pressure:

$$\lambda = RT/\sqrt{2}\pi d^2 N_A P\,, \tag{2.41}$$

where R=8.314 J.mol^{-1}.K^{-1} is the ideal gas constant, P the pressure and T the temperature of the gas. It is clear from equation (2.41) that lowering the pressure leads to increase the molecules mean-free-paths.

- The heat transfer through a solid is express by the equation (White, 1968):

$$\dot{Q} = \frac{A}{l}\int_{T_1}^{T_2} \lambda(T)\,dT\,, \tag{2.42}$$

where $\lambda(T)$ is the thermal conductivity, A the cross-section area, and l the length of the solid under consideration (e.g. wires).

- The radiative transport of heat between two surfaces at temperature T_1 and T_2 respectively is given by:

$$\dot{Q} = \sigma A\left(T_1^4 - T_2^4\right)\frac{\varepsilon_1\varepsilon_2}{\varepsilon_1 + \varepsilon_2 - \varepsilon_1\varepsilon_2}\,, \tag{2.43}$$

where ε_1 and ε_2 are the emissivity of two surfaces. To minimize this effect, a surface with a low emissivity is required, or equivalently a high reflectivity, e.g. clean polished gold platted copper (White 1968).

2.3.2 Helium Sorption Fridge: qualitative description

In this thesis, the performances of the bolometric receivers are provided by the use of sorption fridges. This section describes the principles of operation of a three-stage sorption fridge, using two stable isotopes of Helium - ^{3}He and ^{4}He, as working gases[1]. All three bolometric detection systems discussed in later

[1] The significant difference between those two isotopes is set by their respective quantum properties. ^{4}He is classified as a boson, zero-spin (i.e. its nucleus consist of 2 neutrons and protons of ½-spin each), and obey Boson-statistics. However, ^{3}He being consisted of 3 nucleons (½-spin) behave as an electron obeying Fermi-Dirac statistics following Pauli exclusion principles (White, 1968).

chapters, involve the use of triple-stage fridges based on a design from Bhatia et al. (2000), and manufactured by Chase Research[1].

The performances of the sorption fridge to achieve sub-Kelvin temperature below 300 mK, is essentially due to the use of charcoal cryopumps. The cryopumps contain porous, activated charcoal of which the equivalent surface is greater than 1 $km^2.g^{-1}$ (White 1968). It has the advantage that it desorbs helium gas at elevated temperature (~40K) and adsorb the gas at lower temperature (<18K) via Van Der Waals binding forces. Pumping the evaporated particles from a helium bath decreases its boiling point (function of the vapour pressure) well below its superfluid transition (λ -point). In this process, the cooling power improves as the number of molecules decreases, or equivalently as the vapour pressure (hence the temperature) decreases. Temperature as low as ~750 mK can be reached with ^{4}He, limited in practice by the minute vapour pressure. To reach lower temperatures requires the rare ^{3}He isotope. At a given low temperature, ^{3}He has a higher vapour pressure than ^{4}He, making possible to reach a temperature as low as ~250mK, still above the λ-point (~2.5 mK). Table 2.3 summarizes some molecular characteristics of both helium isotopes.

Table 2.3: Properties of ^{3}He and ^{4}He

Isotope	Inv/temp (K)	Boiling point (K)	Critical temp (K)	Critical pressure (atm)	λ-point	Quantum statistic
^{3}He	~40K	3.2	3.34	1.15	~2.5 mK	Fermion
^{4}He	~51K	4.2	5.19	2.26	2.17 K	Boson

[1] Chase Research, 35 Wostenholm Rd, Sheffield S7-1LB, UK

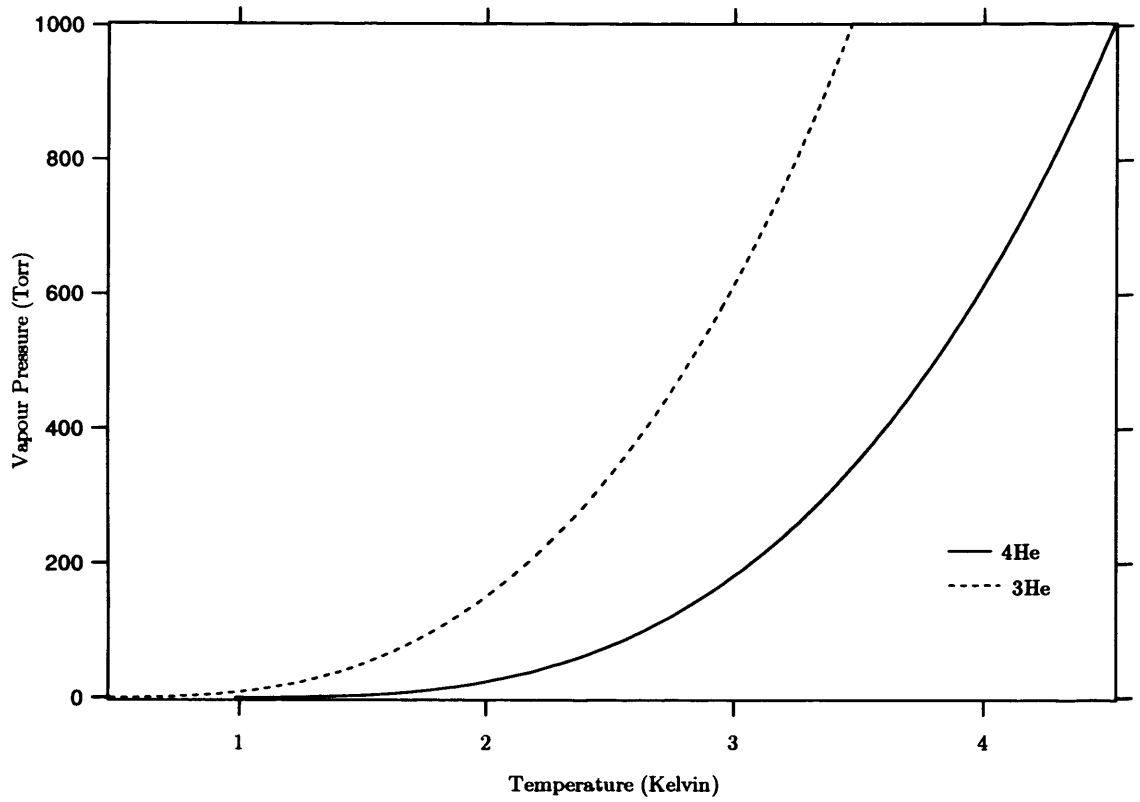

Figure 2.9: Vapour pressure versus temperature for ^{3}He and ^{4}He (Keith 2001)

The operation of a single ^{3}He sorption fridge is illustrated in Figure 2.10. Initially, the charcoal is heated to ~ 40K to desorb all gas particles; once all the particles have condensed, the charcoal is rapidly cooled down (using a heat switch connecting the cryopump to the baseplate), adsorbing all remaining gas particles (it is preferable that the baseplate temperature is below the ^{3}He boiling point, which is typically achieved by pumping on the main ^{4}He bath). From the effect of cryo-pumping, the ^{3}He liquid - fallen into the condenser under gravity - sees its pressure decrease. Using this method, a final temperature as low as ~300 mK can be reached by cryo-pumping down to ~0.2 Pa. The cold-head temperature of the fridge stabilizes at its lowest temperature for a period of time which depends on the amount of ^{3}He gas present in the fridge and the thermal loading (e.g. 5 litres STP of He^3 would condense 7 mL of liquid and last for 12 hours under no extra load).

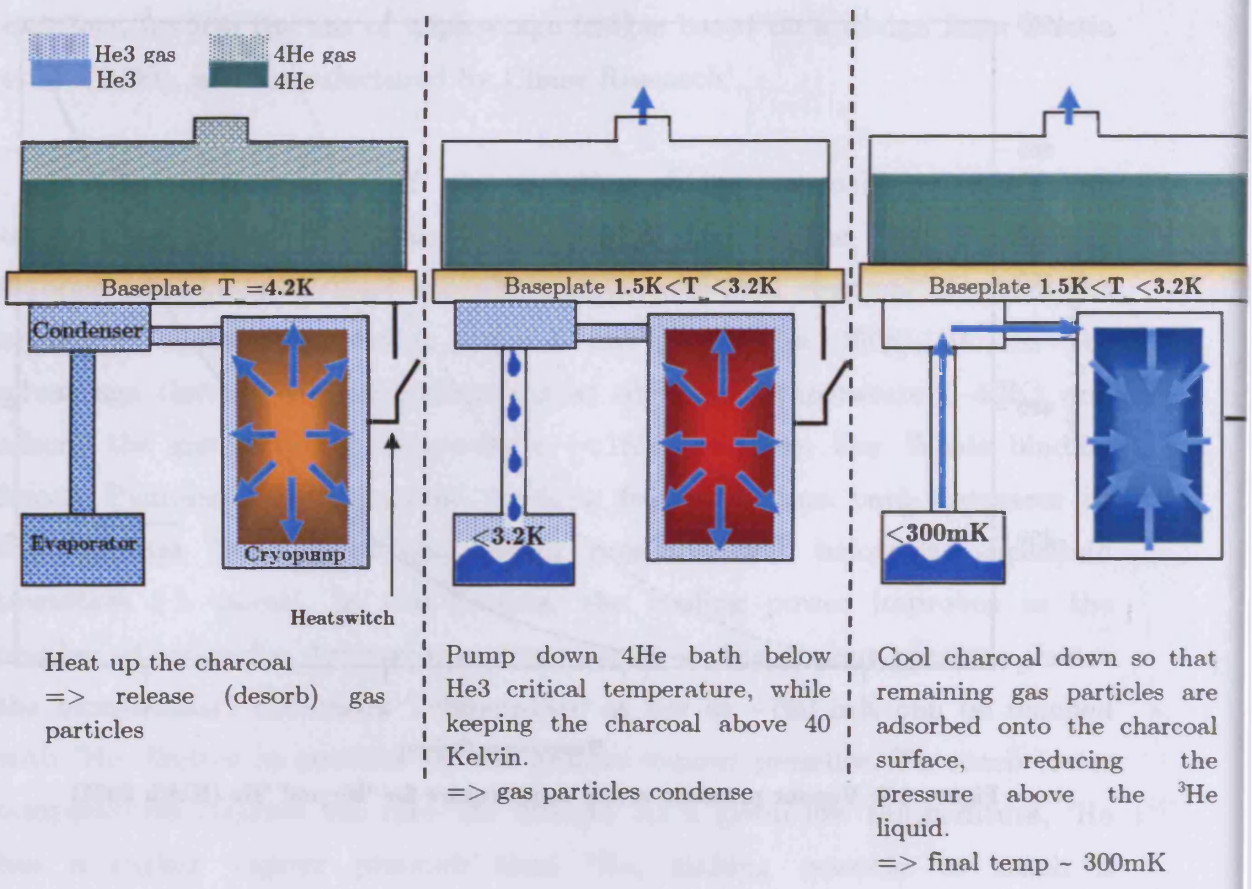

Figure 2.10: He^3 single-stage sorption fridge operation.

Although the use of a single stage ^{3}He fridge is adequate for small cryostats, its operation often requires pumping on the main liquid helium bath. In large cryostats, it is quite common to use a ^{4}He-^{3}He double-stage or ^{4}He-^{3}He-^{3}He triple-stage fridge. Figure 2.11 depicts the layout of a three-stage sorption fridge. We describe hereafter its principle of operation.

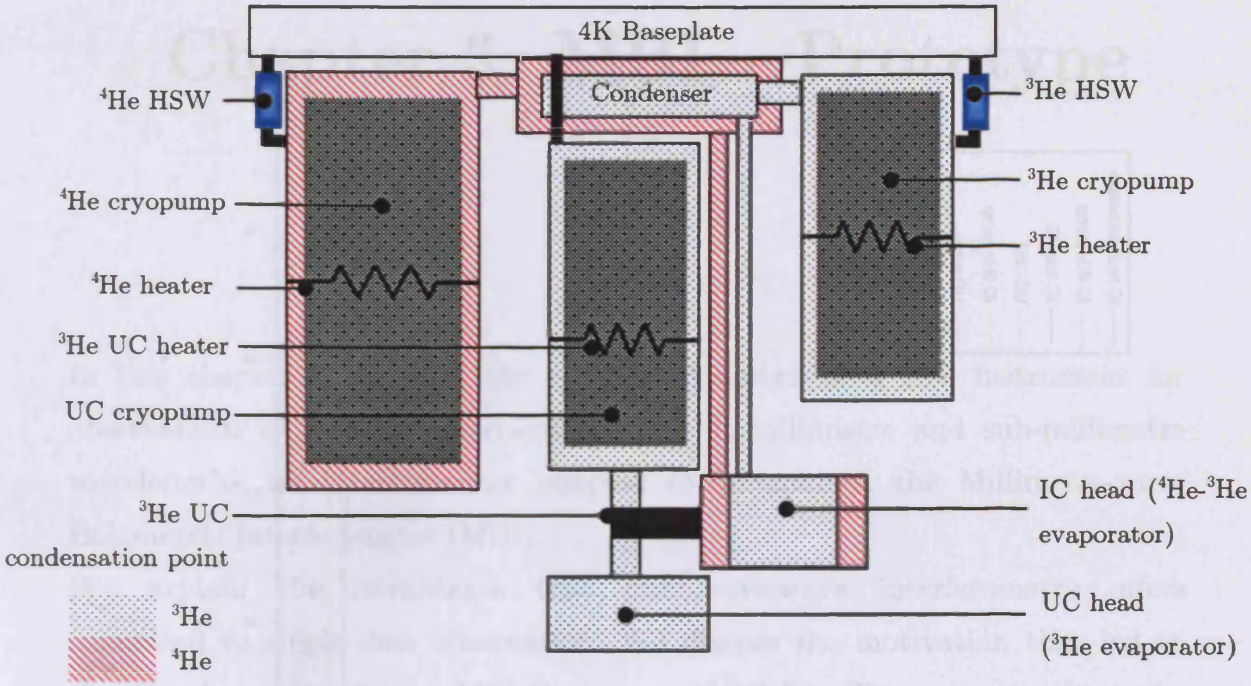

Figure 2.11: He^4- He^3- He^3 triple-stage sorption fridge basic operation. A typical cycle would last at least 2 to 3 hours. HSW, IC, and UC stands for heat-switch, intermediate-cold and ultra-cold respectively.

The operation of a triple-stage can be seen as cycling each stage (as described above) in a specific but variable order. We give here an example of a typical cycle, assuming that the fridge is at a liquid ^{4}He temperature:

- desorb ^{4}He gas by heating the ^{3}He cryopump - The ^{4}He starts condensing immediately.
- desorb ^{3}He gas by heating the ^{3}He cryopump, and UC cryopump.
- when all ^{4}He gas particles have condensed, pump on the ^{4}He liquid by turning the ^{4}He HSW - the IC head and the condenser cool down.
- when the condenser temperature is below the ^{3}He boiling point, the ^{3}He starts to condense - the IC head cools further down.
- when all ^{4}He has evaporated from the IC head, start pumping on the ^{3}He liquid present in the IC head by turning the ^{3}He HSW.
- when all ^{3}He gas particles have liquefied, pump on the UC head, by turning off the ^{3}He UC heater.

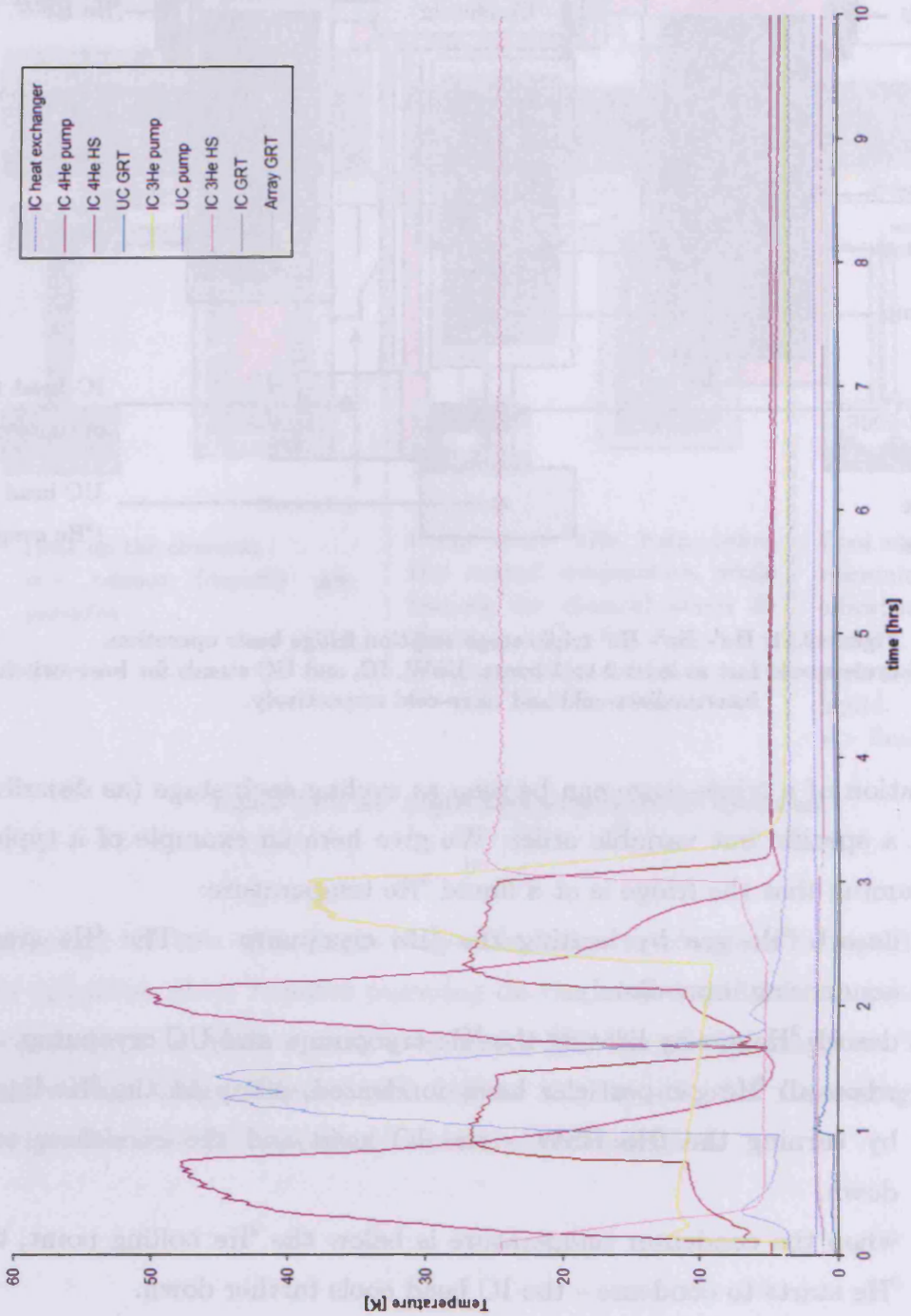

Figure 2.12: Example of a cycle of the 3-stage fridge.
This cycling procedure applies to Bolocam. The ultra cold-head reaches ~255mK for more than 24 hours.

Chapter 3 MBI – Prototype

In this chapter we present the conceptual design of a new instrument for observations of faint astrophysical sources at millimetre and sub-millimetre wavelengths: an interferometer coupled to bolometers, the Millimetre-wave Bolometric Interferometer (MBI).
We explain the advantages that millimetre-wave interferometry offers compared to single dish observation. We discuss the motivation that led to the development of the MBI-Prototype (MBI-P). Then, we analyse the peculiar sensitivity relationships that apply to MBI-P, on which we base our design. We finally describe the instrument and highlight the most important features of the (incomplete) construction of the two-element adding interferometer; this final section includes a description of the optics, cryogenics, motion control, and data acquisition.

3.1 Advantages of interferometers in radio-astronomy

There are a number of advantages that interferometry offers compared to single dish observations. The most relevant at millimetre wavelength lies in the rejection of atmospheric perturbation and instrumental noise. In some cases, the high resolution that the interferometer provides (cf. section 2.1), is an important factor (VLA, ALMA). However, the gain in resolution from very distant antennas occurs at a cost of a reduced collecting area leading to lowering the interferometer sensitivity - this notion of the filling efficiency is further detailed in section 3.4, when investigating the sensitivity of the MBI prototype.

• At millimetre-waves, highly time-variable water vapour clouds drift through any instrument beam producing a low-frequency noise to the instrument output signal, characterized by a 1/f noise signature. Fluctuations in water vapour column density cause distortion in the incoming wavefront, altering its phase (i.e. path length) above each telescope. This translates into variations in the pointing of the telescopes. For an interferometer, this corresponds to an additional time-delay which contributes to an unwanted phase-shift in the interferometer fringes. Eventually, the phases of the visibilities are no longer related to the Fourier phase of the source brightness distribution, causing a degeneracy of the Van Cittert-Zernike theorem. It can be shown that the rms phase fluctuation is related to the interferometer baseline according to :

$$\langle \phi^2 \rangle \propto B^n/\lambda \tag{3.1}$$

where the baseline B is expressed in km, and the wavelength λ in mm. At wavelengths greater than the water vapour column width, $n = 1/3$, while $n = 5/6$ for smaller wavelength (Coulman 1990, Carilli, Lay and Sutton 1998). For long baseline interferometry in the radio, observation of calibrators – a technique called phase referencing (Holdaway 1992, Holdaway & Owen 1995, Lay 1997), and monitoring of the emission from PWV in the line of sight of the antenna beam as a function of time (Lay 1997, Carlstrom et al. 1994), are used to derive a phase correction factor. But, because small baselines correspond to a narrow range of scale sizes, small baseline interferometers are more likely to offer a good rejection to atmospheric perturbations (Church 1995). Also, pointing offsets due to the alteration in the pathlengths are greatly limited for relatively small beamsizes.

• Interferometers are less sensitive to different systematics than single dishes. The interferometer fringe rate, its spatial filtering (cf. section 2.1.3) and in some cases the rapid phase-switching, contribute to disentangle and minimize systematics effects such as spurious signal arising from side-lobes pickup. For example, fringe rates of ground spillover differ from those of the phase reference centre, and are not correlated; thus, they can be easily identified not to appear in the construction of the complex visibility function.

- An interferometer response provides a direct measure of the Fourier transform of the sky brightness distribution. Using the Van Cittert-Zernike theorem it can be shown that the image of the object can be reconstructed from the set of phase and amplitude measurements of the interferometer (i.e. visibilities).

- Interferometers do not require fast mechanical chopping to differentiate atmospheric perturbation from the astronomical signal. This method developed for single dish observation consists of nutating the secondary mirror at a rate faster than the 1/f noise of the atmosphere. This technique may be combined to a nod movement of the entire telescope while chopping, so that the signal is transported alternatively in either the signal beam or the reference beam.

3.2 Technical motivation

Interferometry at centimetre wavelengths using coherent receivers (such as HEMT amplifiers), has demonstrated important advantages over filled-aperture techniques, particularly at high angular resolution and in forming maps. However, at millimetre and sub-millimetre wavelengths, cooled bolometers are substantially more sensitive than existing coherent detectors. The resulting instrument presents a new way of observing the CMB primary and secondary anisotropies (cf. Table 3.1 for existing and upcoming interferometers dedicated to CMB and SZ observations).

3.2.1 Possible science

Primary anisotropy - A priori, from the combination of interferometry (high rejection to atmospheric perturbation & systematics, and high resolution) and incoherent detection (high sensitivity), the concept of MBI offers good perspectives in the study of the 2.7K CMB. As seen in Chapter 1, by establishing its power spectrum over a broad range of angular scales, cosmologist can deduce key cosmological parameters (Hu, Sugiyama & Silk 1997, Liddle 1998). Upon completion, the proposed MBI-P could lead to

imaging the CMB from the ground (e.g. South Pole) at a frequency band centred at 150 GHz. MBI-P frequency and angular coverage (ranging from 30' to 3') is adequate to image the CMB anisotropy, and recover both scalar and polarization information. If fitted with a polarization-sensitive detector system, MBI-P could measure simultaneously temperature and polarization anisotropies, leading to observe the cross-correlation between the CMB polarization and temperature (cf. section 1.2.2).

Point sources - MBI-P using its high resolution capabilities could become useful to quantify the presence of foreground contamination in the recovered CMB maps (Hu & White, 1997b). With a baseline of up to 5 metres, MBI-P would have higher resolution than both WMAP and PLANCK and contribute to survey point sources polluting the CMB sky.

Secondary anisotropy - The sensitivity, the ability to remove systematics and the field-of-view (FOV) of several tenths of an arcminute make MBI-P particularly interesting to study the SZ effect in clusters of galaxies with angular sizes ranging from ~10' to 1'. Moreover, if MBI-P is sensitive to different frequencies situated below and above the 218 GHz null of the thermal SZ spectrum, the thermal effect could be spectrally separated from the kinetic effect produced by the motion of the clusters intra-medium.

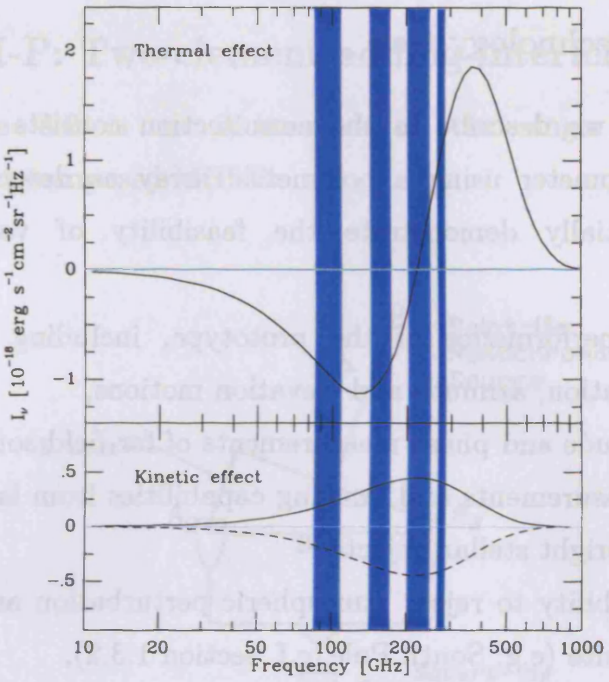

Figure 3.1: The SZ thermal and kinetic effects & possible MBI-P bandwidths. MBI will be able to distinguish the two effects spectrally.

Table 3.1: Current, past and planned CMB-related interferometers

Name	Location	status	#dish	Freq. (GHz)	Multipole ℓ Coverage*
VLA	United States	Current	27	5, 8, 15	5000 - 8000
Ryle	United Kingdom	Current	8	5, 15	4000 - 8000
ATCA	Australia	Current	6	9	3500 - 5780
T - W	United States	Past	2	43	20 – 100
CAT	United Kingdom	Past	3	13 – 17	339 - 722
VSA	Canary Islands	Current	14	26 – 36	130 - 1800
DASI	South Pole	Past	13	26 – 36	125 - 700
CBI	Chile	Current	13	26 – 36	630 - 3500
AMIBA	Chile	Future	19	95	120-5000
MBI	Ground & space	in study	8	29-270	360-15000
ALMA	Chile	Future	64	30 – 1000	780E3-65E6

* the multipole (angular wave-number) can be approximate to roughly the inverse of the angular scale (in radians) times π.

3.2.2 Technology test

The prototype we describe in the next section consists of a single-baseline adding interferometer using a bolometric array as detectors. We aim with MBI-P to initially demonstrate the feasibility of various technological innovations:

- mechanical performance of the prototype, including fringe modulation, baseline variation, azimuth and elevation motions,
- fringe amplitude and phase measurements of far-field sources,
- visibility measurements and imaging capabilities from laboratory millimetre source, and bright stellar objects,
- instrument ability to reject atmospheric perturbation and systematics from an excellent site (e.g. South Pole, c.f. section 1.3.2),
- assess instrument performance in terms of sensitivity and aperture synthesis to ensure that the scientific goals described above are achievable,
- demonstrate the ability to perform deep field observations without chopping,
- investigate the addition of more antennas to multiply the baselines.

Our design of MBI-P is made up of a single baseline. In the next section, we discuss the principle of a two-element adding interferometer.

3.3 MBI-P: Two-element adding interferometer

Shown in Figure 3.2 is an illustration of the single baseline adding interferometer that composed MBI-P.

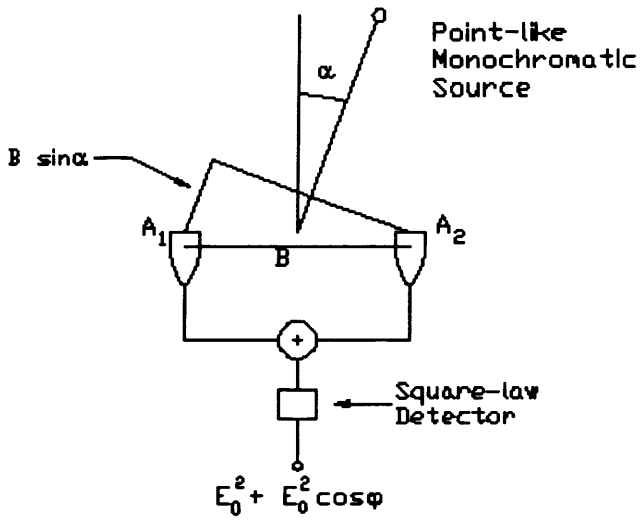

Figure 3.2: Adding two-element interferometer.

In this particular case, the electric field of the two distinct antennas are added, before being squared by an incoherent detector. This results in a constant term and an interference term. We show hereafter the mathematical steps to form the response of the adding interferometer, and verify that the Van Cittert-Zernike theorem holds.

Considering the interferometer described above in section 2.1, the farfield in the direction θ can be expressed as follow:

$$E(\theta) = E_2(\theta)e^{i\psi/2} + E_1(\theta)e^{-i\psi/2} \tag{3.2}$$

with $\psi = 2\pi B_\lambda \sin\theta$ where B_λ is the baseline B expressed in wavelengths. Ideally, the two incoming fields have the same amplitude and we define the primary pattern as $E_0(\theta) = E_1(\theta) = E_2(\theta)$, which leads to write:

$$\begin{aligned} E(\theta) &= 2E_0(\theta)\left(\frac{e^{i\psi/2} + e^{-i\psi/2}}{2}\right), \\ &= 2E_0(\theta)\cos\left(\psi/2\right) \end{aligned} \tag{3.3}$$

from which we express the total power pattern $P(\theta, B_\lambda)$ as:

$$P(\theta, B_\lambda) = \frac{1}{2}\left|E_0(\theta)\right|^2 (1 + \cos\psi) \tag{3.4}$$

As expected, equation (3.4) shows that the total power pattern is composed of the antenna power pattern and of the interference pattern, as plotted in Figure 3.3.

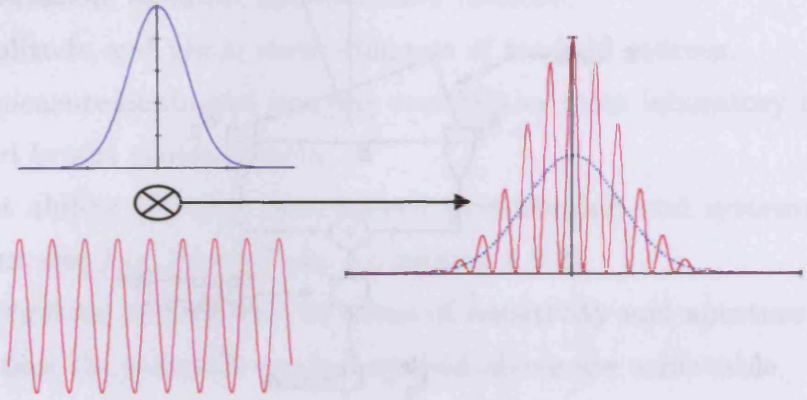

Figure 3.3: Two-element interferogram.
Plots are a function of pointing angle, illustrating the convolution of the primary beam pattern and the array pattern, resulting in the interferogram.

It follows that the observed (ideal) flux density can be expressed as:

$$S(\theta, B_\lambda) = \left|E_N(\theta)\right|^2 \int_{\substack{\text{Source} \\ \text{extent}}} B(\theta)\left[1 + \cos\left(2\pi B_\lambda \sin\theta\right)\right] d\theta \tag{3.5}$$

where $B(\theta)$ is the brightness of the source, and $E_N(\theta)$ is the normalized field pattern of an individual array element. Assuming that $\left|E_N(\theta)\right|^2 = 1$ and $S_0 = \int_{\substack{\text{Source} \\ \text{extent}}} B(\theta) d\theta$, equation (3.5) becomes:

$$S(\theta, B_\lambda) = S_0 + \int_{\substack{\text{source} \\ \text{extend}}} B(\theta)\cos\left[2\pi B_\lambda \sin\left(\theta_0 - \theta\right)\right] d\theta, \tag{3.6}$$

where θ_0 refers to as the pointing direction with the centre of the source. Equation (3.6) can be further simplified by expanding the cosine and sine terms to:

$$S(\theta, B_\lambda) = S_0\left[1 + V(\theta, B_\lambda)\right] . \tag{3.7}$$

By introducing the complex visibility function discussed in section 2.1.3 in the form of:

$$V(\theta, B_\lambda).e^{i2\pi B_\lambda \Delta\theta_0} = \frac{1}{S_0}\int_{-\alpha/2}^{\alpha/2} B(\theta)e^{i2\pi B_\lambda \theta}d\theta \tag{3.8}$$

and substituting it into (3.6), we obtain:

$$B(\theta_0) = S_0\int_{-\infty}^{\infty} V(B_\lambda).e^{-i2\pi B_\lambda(\theta_0-\Delta\theta_0)}dB_\lambda \tag{3.9}$$

Equation (3.9) demonstrates that the brightness distribution of the source is the inverse Fourier Transform of the complex visibility function, a measurable quantity:

$$B_{source}\alpha FT^{-1}[V]. \tag{3.10}$$

The quantity $V_0(B_\lambda)$stands for the fringe amplitude. When a function of B_λ, it refers to as the visibility function. Therefore $\Delta\theta_0$ represents the fringe displacement from the reference point. Expressed in terms of this displacement, we write:

$$V(\theta_0, B_\lambda) = V_0(B_\lambda)\cos\left[2\pi B_\lambda(\theta_0 - \Delta\theta_0)\right] \tag{3.11}$$

In the real world, the radio noise being Gaussian-distributed, signals coming from various frequencies are uncorrelated. Also, the use of sensitive bolometers as detectors allows a large bandwidth in order to assure their high sensitivity. Nevertheless, a band-smearing effect occurs when the ratio of the baseline over the diameter of the Cassegrain antenna is of the order of the wavelength over the bandwidth $\left(B/D \sim \Delta\lambda/\lambda\right)$. This can be easily quantified by considering a variation of the signal over a finite bandwidth $\Delta\nu$. Thus, the interferometer response in (3.4) has to be obtained from integrating over the bandwidth, as:

$$P(\theta, B_\lambda)_{\Delta\nu} = P_A\int_{\nu_0-\frac{\Delta\nu}{2}}^{\nu_0+\frac{\Delta\nu}{2}}\left[1+\cos(\psi)\right] \tag{3.12}$$

where P_A is the antenna power pattern (with a throughput assumed constant over the bandwidth). It results from equation (3.12) that the interference term in equation (3.4) is modulated by the sinc function having a coherence length of $\lambda^2/\Delta\lambda$. The interferometer response given in (3.4) becomes:

$$P(\theta, B_\lambda) = P_A\left[1+\mathrm{sinc}\left(\frac{\pi B\Delta\nu}{c}\sin\theta\right)\cos\psi\right] \tag{3.13}$$

and is plotted in red in Figure 3.4.

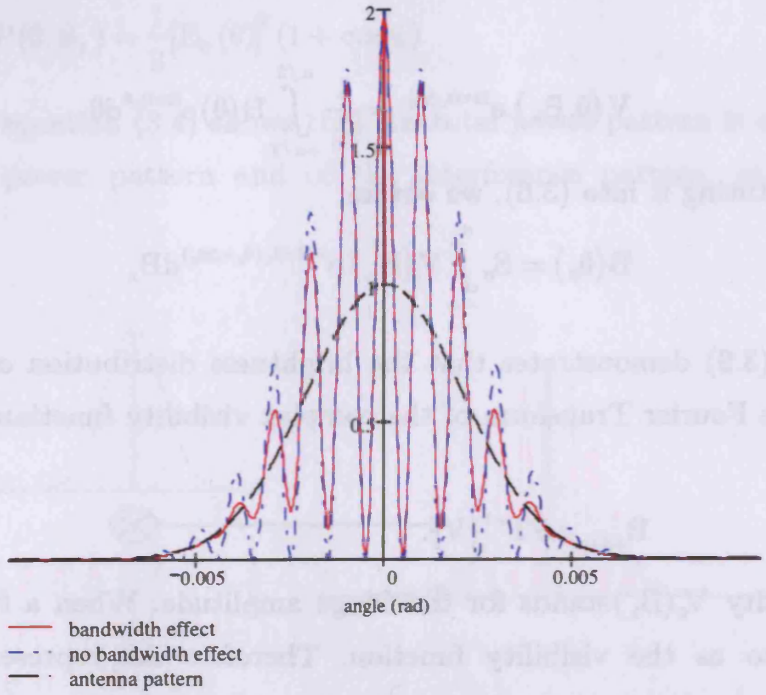

Figure 3.4: Interferogram of a 2-element adding interferometer. The dotted-blue line is the interferogram free of the bandwidth effect. The red interferogram illustrates the band-smearing effect. The dashed-black curve represents the antenna pattern.

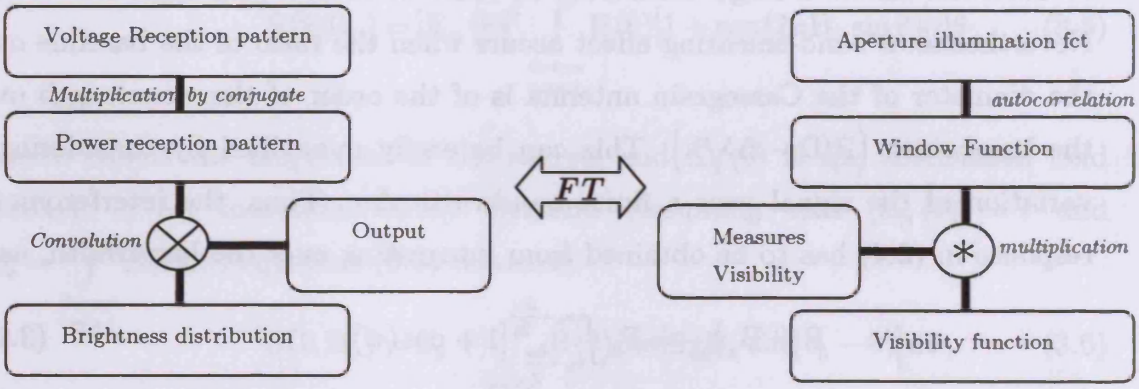

Figure 3.5: Mathematical relationships involved in interferometry. based on Thompson, p.115 (1998)

Stellar interferometers are composed of at least two antennas pointing at the same direction in the sky. In the radio, the signals of interest are commonly combined in a correlator before being detected by a square law detector. In the optical, the beam combination depends on the architecture of the beam combiner, and result in most cases in a pupil-plane, or image plane interferometer, also referred to as Michelson and Fizeau respectively.

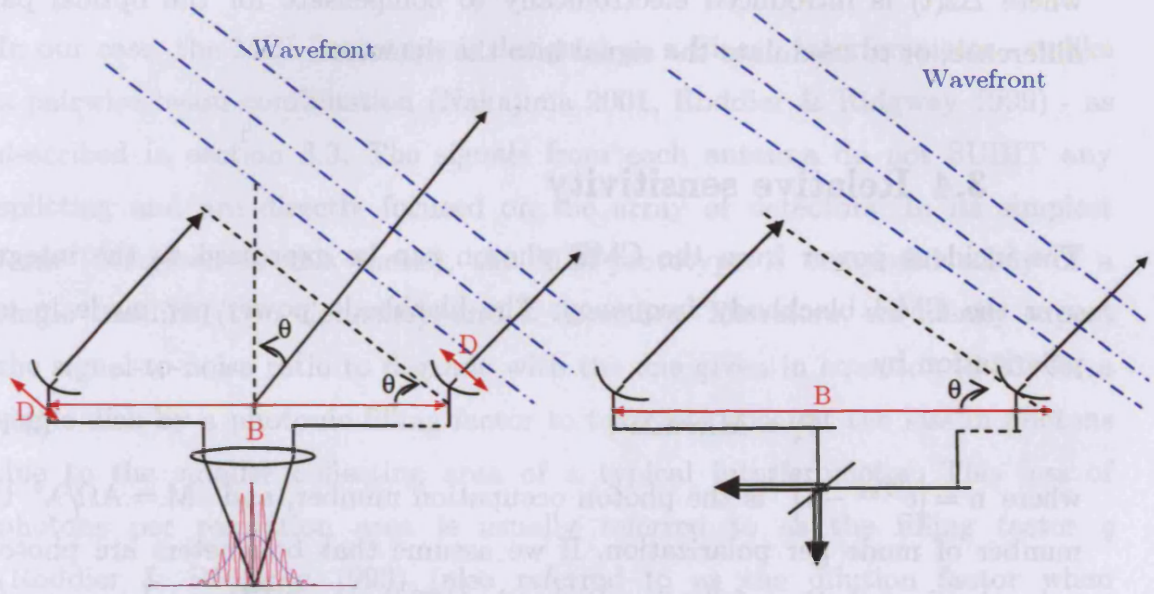

Figure 3.6: Principle of beam combination.
Left: 2-element image-plane interferometer (Fizeau); right: 2-element pupil-plane interferometer

In a pupil-plane configuration, parallel beams are superimposed on an optical divider (e.g. beam splitter). The resulting combined signal is then routed towards the focal plane and focussed on one or more detectors. If the polarization of the astronomical source is to be recovered, the beam splitter could be a polarizer grid to split the two polarized component of the electromagnetic wave. Figure 3.6(b) illustrates the principle of a two-element pupil-plane interferometer. It can be shown that the interferometer output is proportional to:

$$E_{int}(t) = E_n(\theta)\left[1 \pm V \sin(2\pi\Delta z(t)/\lambda)\right] \qquad (3.14)$$

where $\Delta z(t)$ represents the optical delay introduced to compensate for the optical path difference.

In an image-plane (or Fizeau) interferometer, each of the two distant beams is focussed to make an image. Both images would then be superimposed, forming an interference pattern on the detector focal plane, as shown in Figure 3.6(a), and proportional to:

$$E_{int}(\theta) = E_n(\theta)\left[1 + V\cos(2\pi(\theta B + \Delta z)/\lambda\right] \tag{3.15}$$

where $\Delta z(t)$ is introduced electronically to compensate for the optical path difference, or to modulate the signal into the detectors.

3.4 Relative sensitivity

The incident power from the CMB photon can be expressed as the integral over the CMB blackbody frequency: The blackbody power per mode in one polarization by

$$P_s = Mh\nu n\Delta\nu, \tag{3.16}$$

where $n = \left[e^{h\nu/kT} - 1\right]^{-1}$ is the photon occupation number, and $M = A\Omega/\lambda^2$ the number of mode per polarization. If we assume that bolometers are photon-noise dominated, then following Richards (1994), the NEP can be expressed as:

$$NEP^2 = h\nu P_s + \frac{P_s^2}{\Delta\nu}, \tag{3.17}$$

The first term represents the shot-noise component ($h\nu/kT \gg 1$) of the background radiation fluctuation, while the second term represents the wave-noise ('bunching', $h\nu/kT \ll 1$). Assumptions are typically made to simplify the algebra. However both terms are relevant in the following discussion since the CMB observed from space lies in a frequency region where $n \approx 1$. We therefore choose to include both terms in the following relationships. Re-arranging (3.17) gives:

$$NEP \approx h\nu\sqrt{2Mn(1+Mn)\Delta\nu}\,. \tag{3.18}$$

Since $NEP = P_{signal}\left(S/N\right)^{-1}$, the signal-to-noise ratio (SNR) for a single dish, per polarization detected in a single detector is given by:

$$\left(S/N\right)_{SD} \propto \left[\frac{Mn\Delta\nu}{(1+Mn)}\right]^{1/2}. \tag{3.19}$$

This is simplified to form the usual relation for a single dish at high frequency ($n \ll 1$) to $\sim \sqrt{Mn\Delta\nu}$. The SNR with a detector array of Z bolometers, assuming no correlation between bolometers in the array, is increased by a factor of $\sqrt{Z}$:

$$\left(S/N\right)_{\substack{SD \\ Z\ bolos}} \propto \sqrt{Z}\left[\frac{Mn\Delta\nu}{(1+Mn)}\right]^{1/2} \tag{3.20}$$

In our case, the MBI-Prototype is designed as a Fizeau interferometer - unlike a pairwise beam combination (Nakajima 2001, Roddier & Ridgway 1999) - as described in section 3.3. The signals from each antenna do not SUBIT any splitting and are directly focused on the array of detectors. In its simplest form (described in this thesis), the MBI-prototype is composed solely of a single baseline (two elements), and Z detectors. Therefore, we ideally expect the signal-to-noise ratio to degrade with the one given in equation (3.20) for a single dish by a photonic filling factor to take into account the loss in photons due to the smaller collecting area of a typical interferometer. This loss of photons per resolution area is usually referred to as the filling factor q (Roddier & Ridgway 1999) (also referred to as the dilution factor when inversed) where B the longest baseline, and N the number of identical apertures of area D^2:

$$q = N\left(B/D\right)^2 . \tag{3.21}$$

Consequently, we expect the signal the SNR of MBI-P to degrade as $q^{-1/2}$:

$$\left(S/N\right)_{MBI\text{-}P} \propto \sqrt{\frac{Z}{q}}\left[\frac{Mn\Delta\nu}{(1+Mn)}\right]^{1/2} \tag{3.22}$$

If we were to considered additional collecting areas the SNR of the prototype would be improve by the square root of the numbers of non-redundant baseline(3.22) This configuration implies multiplexing the signal, provided that the signal in non-redundant baselines is modulated at a different frequency to recover the astronomical information. In this case, the SNR of MBI-p is re-written from (3.22) as follow:

$$\left(S/N\right)_{MBI-P} \propto \sqrt{\frac{Z}{q}\frac{N(N-1)}{2}}\left[\frac{Mn\Delta\nu}{(1+Mn)}\right]^{1/2} \tag{3.23}$$

The number of detectors is governed by the necessity of populated sufficiently the focal plane to Nyquist sample the interference pattern imaged onto the focal plane. In the Fizeau configuration, there are $2B/D$ (where B is the maximum baseline) fringe cycles in the image plane. Hence, $4B/D$ pixels are required on one dimension of the (uv) plane to comply with Nyquist requirements. Therefore a two-dimensional array must be composed of at least $16(B/D)^2$ single-mode bolometers. We note that the use of a two-dimensional array of bolometers would increase the mapping speed by the square root of the numbers of detectors. Where the sky-noise dominates, this is acceptable. However, in the case where the detector noise dominates, the SNR of the interferometer over the entire array degrades dramatically as $\sqrt{Z}$.

3.4.1 Noise correlation

Since each baseline corresponds to a different window function, we could expect to increase our sensitivity by multiplying the number of baselines and/or by adding more collecting surfaces to our interferometer. However, a problem arises in the nature of the noise in each baseline, more explicitly from the level of noise correlation between various baselines prior to the actual detection. Where the window functions overlap, the CMB signal is correlated from certain baselines. However, in the case of an uncorrelated source, this statement doesn't appear to be true, and the noise in each (non-redundant) baseline is uncorrelated. This problem can be recast as how the beams are combined. For a beam combiner where the beams are divided pairwise to form the baselines, Zmuidzinas (2003) states that the noise is divided in the same way as the signal, depending on the photon occupation number in each detector. However, it is possible that uncorrelated noise gets correlated in the beam combination process (Mauskopf 2003). In the present case, the addition of baselines to our prototype would involve multiplexing the baseline at different modulation frequencies, so that no division occurs in either the signal or the noise. Therefore, what was uncorrelated would then remain so. The MBI-P beam combiner is presented in section 3.5.1.

3.5 Description of the instrument

We present in this section the optical design of the MBI two-element prototype, its cryogenic hardware, its mechanical features highlighting the various motion capabilities and hardware, but also some interesting electronic development.

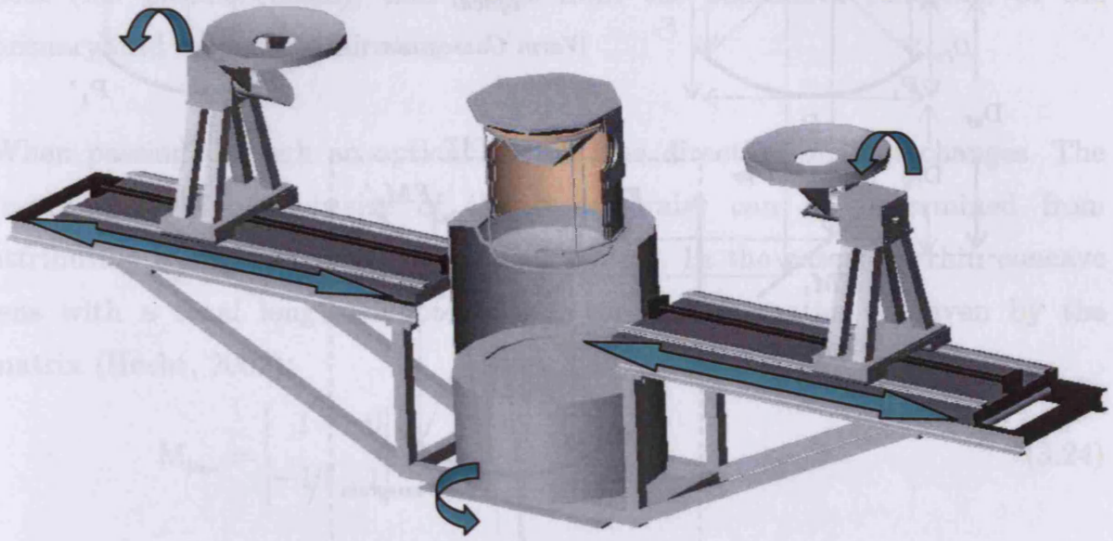

Figure 3.7: MBI-P schematics
The secondary mirrors of the afocal Cassegrain are not shown for clarity reasons. They have been designed to be supported by foam-cones (cf. section 3.5.4).

3.5.1 Optics & Beam-Combination

The concept of the MBI-P quasi-optical general layout is based on the Michelson interferometer (Tango & Twiss 1980), and is illustrated in Figure 3.8 below.

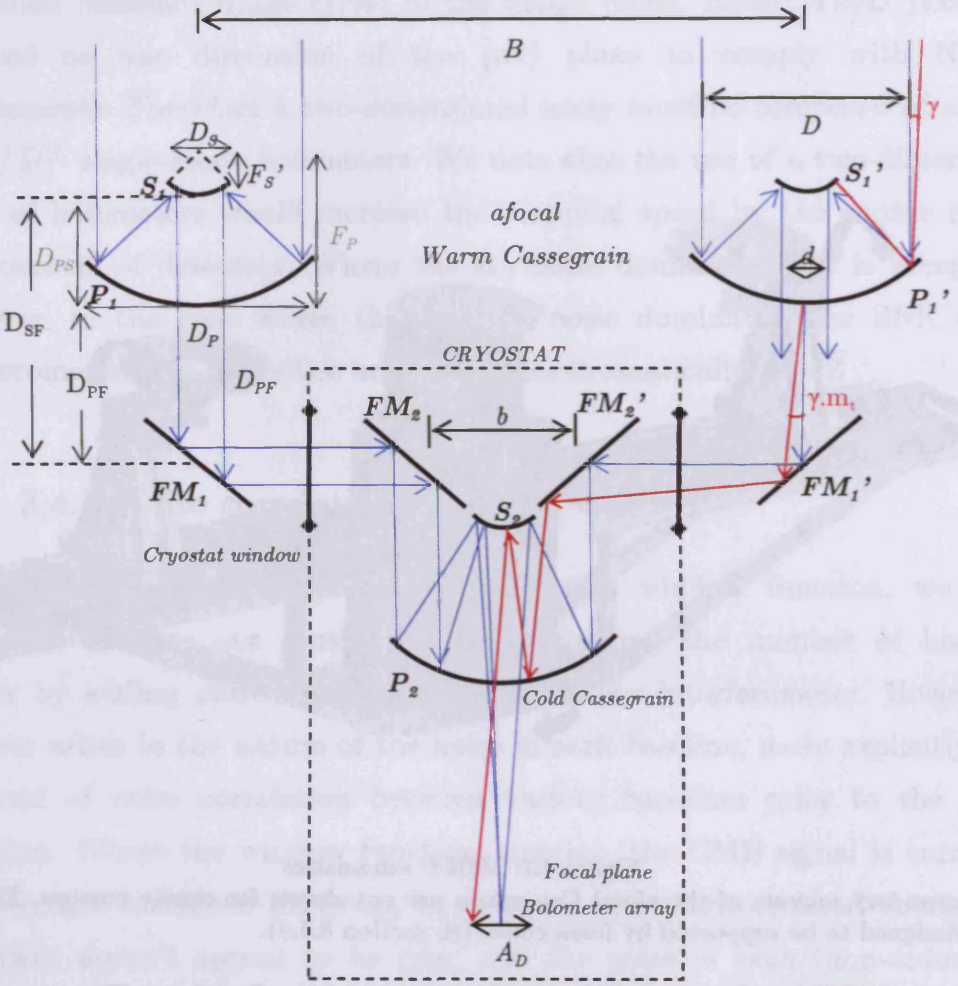

Figure 3.8: Geometrical nomenclature of the image-plane MBI-P

The sky signal illuminates two afocal Cassegrain antennas that define the baseline *B*. The resulting electric fields are reflected by their respective secondary mirrors, and reflected towards the cryostat windows from a set of two flat mirrors, as shown in Figure 3.8.

Inside the cryostat, the two incoming beams are reflected by another set of two 45°-inclined flat mirror onto the surface of the primary mirror P_2 of a cold Cassegrain. The resulting beam focuses on the detector array. The wavelength at which the instrument is designed to operate (2 mm) is not negligible

compared to the size of the optical elements, so quasi-optical techniques have been used in the optical design. The principles behind those are summarized in appendix A.

QUASI-OPTICAL AFOCAL CASSEGRAIN TELESCOPE

The dimensions of the reflecting surfaces of the afocal Cassegrain telescope must be derived using Gaussian optics rules (cf. Appendix 0). Following Goldsmith's framework (Goldsmith, 1998), we define the matrix to represent the transformations of incoming radiation emitted from a source in the far-field (i.e. parallel beam), that result from the successive reflection of the primary and secondary mirror.

When passing through an optical system, the direction of light changes. The resulting position and size of the beam waist can be determined from attributing a 2x2 matrix to the optical system. In the case of a thin concave lens with a focal length denoted by f, the transformation is given by the matrix (Hecht, 2002):

$$M_{lens} = \begin{bmatrix} 1 & 0 \\ -1/f & 1 \end{bmatrix} \tag{3.24}$$

In our case the optical system is the afocal Cassegrain antenna. The transformation matrix can be worked out, and written as a function of the secondary focal length and is given by:

$$M_C(F_S) = \begin{pmatrix} 1 - D_{PS}/F_P & D_{PS} \\ -\dfrac{F_P - D_{PS} + F_S/[1 - m_S(F_S)]}{F_P . F_S/[1 - m_S(F_2)]} & 1 - \dfrac{D_{PS}}{F_S/1 - m_S(F_S)} \end{pmatrix} \tag{3.25}$$

where F_S is the secondary focal length of the afocal telescope, and the other distances are highlighted in Figure 3.8.

The size of the waist radius ω_0 and its location are given by:

$$\omega_{out}(F_S) = \frac{\omega_0}{\sqrt{\left(M_C^{1,1}\right)^2 + \left(M_C^{1,0}.z_c(\omega_0)\right)^2}} \tag{3.26}$$

$$d_{out}(F_S) = \frac{\left(M_C^{0,1}\right)\left(M_C^{1,1}\right) + M_C^{0,0}.M_C^{1,0}.z_c(\omega_0)^2}{\left(M_C^{1,1}\right)^2 + \left(M_C^{1,0}.z_c(\omega_0)\right)^2} \tag{3.27}$$

where $z_c(\omega_0)$ is the confocale distance of the input beam waist (located on the primary mirror), set to be equal to a third of the primary mirror. We find the position and size of the beam waist at the output of the afocal Cassegrain by seeking the limit of equations (3.26) and (3.27) with F_2 set to infinity.

$$\begin{aligned} \omega_{out} &= \lim_{F_S \to \infty} \omega_{out}(F_2) \\ d_{out} &= \lim_{F_S \to \infty} d_{out}(F_2) \end{aligned} \tag{3.28}$$

Using equation (3.28) with MBI-P parameters, we demonstrate that the size of the output beam waist of the afocal telescope is equal to the ratio of the diameter of the secondary mirror and the oversized factor (equal to 3 in this study). The output beam waist is located at the image focal point of the secondary. This result is confirmed by simulation carried out with Zemax[1] ray tracing software.

DIMENSIONS

The dimensions of the optical components have been carefully chosen to satisfy the basic quasi-optical rules described in the appendix 0. Knowing the operating wavelength, $\lambda = 2$ mm , and using two identical warm primary mirrors, $D_P = F_P = 500$ mm , we can work out the dimensions of the quasi-optical elements sketched in Figure 3.8. MBI-P focal plane is designed to house a linear array of 16 bolometers, each spaced evenly by 5 mm (Mauskopf, private communication). This corresponds to an Airy disk at the cold-Cassegrain focus of 80 mm. The Airy disk and the $F_{\#}$ are related according to:

$$A_D = 2.44\lambda F_{\#}, \tag{3.29}$$

thus $F_{\#} = 16.4$ mm . According with Figure 3.8, we consider a radiation coming with an angle γ in respect with the centre of the antenna. The projection of the maximum angular separation in the focal plane (Airy Radius A_R) must not exceed 40mm and is related to the input angular magnification

[1] Focus Software inc. http://www.zemax.com

$m_t\gamma$ and the effective focal length of the beam combining cold Cassegrain F_{eff} by (cf. Figure 3.8):

$$A_R = m_t \gamma F_{eff} \tag{3.30}$$

The telescope magnification m_t is used to fix the minimal size of the cold primary mirror, which in turn will set the size of the cryostat. Using the geometrical dimensions given in Table 3.2 and illustrated in Figure 3.8, the optimum size of the warm secondary mirror is given by:

$$R_2(m_t) = \frac{D_P}{2.m_t} \tag{3.31}$$

where the distance from the vertex of the warm primary to the centre of the warm flat mirror is given in function of the angular magnification by (cf. Figure 3.8):

$$D_{PF}(m_t) = D_{SF} + F_P\left(1/m_t - 1\right) \tag{3.32}$$

we find the diameter of the warm secondary mirror D_S as a function of the angular magnification:

$$D_S(m_t) = z(m_t)\tan(m_t A_R) + \Omega\left(R_S(m_t), m_t\right) \tag{3.33}$$

where R_S is the warm secondary diameter, Ω is the beam radius at the distance $z(m_t)$ from the warm primary vertex, corresponding to the centre of the cold flat mirror. From equation (3.33), we find a minimal value for the telescope magnification equal to 5.263 from which we deduce the effective focal length of the beam-combining Cassegrain, F_{EFF}, to be 1.557 metres.

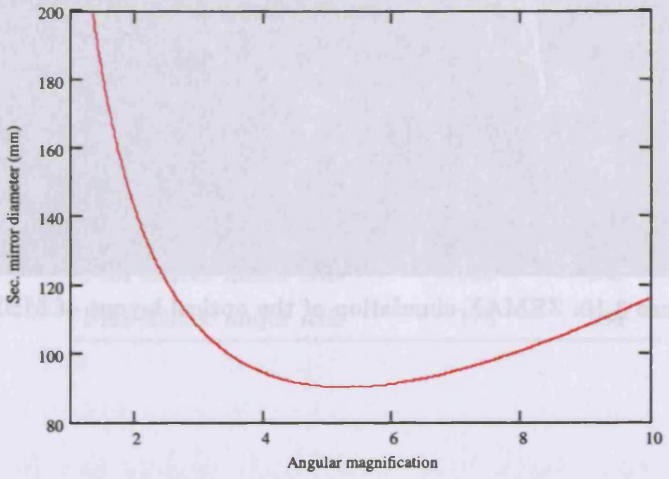

Figure 3.9: MBI-P warm 2nd mirror function of telescope magnification

This reasoning is correct if we consider the cold Cassegrain as a concave lens. In our case, the obstruction of the primary aperture from the secondary mirror affects the dimension of the Airy disk. Consequently, we use the angular magnification and related information to model the optics using ray-tracing software. We show in Figure 3.10 the result of the simulation carried out with Zemax for only one arm of the interferometer. The final parameters of the warm Cassegrain, the cold Cassegrain and the distances between the elements are summarized in Table 3.2 , Table 3.3 and Table 3.4 respectively.

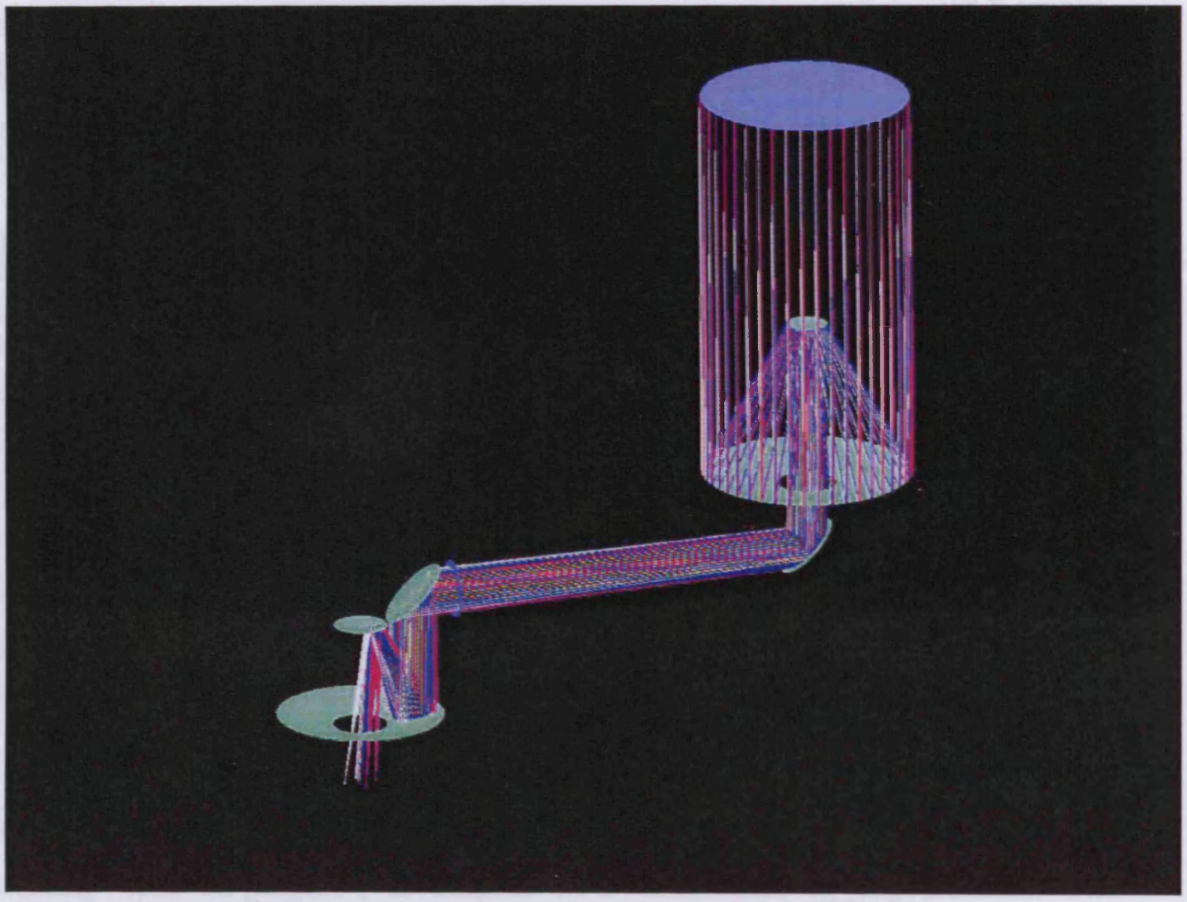

Figure 3.10: ZEMAX simulation of the optical layout of MBI-P.

Table 3.2 : Characteristics of the warm Cassegrain mirrors (in mm)

Parameters	Symbol	Primary mirror	Symbol	Secondary mirror
Type		Parabolic		Parabolic
Diameter	D_P	500	D_S	100
Focal length	F_P	500	F_S' (back)	95
Radius of curvature	R_p	500	R_S	190
Conic constant	B_P	-1	B_S	-1
Mirror equation	P(y)	$Y^2/1^E3$	S(y)	$Y^2/380$

Table 3.3: Characteristics of the cold Cassegrain mirrors (in mm)

Parameters	Symbol	Primary mirror	Symbol	Secondary mirror
Type		Parabolic		Parabolic
Diameter	D_{P2}	400	D_{S2}	130.6
Focal length	F_{P2}	675.51	F_{S2}	500
Radius of curvature	R_{p2}	675.51	R_{S2}	221.30
Conic constant	B_{P2}	-1	B_{S2}	-2.406
Mirror equation	P(y)	$Y^2/2R_{P2}$	S(y)	$Y^2/442.6+Y^4(1-2.406)/8.670E7$

Table 3.4: Distance between mirrors and flat mirrors dimensions (in mm)

Parameters	Warm	Cold
Primary to secondary	405	350
Primary to Flat	100	150
Flat mirror minor axis	120	130
Flat mirror major axis	170	184

Our design allows adjustments of the baseline from a distance of 0.6 metres to 5 metres, or to a maximum resolution of 1.7 arc minutes. The resulting interference fringes are combined on an Airy disk of 80 mm, suitable for illuminating a linear or two-dimensional array of detectors. This offers the possibility of adding a polarizer under the beam-combiner primary mirror before the detector stage; Shown in Table 3.5 are the final technical specifications of MBI-P.

Table 3.5: MBI-P features

Parameters	Unit	Range
Frequency	GHz	150
Baseline extent	Metres	0.6 to 4.600
Angular resolution	Arcmin	14' down to 1.7'
Primary mirror diameter	mm	500
FOV	Arcmin	33.5'
Coherence length	mm	10
Beam combiner primary mirror	mm	400
Beam combiner airy disk	mm	80
Operating temperature	milli-Kelvin	280

GOLDEN RULE VIOLATION

The design adopted to combine the two signals together must comply with:

$$B/b = D/d, \tag{3.34}$$

where B is the interferometer baseline, b the beam-combiner baseline, D the primary mirror diameter, and d the afocal beam diameter as shown in Figure 3.8. This is known as the 'Golden Rule' of interferometry. If this condition is not respected, it can be shown that the superimposed image can suffer distortions (Traub 1986). It turns out that the golden rule can be broken, and we investigate its limit in Appendix B. Curves in Figure 3.11 show the deviation in angle induced by an extended baseline, and highlight the situation where equation (3.34) is no longer respected. In an ideal case, the variation in the pointing angle changes linearly with the position in the focal plane. However at a large baseline or high angles, the focal plane image appears to blur out. The linear relationship is conserved at small angles

and/or baselines. Higher baselines or angles tend to distort the image towards the centre. Six baselines are plotted: 0.5,1,2,3,4,5 metres long.

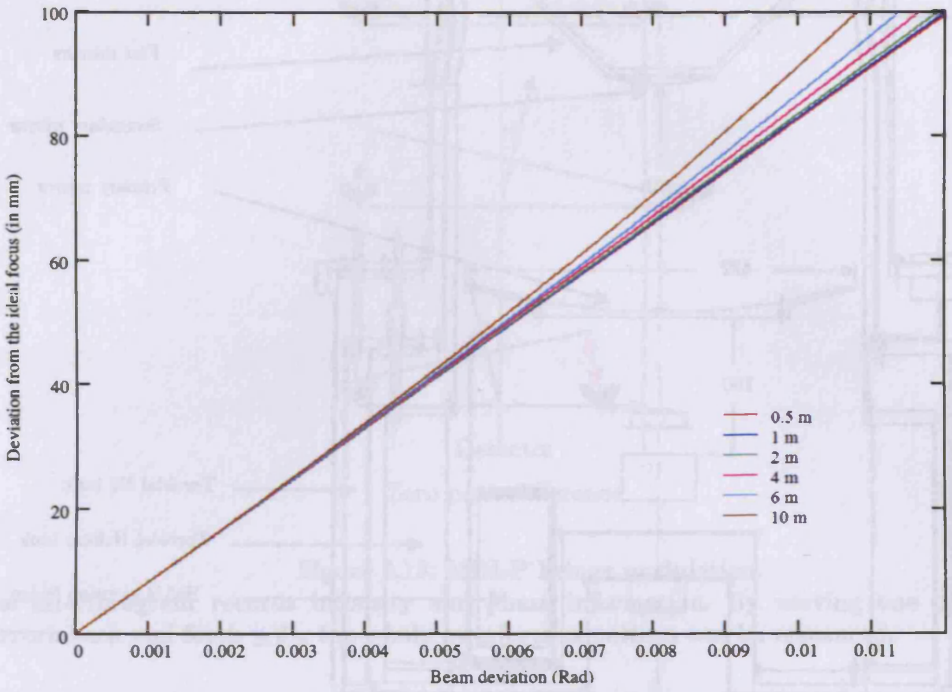

Figure 3.11: Limits of application of the Golden Rules.
Plots are the pointing angle vs. the deviation from the ideal focus point. The plot is made at different baselines, from which can be seen under what limits (baseline and angle) the Golden rule can be broken.

3.5.2 Cryogenics

MBI-P cryostat has been specifically designed to house the beam combiner mirrors, the sorption fridge necessary to cool the bolometers down to their operating temperature of 260mK and also the cold electronics, such as the JFET amplifiers and RF filters. The coldest temperature is achieved using a three-stage He3-He3-4He sorption fridge (Bhatia et al. 2000) similar to that used in Bolocam, and described in section 2.3.2. For mechanical reasons, the cryostat, shown in

Figure 3.12, is composed of toroidal cryogens tanks, providing sufficient working volume to house the beam combiner. The cryostat sits in the centre of the interferometer baseline. The two incoming beams enter the optical windows, situated at the top of the cryostat 180° apart.

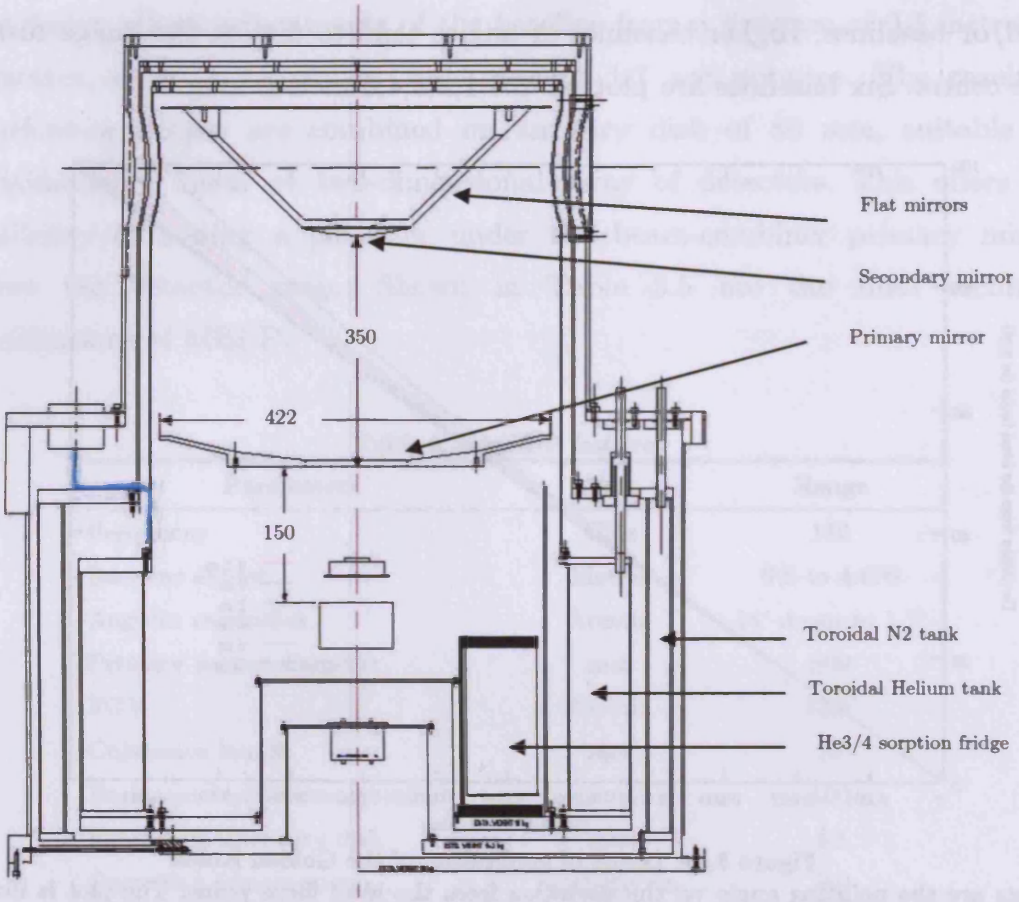

Figure 3.12: MBI-P cryostat and beam-combiner (dimensions in mm).

3.5.3 Fringe & baseline modulation

The fringe modulation is achieved by moving one of the afocal telescopes back and forth, on the order of a few wavelengths (± 6mm). As illustrated in Figure 3.13 below, a horizontal geometric delay introduced at one extremity of the baseline, changes the pointing direction. Therefore, it is equivalent to steering the antennas to construct the interferogram from which both intensity and phase can be measured.

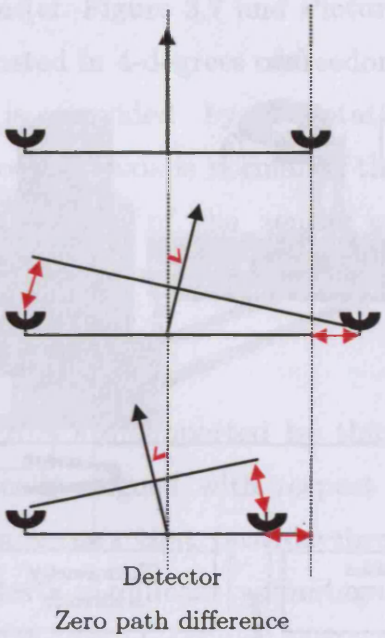

Figure 3.13: MBI-P Fringe modulation.
The interferogram records intensity and phase information. By moving one of the afocal mirrors back and forth $\pm 3\lambda$, the whole interference pattern can be measured.

Another type of modulation filters the constant term in the output signal from equation (3.3) (cf. section 3.3), that would be visible as an offset in the final signal. At a given baseline, this DC signal can be removed by modulating the baseline, i.e. by translating in phase both afocal mirrors back and forth at a constant rate (~1Hz). In addition, this particular modulation can reduce low-frequency drifts in the readout electronics and bolometers.

3.5.4 Motion Control

MBI-P features a linear translation of each of the two afocal antennas, to (i) ensure the variation in length of the single baseline, (ii) provide the fringe modulation, and (iii) filter out the constant term of the interferometer response. In addition, the interferometer can be rotated in azimuth and elevation.

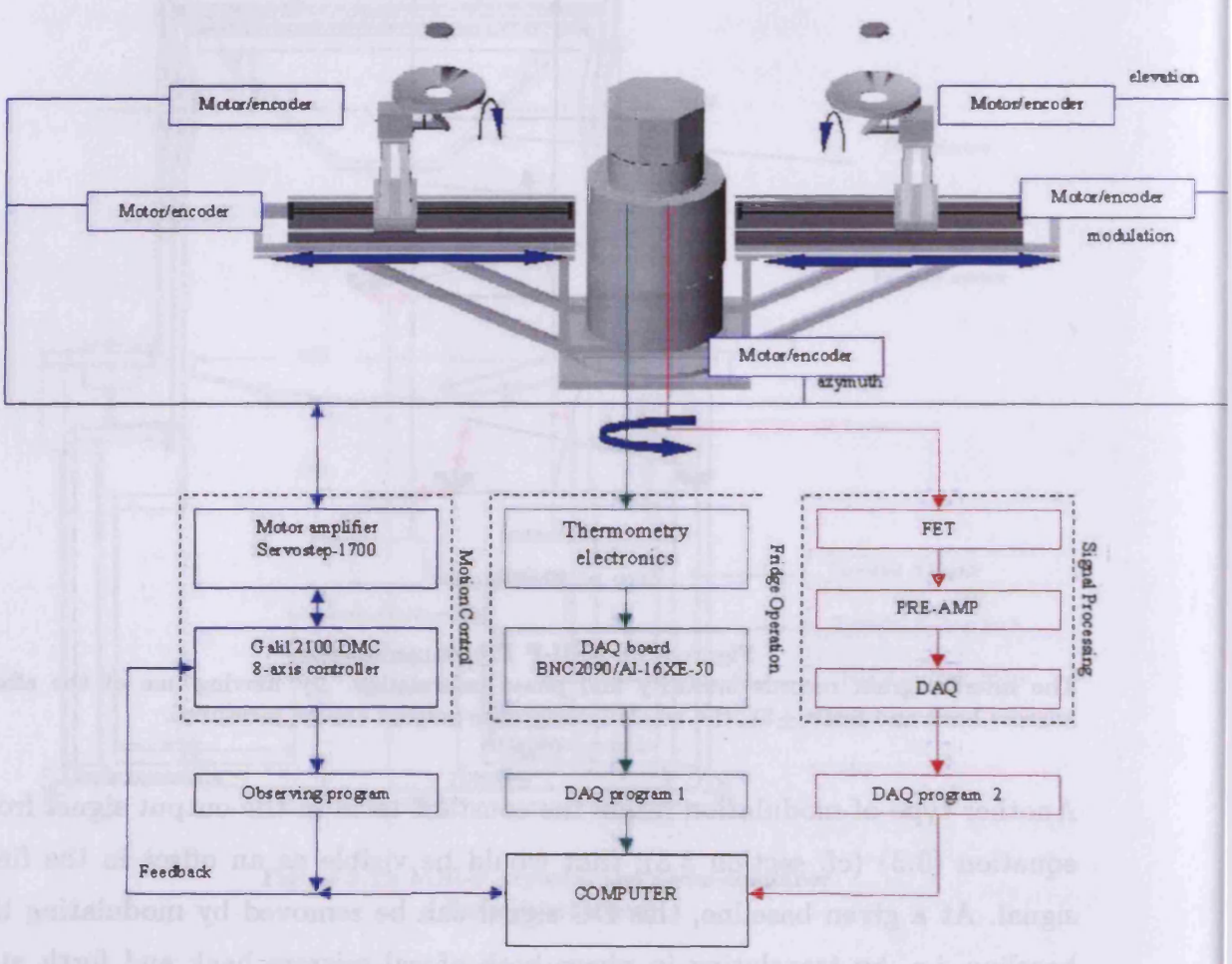

Figure 3.14: MIP-P operation.

Five DC-servo motors are operated by a high standard 8-axis DMC2100 Galil[1] controller via an Ethernet connection, as illustrated in the flow diagram Figure 3.14.

The linear translation of each afocal telescope is provided by a custom-made positioning system from Hepco[2]. The telescopes are mounted on two tracks powered by a low-backlash ballscrew assembly. To provide the stability and accuracy in this particular motion, the entire positioning system stands on two separate custom-made optical tables. These tables are coupled to the

[1] Galil Motion Control – http://www.galilmc.com

[2] Hepco Slide Systems Limited – http://www.hepco.co.uk

main interferometer frame (cf. Figure 3.7 and Picture 3.1), and their positions can be independently adjusted in 4-degrees of freedom.
The azimuth rotation is provided by a rotating base on which the interferometer sits. The rotation axis is normal to the baseline, situated at the phase-tracking reference. Control of the zenith angle is provided by two motorized shafts, on which are mounted the afocal Cassegrain telescopes and their respective flat mirrors.

The warm secondary mirrors are supported by thick (3 cm) conical piece of Zotefoam. They are optically aligned with respect to the other components using adjustable ball-joint screws that provide three degrees of freedom (cf. Picture 3.3). This provides a significant advantage over standard secondary mechanical supports, avoiding shadowing as well as cutting down the weight of the assembly. The transmission loss of Zotefoam has been measured in Cardiff (Peter Ade et al.) and has negligible effect at our operating frequency.

The features and accuracy of the servo-motors required to control MBI-P are listed in Table 3.6.

Table 3.6: motion details of the MBI prototype.

Motion	Type	Speed	Required Accuracy	Actual Accuracy	Gear head ratio
Baseline	Linear	50 to 100 mm/s	300μm	1.25μm	X
Steering	Linear	"	300 μm	1.25μm	X
Filtering	Linear	"	300 μm	1.25 μm	X
Azimuth	Rotation	1°/s	0.36 arcmin	0.17 arcsec	5:1+387:1
Tracking	Rotating	"	0.36 arcmin	15 arcsec	216:1

All the motions are controlled by an independent motor fitted with a 4000 ppr encoder. The achievable accuracy on the motion may be affected by backlash, and instrumental error.

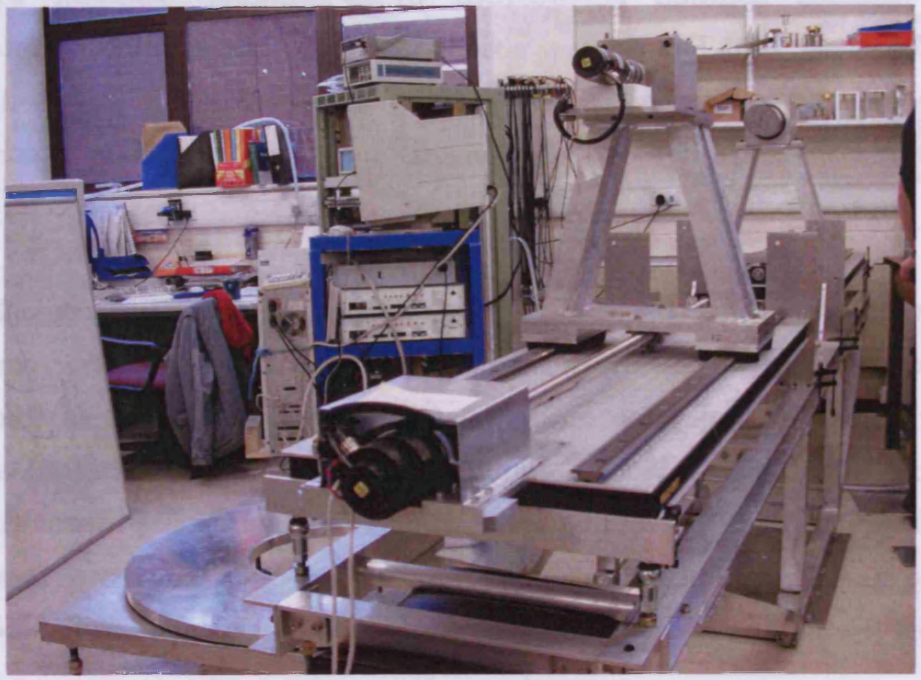

Picture 3.1: MBI-P baseline

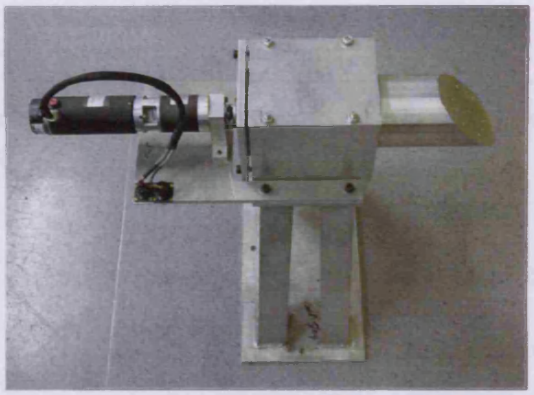

Picture 3.2: Afocal Cassegrain mount
Picture 3.3: Secondary mirror supported in a zotefoam plate.

3.5.5 Data Acquisition

The electronics for temperature control and acquisition have been designed and built in Cardiff University (Rob Tucker), covering a temperature range from 300K down to 250mK. It is essential to have a reliable system in order to control efficiently the sorption fridge. Consequently, two types of electronic circuits were constructed to acquire: (i) high cryogenic temperatures (above 3 Kelvin) from semi-conductor diodes, and (ii) low temperatures ranging from 250 mK to 3K, via Lakeshore[1] germanium resistance thermometers (GRT). The data from 4 GRT and six diodes can be acquired simultaneously. The circuitry are presented and explained in Appendix C.

Thermometer voltages are acquired in real-time via an 8 channel data acquisition board BNC-2060[2]. Operations on the acquired voltages (filtering and interpolating calibrations, conversion to Kelvin unit, recording, monitoring, automating...) as well as the cycle of the sorption fridge, were performed using the Labview 6.2[1] environment. This reliable software is widely used in instrumentation and provides a user-friendly graphical environment.

.

We refer back to Figure 3.14 for a flow-diagram describing all aspects of DAQ involved so far in the construction of the MBI-P.

[1] Lakeshore – http://ww.lakeshore.com

[2] National Instrument – http://www.ni.com

3.6 Conclusion

We have started to explore the feasibility of a millimetre-wave bolometric interferometer. Although interferometry could be done in other ways, we based our design around a simple beam-combiner, borrowed from optical techniques. As shown throughout this chapter MBI-P has a clear potential to demonstrate the technology. The main components (inc. interferometer body, warm mirrors, motion control system, temperature acquisition system & electronics) have been designed, built and tested successfully. The beam combiner was designed but not built, as shown in Appendix D.

Before the design of MBI-P could be enhanced to implement more baselines and adapted to be polarization sensitive, similarly to the Polatron experiment, the instrument crucially requires a measure of its sensitivity. This is likely to occur in the near future, in preparation for proposed satellite missions (cf. NASA Einstein Probe program[1]).

[1] http://universe.gsfc.nasa.gov/science.html

Chapter 4 POLATRON: feasibility study

We discuss in this chapter the work done on the Polatron experiment. Polatron is an existing polarization-sensitive bolometric receiver, designed to study the SZ effect and the polarization of the Cosmic Microwave Background (cf. section 1.2). Our participation in this experiment has been oriented towards the coupling of bolometers with the existing mechanical cryocooler. This feature is particularly attractive for space applications, such as HFI on Herschel or Planck, and for instruments located in hostile remote locations where cryogens are expensive.

The original technical features of Polatron are two fold; (i) a closed-loop mechanical cooler, used to cool the cryostat from room temperature to 4K; (ii) a detection system made up of bolometers cooled to sub-Kelvin temperature by a sorption fridge. The difficulty of coupling cryocoolers and bolometers has been addressed before (Bhatia et al. 1998). However, the original design did not succeed in minimizing the propagation of noise from the cryocooler to the detector stage; therefore a proper evaluation of the system performance could not take place.

In this Chapter, we revisit the design of the instrument cryogenics in order to assess its performance. After a brief description of the instrument, we identify the technical problems. We then describe methods to characterize the noise performance of the instrument and carry out a number of noise measurements to quantify the effect of our modifications to the overall system performance. Based on the result of our investigation, we finally address the feasibility of Polatron in studies of the polarization of the CMB.

4.1 Overview of the instrument

The science case and specific technical features of Polatron have been well documented in the past and we refer to Philhour (2001 and 2002) for information not developed in this section. Shown in Figure 4.1 is a technical drawing illustrating the instrument.

Put forward in 1999 as a bolometric polarimeter to study the polarization in the CMB anisotropies, Polatron was conceived to ultimately resolve features in the polarization spectrum (cf. section 1.2.2). Polatron was also expected to characterize polarized foregrounds and to test key instrumental features for future CMB measurements such as the utilization of a mechanical cryocooler (e.g. Planck satellite). The receiver was designed to operate remotely from the upgraded 5 metre telescope in the Owen's Valley Radio Observatory (OVRO) at a frequency of 96±10 GHz (3 mm), chosen to minimize galactic foregrounds (cf. section 1.3.2). The incoming radiation is collected by an on-axis Cassegrain, coupled to the on-axis cold optics inside the cryostat. Shown above in Figure 4.2, is a schematic of the Polatron on-axis optics. After its modulation by a half-wave plate (cf. 4.1.1) the radiation propagates through a millimetre-wave filter stack, similar to the one used in Bolocam, and described in section 5.1.

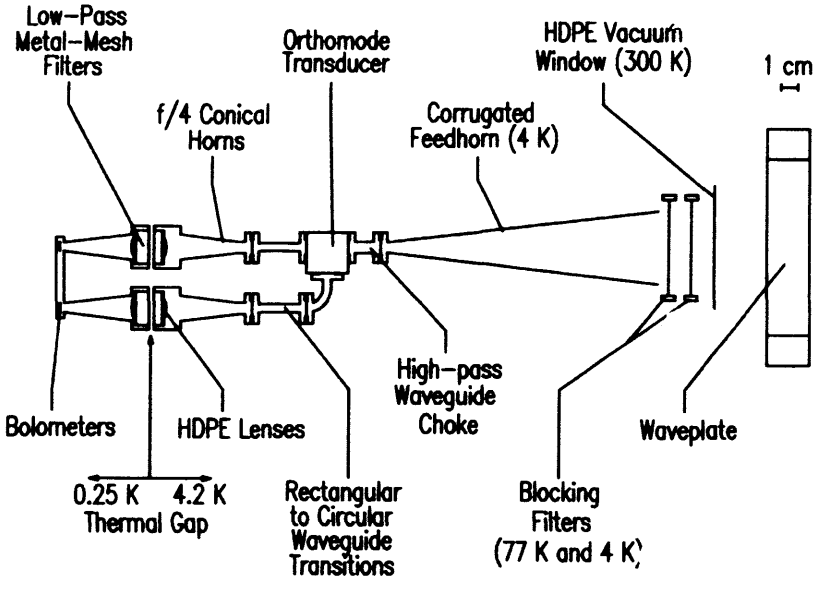

Figure 4.2: Schematic of the Polatron focal plane optics

The incoming polarized EM wave is then separated into its orthogonal linear components using an ortho-mode transducer – OMT - (Chattopadhyay, 1998). Both polarization orientations of the incoming wave are detected by a bolometer shown in Figure 4.2.
The next section describes the role played by the waveplate in the design. We then describe the bolometer readout electronics.

4.1.1 Waveplate modulation

Shown in Figure 4.3 is an illustration of the transformation of a polarized electro-magnetic wave after propagating though a half-wave plate.

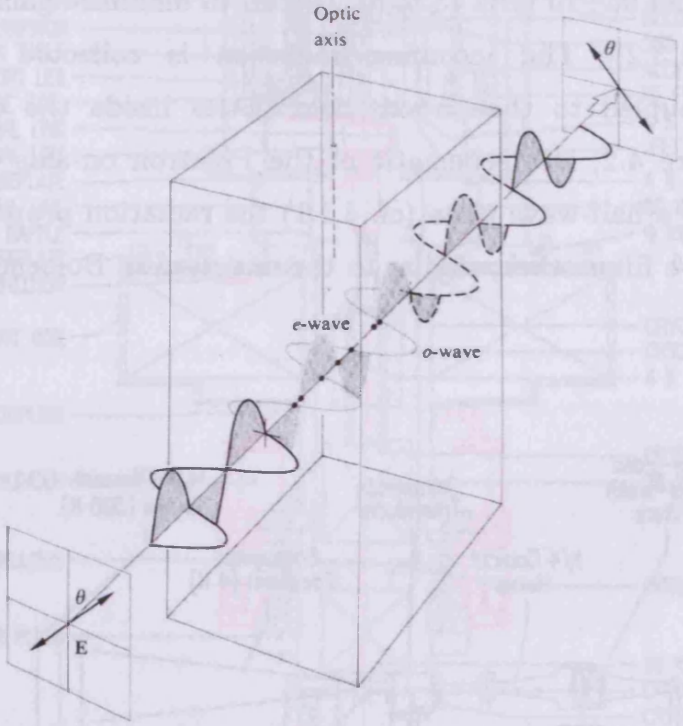

Figure 4.3: half-waveplate modulation (Hecht 2002).
The waveplate is made out of a birefringent material, having two indexes of refraction. As a result, the polarized component of an incoming radiation aligned with the waveplate slow axis is delayed by an amount of π with respect to its orthogonal component aligned with the fast axis of the waveplate.

Polatron uses a uniaxial birefringent half-wave plate made in quartz on which impinges the incoming EM wave denoted by $\vec{E}(t) = \vec{E}_x(t) + \vec{E}_y(t)$ with:

$$\begin{aligned} \vec{E}_x(t) &= E_{0x}\cos\left[(kz - \omega t) + \phi_x(t)\right] \\ \vec{E}_y(t) &= E_{0y}\cos\left[(kz - \omega t) + \phi_y(t)\right] \end{aligned} \tag{4.1}$$

where k is the wave vector, $\phi_x(t)$ and $\phi_y(t)$ the phase shift of each component, and ω the angular frequency. Since Thompson scattering only generates linear polarized signal from the CMB, $\vec{E}_y(t)$ and $\vec{E}_x(t)$ are in phase. Therefore we simplify equation (4.1) to:

$$\vec{E}_x(\xi) = \left(E_{0x} + E_{0y}\right)\sin(\xi) \tag{4.2}$$

with $\phi_x(t) = \phi_y(t) = -\pi/2$ and $\xi = kz - \omega t$. Following equation (1.8) (cf. section 1.4) we can characterize the EM wave by its Stokes parameters using:

$$\begin{aligned} I_0 &= \left\langle E_{0x}^2 \right\rangle + \left\langle E_{0y}^2 \right\rangle \\ Q_0 &= \left\langle E_{0x}^2 \right\rangle - \left\langle E_{0y}^2 \right\rangle \\ U_0 &= 2\left\langle E_{0x} \right\rangle \left\langle E_{0y} \right\rangle \\ V_0 &= 0 \end{aligned} \tag{4.3}$$

The transformation of Q_0 and U_0 from rotating the waveplate can be expressed by rotating the original coordinates system, so that:

$$\begin{aligned} Q' &= Q_0\cos 2\theta + U_0 \sin 2\theta \\ U' &= -Q_0 \sin 2\theta + U_0 \cos 2\theta \end{aligned} \tag{4.4}$$

where θ is the rotation angle. If we consider $\vec{E}'(t)$ to be polarized at a certain angle $\varphi = \tan^{-1}\left(E_{0y}/E_{0x}\right)$ with respect to the fast axis, it can be shown that:

$$\vec{E}'(t) = \left\{\left[E_{0x}\cos\varphi + E_{0y}\sin\varphi\right]\hat{i} + \left[E_{0y}\cos\varphi - E_{0x}\sin\varphi\right]\hat{j}\right\}\sin\xi \tag{4.5}$$

where the coordinates system $\left(\hat{i}, \hat{j}\right)$ is oriented in the directions of the fast and slow axis of the wave-plate. The difference between the two indexes of refraction at a frequency centred at $\nu_0 = 96\text{GHz}$ of the birefringent material is $\Delta n = 0.048$ (Philhour 2002). We can justify the thickness of the wave plate by the following equation:

$$l = \Delta\phi\left(\Delta n \frac{2\pi\nu}{c}\right)^{-1} \tag{4.6}$$

where c is the speed of light, and $\Delta\phi$ the differential phase shift generated between two orthogonally polarized rays aligned with the fast and slow axes of the plate given by:

$$\Delta\phi = \frac{2\pi\nu}{c}\Delta n \times t = \pi + \delta\phi \tag{4.7}$$

with $\delta\phi = \pi\left(\nu/\nu_0 - 1\right)$. Using equation (4.6), it can be shown that the half-wave plate used in Polatron needs to be ~32.6 mm thick.

As the incoming wave travels through the wave plate, the $\hat{j}$-component (slow axis) of $\vec{E}'(t)$ is delayed by an amount of π with respect to the $\hat{i}$-component (fast axis), i.e. it has been reflected about the fast axis corresponding to a rotation of -2φ (cf. Philhour 2002). Rewriting equation (4.2) back into (x,y) coordinates as follow:

$$\vec{E}(t) = \left\{\left[E_{0x}\cos 2\varphi + E_{0y}\sin 2\varphi\right]\hat{x} + \left[E_{0y}\cos 2\varphi - E_{0x}\sin 2\varphi\right]\hat{y}\right\}\sin\phi \tag{4.8}$$

from which it can be shown that the expression of the Q and U parameters after $\vec{E}(t)$ travelled through the half-wave plate are:

$$Q = Q_0\cos 4\varphi + U_0\sin 4\varphi \tag{4.9}$$

$$U = U_0\cos 4\varphi - Q_0\sin 4\varphi \tag{4.10}$$

The rotation of the plane of polarization with respect to the feed would then produce U. A rotation of the half-wave plate, 7.6 cm in diameter, placed in front of the entrance feed of the instrument induce the rotation of the plane of polarization, and thus allow to alternate the measurement between Q and U. Therefore, Q and U can be measured in quadrature through a single feed horn. This results in a modulation of the polarized signal at a frequency equal to four times to the physical rotation velocity of the waveplate:

$$\nu_{\text{modulation}} = 4.\nu_{\text{waveplate}} \tag{4.11}$$

4.1.2 Bolometer readout circuit

Shown in Figure 4.4 is the original AC-bridge readout circuit of Polatron.

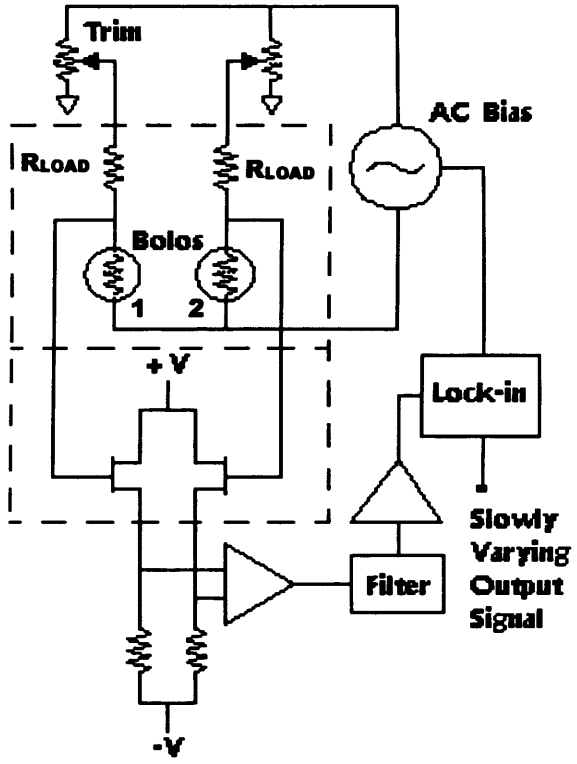

Figure 4.4: Polatron AC-biased readout electronics.
This electronics are based on the one used in SuZIE. In the original layout, the load resistor R_{LOAD} were set to $10\,M\Omega$, and the bias frequency was 219 Hz.

The readout circuit also allows the differencing of the bolometer pair using a pair of matched JFET amplifiers to help reject the common-mode signal which includes the atmospheric background and variations in the telescope unpolarized emission or in the temperature of the cold-stage. The resulting differenced signal is then filtered, demodulated and amplified to produce a final signal that is proportional to the difference of the two orthogonal polarizations (Philhour 2001):

$$V_{out} = S_T \eta_{opt} \eta_p \left[Q \cos\left(2\pi.4 f_{wp} t\right) + U \sin\left(2\pi.4 f_{wp} t\right) \right] + V_{noise} \qquad (4.12)$$

where S_T is the detector responsitivity in $V.K^{-1}$, η_{opt} the optical efficiency, and η_p the polarization efficiency, V_{noise} the noise contribution from the JFET and detectors, and f_{wp} is the half-wave plate rotation.

Table 4.1: Polatron bolometers specifications

Detectors parameters	Values
Expected Optical Load	3pW/channel
Sink temperature	250 mK
Operating temperature	450 mK
Thermal Conductivity	40 $pW.K^{-1}$ @ 250 mK
Thermistor heat capacity	1.5 $pJ.K^{-1}$
Thermistor resistance	2.0 Ω
Time constant	25 ms
NEP	2.9E-17 $W.Hz^{-1/2}$
Electrical Responsitivity	3E8 $V.W^{-1}$

Table 4.2: Specification of the Polatron receiver (Philhour 2002)

Telescope	5.5 metres Cassegrain
Beam size (FWHM)	2.5'
Polarization detection	Waveplate & OMT
Detectors	Silicon-nitride micromesh bolometers
Spectral band	86-100GHz
Polarization efficiency	>95%
Sensitivity	~ $500\mu K/\sqrt{s}$ to Q and U

To achieve the required sensitivity, the bolometers are cooled by a sorption fridge to ~300mK, whose base-temperature is provided by a custom-made mechanical cryocooler. Table 4.2 depicts the performance of the receiver base on the optical test performed in a wet dewar (Philhour, 2002). Before elaborating on a strategy to take noise measurements of the instrument, we introduce the cryogenic system of Polatron. We briefly describe the cryocooler operation, and the sorption fridge.

4.1.3 Cryogenic System

The mechanism used to achieve low temperatures depends critically on the temperature one needs to achieve. Different techniques are required to reach a sub-Kelvin temperature. Shown in Figure 4.5 are the different temperatures at which various parts of Polatron need to operate. In Polatron, the transition from 300K to 4K is achieved by a mechanical cryocooler using ^{4}He as the working gas. The ~300 mK heat sink for the bolometers is provided by a sorption fridge.

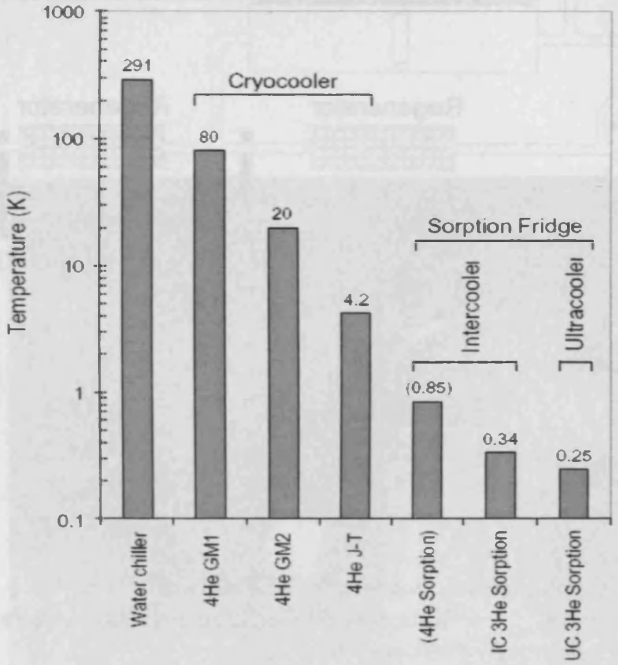

Figure 4.5: Polatron's thermal stages

300K – 4K TRANSITION: MECHANICAL CRYOCOOLER

Figure 4.6 depicts the principle operation of the Gifford-McMahon (GM)/ Joules Thompson (JT) cryocooler used in Polatron, shown in Picture 4.1. The cold temperature is achieved by isenthalpic expansion of high-pressurized Helium gas, through a small aperture. The temperature and cooling power can be varied by adjusting the nozzle aperture.

An ideal gas would not experience any change in temperature under such an expansion process. However, the molecule distance and incompressibility of a non-ideal gas results in opposing effects on their temperature under adiabatic JT expansion. This is used to achieve high efficiency, two GM stages precede the JT adiabatic expansion, pre-cooling the He^4 gas stream from room temperature to well below the inversion temperature (Table 2.3). As shown in Figure 4.5, the GM stages reach respectively 80K and 20K.

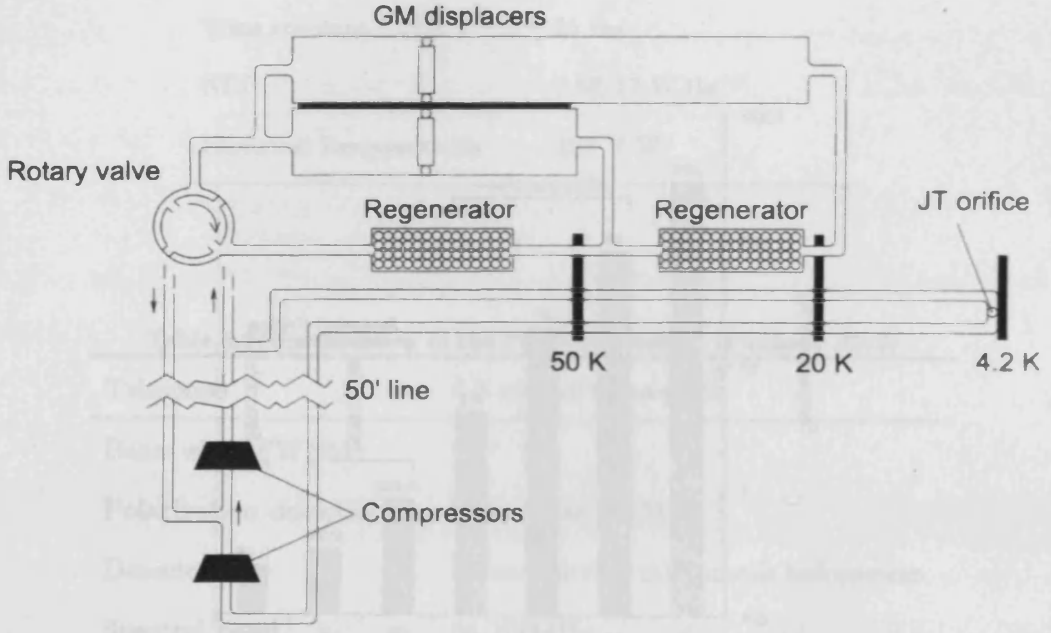

Figure 4.6: Schematics of Polatron cryocooler.
It illustrates the operation of a Gifford-McMahon/Joules-Thompson mechanical cryocooler – see text for detail of operation (Philhour, 2002).

A single cycle of the GM cooler can be defined as the combination of the operation of the two rotatory intake and expansion valves, in coordination with the motion of the displacer that provides refrigeration. The cycle can be described in four successive phases as follow (White 1968):

- pressurization phase: the intake valve is opened and allows the He^4 compressed gas to fill in the warm end volume of the piston
- intake phase: the displacer moves upwards to increase the cold end volume. Pressurized gas enters the regenerator

- expansion phase: the intake valve is closed, and the exhaust valve is slowly opened. By expansion of the gas, the cold volume is cooled down further.
- exhaust phase: the displacer moves across to force the remaining cold gas to be expanded

The first GM stage provides a 50K heatsink with 50W cooling powers, while the second GM stage reaches 20K (well below the 4He inversion temperature at ~51K), where cooling power is used to pre-cool the gas in the JT circuit. The amount of cooling power delivered from the 4K cryocooler tip (CCT) is about 1.5W. This is an important figure since it determines the three-stage fridge cycling procedure described in section 4.2.3.

Picture 4.1: Polatron mechanical cryocooler

4 K-250 mK TRANSITION: 4HE-HE3-HE3 SORPTION FRIDGE

The three-stage sorption fridge used in Polatron is described in (Bhatia et al. 2001) and is similar in principle to that described in section 2.3.2, and used in MBI-P and Bolocam. The main difference is that the Polatron fridge is oriented upside-down with respect to the 4K baseplate, relative to a typical wet-dewar thermal layout. Figure 4.7 illustrates the layout of Polatron sorption refrigerator.

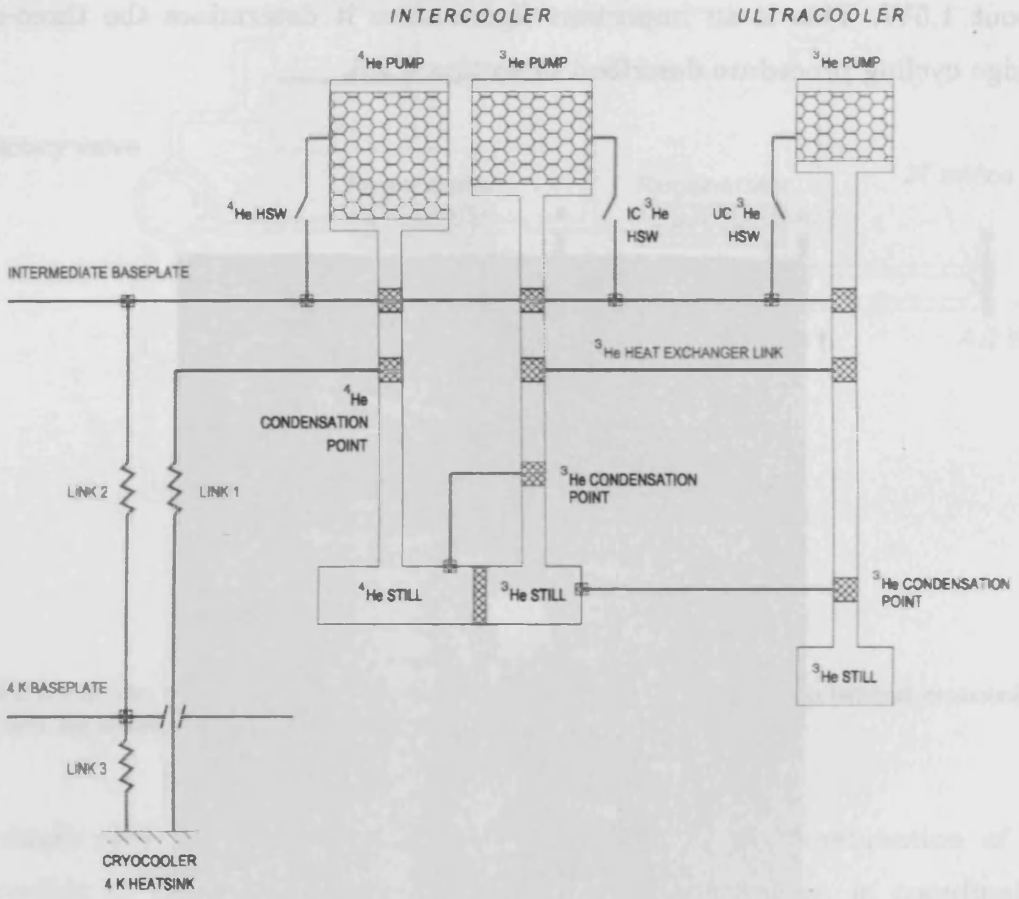

Figure 4.7: Polatron's sorption refrigerator (Philhour, 2001)

4.2 Problem & Solution

Having described Polatron cooling system, we address the problems in the original cryogenic design, and investigate a method to measure the performance of the instrument.

4.2.1 Problem

The implementation of mechanical cryocoolers in cooling sensitive bolometric receivers can lead to a significant contribution to microphonics and electromagnetic interference (EMI). Vibrations induced by the mechanical cryocooler are transmitted to supporting structures and the thermal cold strap linking the cryocooler JT tip to the baseplate, and can propagate to the detectors stage. Bhatia (1999) has shown that transmitted mechanical vibrations, optical misalignments, thermal instability, and electrical interferences (capacitive and inductive) are direct consequences of cryocooler operation. The most significant impact of the cooler is to compromise the detection of faint signals such as the CMB polarization signature.

Although the Polatron cryogenic sorption fridge had been tested in an open-cycled cryostat (i.e. using cryogens, Bhatia et al. 2000) - and in this context complied with the experimental requirements – its performance when coupled with the cryocooler was not sufficient to cool the detector stage. As a result, the noise measurements necessary to assess the bolometer performance could not be performed.

We present hereafter the method used to improve the system in order to perform noise measurements.

4.2.2 Experimental method

To assess the viability of Polatron, we adopted the following approach:

- Rebuilding of the cryogenic thermal layout in order to obtain a substantial heatsink for the bolometers,
- Determination of a cycling procedure of the sorption fridge
- Mechanical isolation of the different source of noise being propagated to the bolometers,

operation. A solution to this problem is to adjust the power delivered by the CCT is to make use of the JT expansion valve initially implemented to progressively cool down the instrument from room to liquid helium temperature. Opening slightly the JT valve results in increasing the CCT temperature as well as its cooling power, so this solved a problem but creating the other; therefore this was not considered as a viable solution.

At any given point in time, it is essential that the cryocooler is maintained within a loop. This is achieved by a computer-based program to cycle the fridge and control the cryocooler behaviour so that the operation would become automated. The CCT cooling power was kept under control not by opening the JT valve, but by reducing the current flowing through the cryopump heaters or slowing down the cycle so minimal heat load would be dumped on to the CCT. This was achieved by including a temperature feedback from critical locations on the fridge and cryocooler in our program. In this way, rapid and automated response could be achieved. The software was developed under the Labview[1] environment. The data was acquired at a rate of 50 Hz from a NI-PCI DAQ[1] card, two Keithley power supplies, one Lakeshore temperature controller (GRT), and Lakeshore temperature readout (diodes).

ISOLATION OF MICROPHONICS AND MECHANICAL INTERFERENCE

The reduction of unwanted interferences was achieved by various methods. In low signal application, long wires reduce conductance, however increase capacitance and thus sensitivity to microphonics pickups. As a first step, all wiring was reduced to minimal length, retightened and thermally grounded. The wiring of the warm analogue data acquisition box was also completely re-designed, in order to limit interference problems. The main idea was to isolate as much as possible the source of unwanted spurious signal so as to better understand the noise affecting the detectors and identify the possible causes.
In order to lower the energy input from external sources of vibrations, we planned to isolate the instrument, and separate adequately the resonant

[1] National Instrument – http://www.ni.com

frequency of the system to the one of the cryocooler. Prior to our improvement, Polatron originally implemented a mechanical vibration isolator, coupling the mechanical cooler to the cryostat as shown in Figure 4.1 and described in Philhour (2001). It consisted of an expanding and contracting bellow, which regulated the flow of compressed air into four pistons. Unfortunately, this apparatus did not appear to provide sufficient isolation. As a simple and cheap improvement, we firmly bolted the Polatron down to a solid structure. In addition, by placing sand bags over the instrument, we aimed to reduce the natural vibration frequency well below the mechanical cooler operating frequency, and divert the vibration away from the cryostat.

As stated in section 4.1, the presence of the waveplate constitutes another level of action against the microphonics. Indeed, in the eventuality of finding a frequency range in the spectrum where the noise is low enough to operate, the waveplate would provide a modulation of the incoming signal which could easily be tuned to operate the bolometer where the noise is lowest. Limits in the frequency are set by the (atmospheric) 1/f noise at low frequency and by the bolometer time constant at higher frequencies. The waveplate was originally due to rotate at 0.15 Hz, modulating the signal at 0.6 Hz (cf. section 4.1.1).

DETECTOR STAGE LAYOUT AND MEASUREMENT SETUP

Every sets of measurements presented in the next section were based on the original Polatron electronics, as described below. To measure the microphonics generated by the mechanical cryocooler at different temperatures and sensitivities we set up on the detector stage two resistors, two thermistors, and two bolometers successively. The resistor was located on the detector plane in a bridge circuit shown in the figure below, with an output gain .of 600.

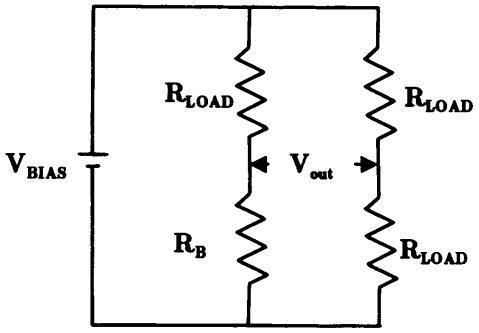

Figure 4.8: Resistor bridge readout circuit.
R_{LOAD}=30MΩ, R_B represents the resistor (see text for value)

The thermistor and the bolometers were AC-biased in the readout circuit shown in Figure 4.4 (initially set to a 219Hz sine-wave), with an output gain of 1E5. Mismatches in the gain between both bolometer channels can be trimmed out by tuning the bias level as shown in Figure 4.4. It is also possible to DC bias the bolometers channels, to simplify the load-curve measurement which are required to assess the optical loading and responsitivities of the detectors. Each bolometer channels can be read individually.

The noise power spectra were measured from acquiring signals at 50Hz using a low-noise spectrum analyser.

4.3 Measurements & Results

4.3.1 Cryogenics & mechanical improvement

In revisiting the cold plate assembly, we were able to reduce the thermal mass by 2 kilograms. As a result, we were able to operate the mechanical cooler at a base temperature of 2.9 K, as compared to 4.7K previously achieved. Shown in Figure 4.9 is an example of the fridge cycle. The total fridge cycle was 3.5 hours, and provided a base temperature of 260 mK with a holding time of 4 hours, matching our goal. This provides enough time to make accurate noise measurements. Since optimizing the duty time was a priority, no intensive effort was made to improve the cycling procedure.

4.3.2 Resistor noise

The first results were obtained by measuring the noise spectrum on the resistor channel placed in a bridge circuit, using a low-noise spectrum analyser. Resistors are subject to thermal noise resulting from random motion of electrons. The mean square voltage is proportional to the physical temperature, so one expects to see a significant decrease in the noise power spectrum with decreasing temperature. The first set of measurements was made with $R_{load} = 30M\Omega$ and $R_B = 1.94M\Omega$ as shown in the Figure 4.8 above. The results followed the Johnson noise model given by $V_J = (4kTR\Delta B)^{1/2}$ where k is the Boltzmann's constant, T the temperature of the resistor, R the resistance, and ΔB the frequency bandwidth constraining the measurement. The output noise was measured to be $27\,mV_{rms}/\sqrt{Hz}$ at 300K, $3\,mV_{rms}/\sqrt{Hz}$ at 4K and $1\,mV_{rms}/\sqrt{Hz}$ at 390mK. With an amplification gain being 600, this corresponds to a noise level of $\sim 1.7\mu V_{rms}/\sqrt{Hz}$ at 390 mK.

Another set of results were obtained from measuring the noise on a 3.7MΩ resistor. The resulting power spectrum is plotted in Figure 4.10. The rms noise voltages in the same frequency range, between 0.5 Hz and 1.5 Hz, were 198.3 $\mu V_{rms}/\sqrt{Hz}$, 26.8 $\mu V_{rms}/\sqrt{Hz}$, and 7.8 $\mu V_{rms}/\sqrt{Hz}$ at 300K, 5 K, and 300 mK respectively. The corresponding spectrum shows a peak at about 200 mHz, at the cryocooler fundamental frequency, and a quiet region between 0.2 Hz and 2.5 Hz, where we anticipated a possible window to operate the bolometers. Other peaks are harmonics of both the cryocooler and instrument resonant frequencies. As expected, there is also the presence of 1/f noise at low frequency.

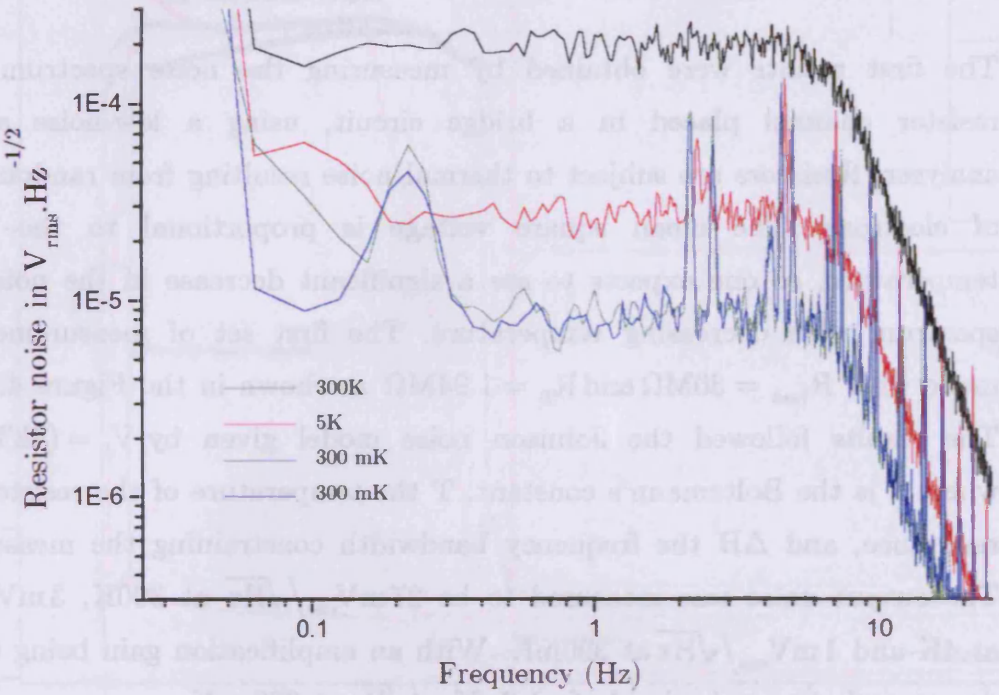

Figure 4.10: Resistor noise spectrum
The measurement is across a 3.7 MΩ resistor. Means values in the frequency range between 0.5 and 1.5 Hz are 198.3, 26.8, 8.5, 7.8 $mV_{rms}/\sqrt{Hz}$ at 300K, 5K, 300mK respectively.

As the temperature decreases, the spectrum reveals the cryocooler microphonics, as shown Figure 4.10. The temperatures calculated from the noise figures appear to be higher than the fridge stage temperatures. The measurements were actually performed at 5.4 K, 518 mK, and 430 mK, instead of 5 K and 260 mK. Therefore, given this peculiar elevated temperature compared with the fridge head GRT, a second GRT was calibrated and installed on the detector cold stage. This elevated temperature was attributed to the very short wiring between the intermediate and ultra-cold stages (cf. Figure 4.7), that resulted in a strong thermal link at the intermediate stage and a slow drift in the fridge intermediate stage temperature during the noise measurements.

The noise floor of the pre-amplifier is assumed to be equal to that of the noise shown in Figure 4.11 below. These measurements were simply performed by grounding the inputs of one of the signal channels.

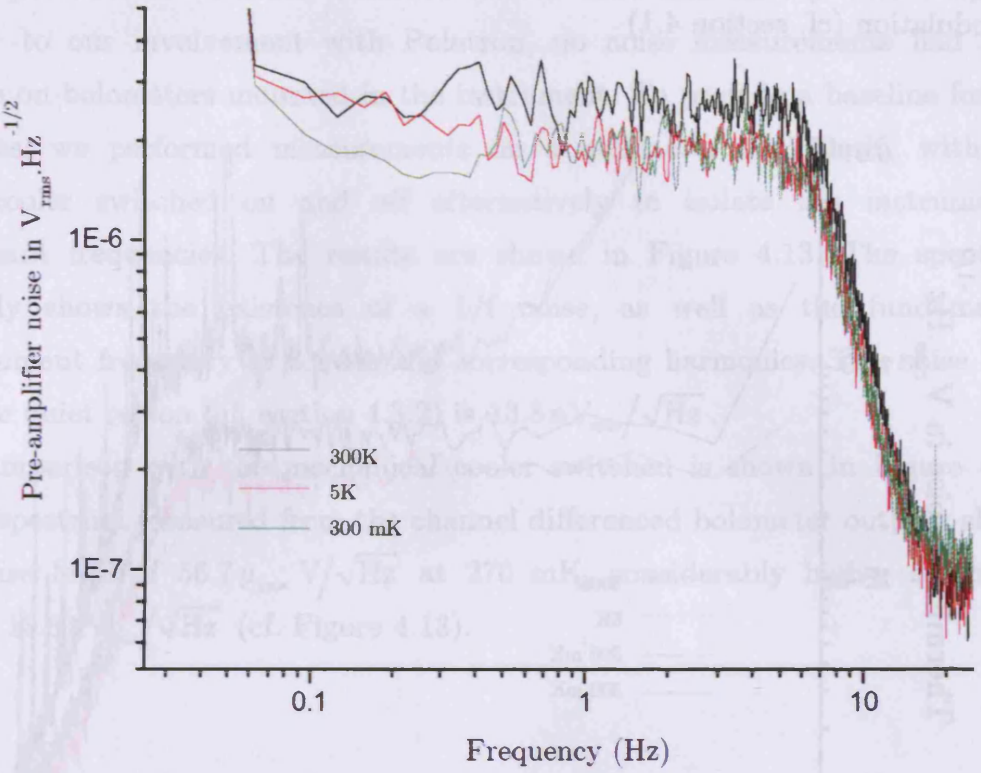

Figure 4.11: Pre-amplifier noise spectrum.
The measurement was performed on a channel with grounded inputs. The noise floor is 2.65. 1.92 $\mu V/\sqrt{Hz}$ and 2.00 $\mu V/\sqrt{Hz}$ at temperature of 300K, 5K, 300mK respectively (between 0.5 and 1.5 Hz). Note that the gain is 600.

From the noise spectra, the pre-amplifier noise equals $4.4\,nV_{rms}/\sqrt{Hz}$ at 300 K, and $3.3\,nV_{rms}/\sqrt{Hz}$ at 300 mK, in the same frequency range as for the resistor noise. This sets a lower limit on the noise from the devices we measure, since the contribution of the detector noise and the electronics would add in quadrature (cf. 2.2.2).

4.3.3 Thermistor noise

Shown in Figure 4.12 are the noise spectra measured by a spectrum analyzer from thermistors located in the bolometer bridge illustrated in Figure 4.4. The spectra reveal a significant 1/f noise due to drift in the base temperature, as explained above. This could influence the responsivity of the bolometers. Nevertheless, the results still show a 'clean' frequency range between 0.5Hz to 1.5 Hz. Therefore, we anticipated the waveplate to rotate at a rate of ~1.1Hz, at exactly half of the cryocooler fundamental frequency present at 2.2Hz. In

This provides an ultimate sensitive test of EMI and microphonic coupling. Prior to our involvement with Polatron, no noise measurements had been made on bolometers mounted in the instrument. To provide a baseline for our results, we performed measurements on a bolometer at 270mK, with the cryocooler switched on and off alternatively to isolate the instrumental resonant frequencies. The results are shown in Figure 4.13. The spectrum clearly shows the existence of a 1/f noise, as well as the fundamental instrument frequency at 3.2 Hz and corresponding harmonics. The noise floor in the quiet region (cf. section 4.3.2) is $13.8\,\mathrm{nV_{rms}}/\sqrt{\mathrm{Hz}}$.

A comparison with the mechanical cooler switched is shown in Figure 4.14. The spectrum measured from the channel differenced bolometer outputs shows a noise level of $56.7\,\mu_{\mathrm{rms}}\,\mathrm{V}/\sqrt{\mathrm{Hz}}$ at 270 mK, considerably higher compared with $13.8\,\mathrm{nV_{rms}}/\sqrt{\mathrm{Hz}}$ (cf. Figure 4.13).

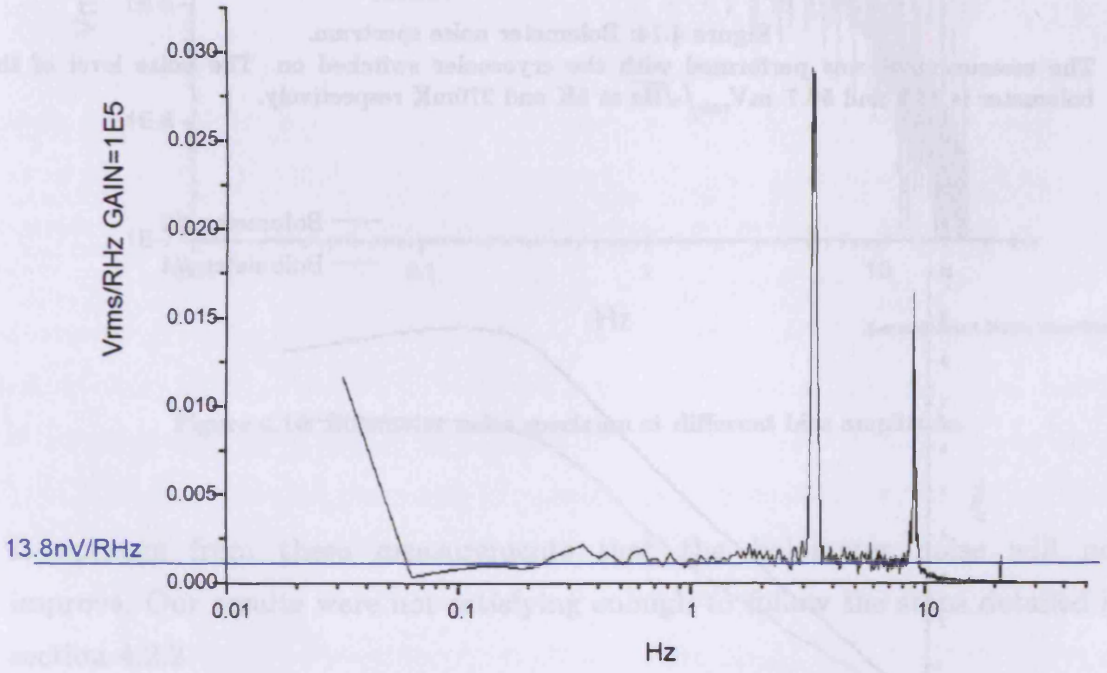

Figure 4.13: Bolometer noise spectrum.
The noise was measured with the cryocooler turned off. The noise floor level between 0.5Hz and 1.5 Hz is $13.8\,\mathrm{nV}/\sqrt{\mathrm{Hz}}$. The gain is 1E5. The bolometer is biased at 3.1V.

The next step in evaluating the bolometer performance was measuring load curves, an example of which is shown in Figure 4.15.

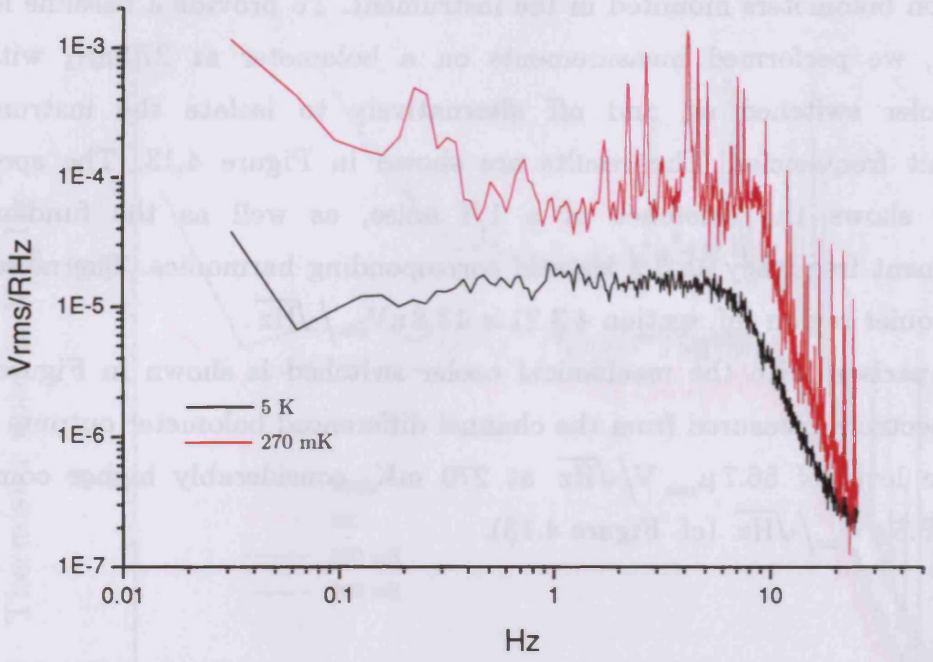

Figure 4.14: Bolometer noise spectrum.
The measurement was performed with the cryocooler switched on. The noise level of the bolometer is 16.8 and 56.7 $mV_{rms}/\sqrt{Hz}$ at 5K and 270mK respectively.

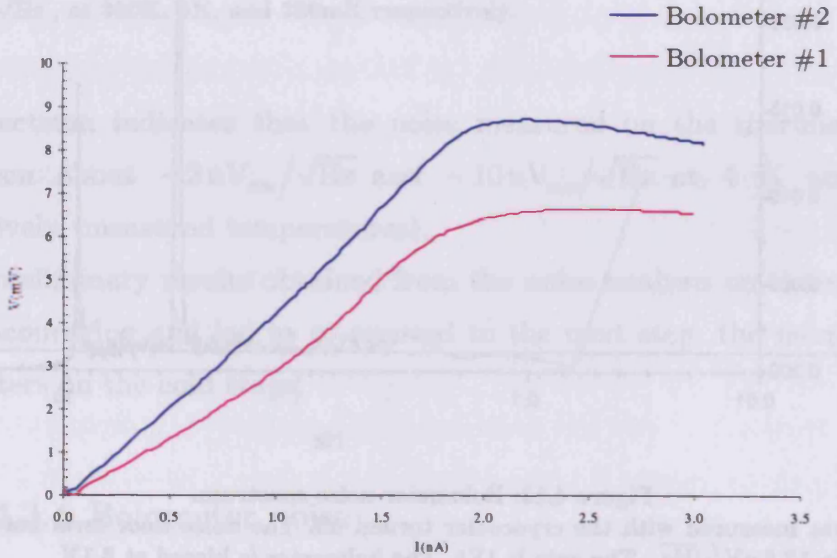

Figure 4.15: Load curves of both bolometers.
The measure was taken at a temperature of 270mK.

As a result of our noise measurements we decided to modulate both the bias voltage and frequency. Shown in Figure 4.16 are the spectra measured at 270 mK at different bias amplitudes. Those can be compared with the spectrum obtained at 5 Kelvin. As the bolometers are biased, the noise increases dramatically. A change in the bias frequency results in shifting the peaks, but do not decrease the noise level.

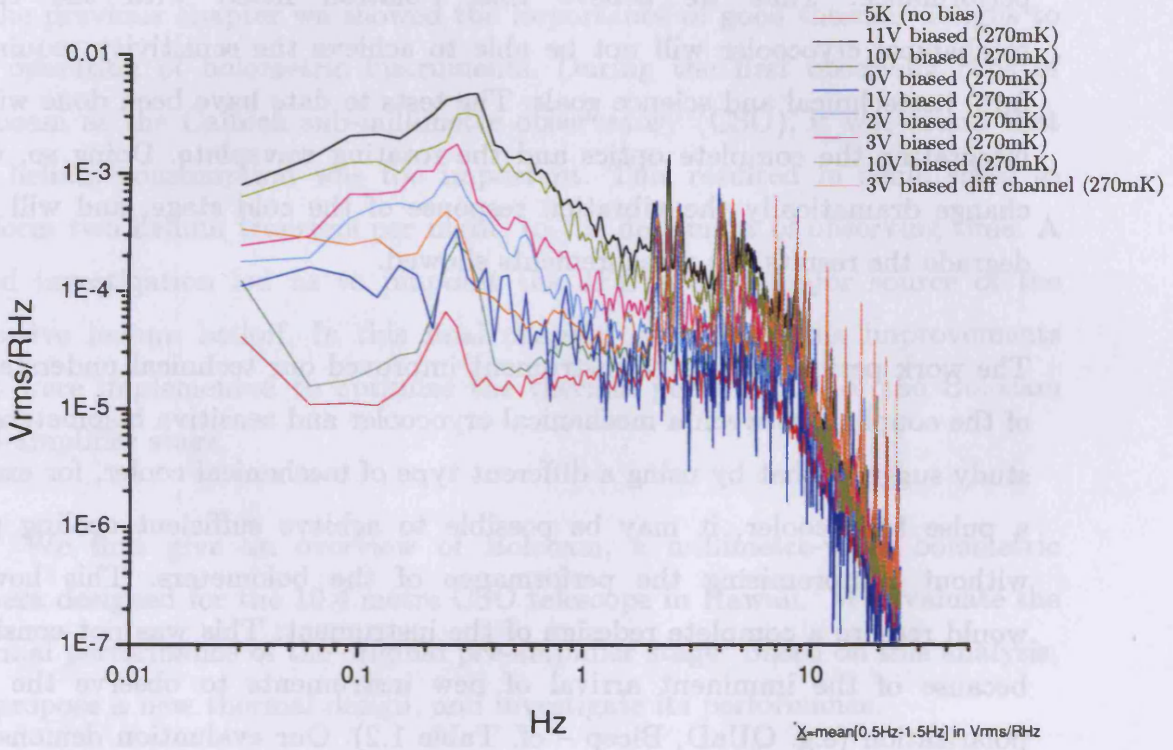

Figure 4.16: Bolometer noise spectrum at different bias amplitude.

It appears from these measurements that the bolometer noise will not improve. Our results were not satisfying enough to follow the steps detailed in section 4.2.2.

4.4 Conclusion

We collected sufficient data to assess whether Polatron would ever be able to detect the polarization of the CMB. Significant improvements have been made to the instrument, resulting in the first bolometer noise spectrum and load curves. The system has been improved to an extent that we believe that now only major conceptual differences can make improvements to the system performance. Thus we believe that Polatron fitted with the current mechanical cryocooler will not be able to achieve the sensitivity required to fulfil its technical and science goals. The tests to date have been done without integrating the complete optics and the rotating waveplate. Doing so, would change dramatically the vibration response of the cold stage, and will likely degrade the results our measurements showed.

The work performed on the instrument improved our technical understanding of the coupling between a mechanical cryocooler and sensitive bolometers. Our study suggests that by using a different type of mechanical cooler, for example a pulse tube cooler, it may be possible to achieve sufficient cooling power without compromising the performance of the bolometers. This however, would require a complete redesign of the instrument. This was not considered because of the imminent arrival of new instruments to observe the CMB polarization (e.g. QUaD, Bicep – cf. Table 1.2). Our evaluation demonstrates that in its current incarnation, the cryogenics of Polatron could only support the use of HEMT like detectors, which are less sensitive to microphonics and can be operated at higher temperature. In this case, the science goals would need to be changed, since HEMT are not as sensitive as bolometers at the wavelength Polatron was designed to observe.

Chapter 5 BOLOCAM JFET Thermal Design

In the previous chapter we showed the importance of good thermal designs to the operation of bolometric instruments. During the first observing runs of Bolocam at the Caltech sub-millimetre observatory (CSO), it was found that the helium consumption was too important. This resulted in some cases to perform two helium transfers per night, to the detriment of observing time. A rapid investigation led us to pinpoint the JFETs as a major source of the excessive helium boiloff. In this final chapter, we discuss the improvements that were implemented to optimize the thermal performance of the Bolocam cold-amplifier stage.

We first give an overview of Bolocam, a millimetre-wave bolometric camera designed for the 10.4 metre CSO telescope in Hawaii. We evaluate the thermal performance of the original pre-amplifier stage. Based on this analysis, we propose a new thermal design, and investigate its performance.

5.1 Instrument description

Bolocam is a bolometric camera composed of 144 Si_3N_4 diffraction-limited spider-web bolometers (Mauskopf, 1997), manufactured on a hexagonal wafer shown in Picture 5.1. Each bolometer sits in an integrating cavity, and is fed by a smooth-walled conical feedhorn defining the beam. The coupling between the integrating cavity plate and the feedhorns is achieved by single mode waveguides 2 λ long. The cavities, the feedhorns and the waveguides are respectively machined on three different plates, constituting the waveguide-cavity assembly. By changing the waveguide-cavity assembly, the focal plane array can be set up to allow measurements at three different spectral bands, centred at 1.1mm, 1.4mm and 2.1mm. Unlike SuZIE, these measurements are

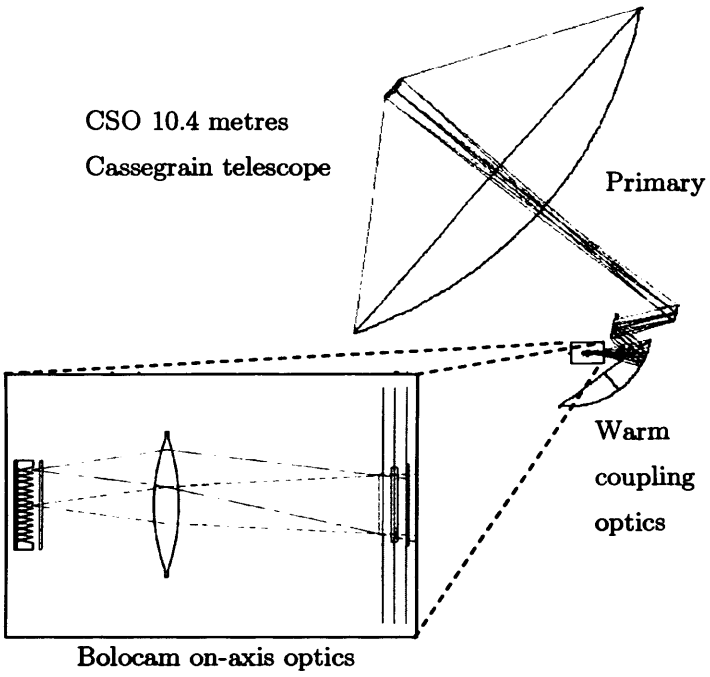

Figure 5.1: optical coupling of Bolocam and the CSO Cassegrain telescope

In the cryostat the incoming radiation is optically filtered to cut any out-of-band radiation before it hits the bolometers. This is achieved by three cold metal-mesh filters that define the high end of the band – i.e. low-pass filters, located at 77K, 4K and 300mK visible as illustrated in Figure 5.2. At 4K there is also an infrared filter, whereas the horns define the lower edge of the bandpass. The filter stack is provided by QMCI[1] in Cardiff University.

To reach the high sensitivity required for deep millimetre observations, the bolometric array is cooled down to ~255 mK using a triple stage ^{4}He-^{3}He-^{3}He sorption fridge specially designed for the instrument (Bhatia et al. 2000), described in section 2.3.2. Its principle of operation is similar to that used in Polatron (cf. section 4.2.3).

[1] Queen Mary College Instrument

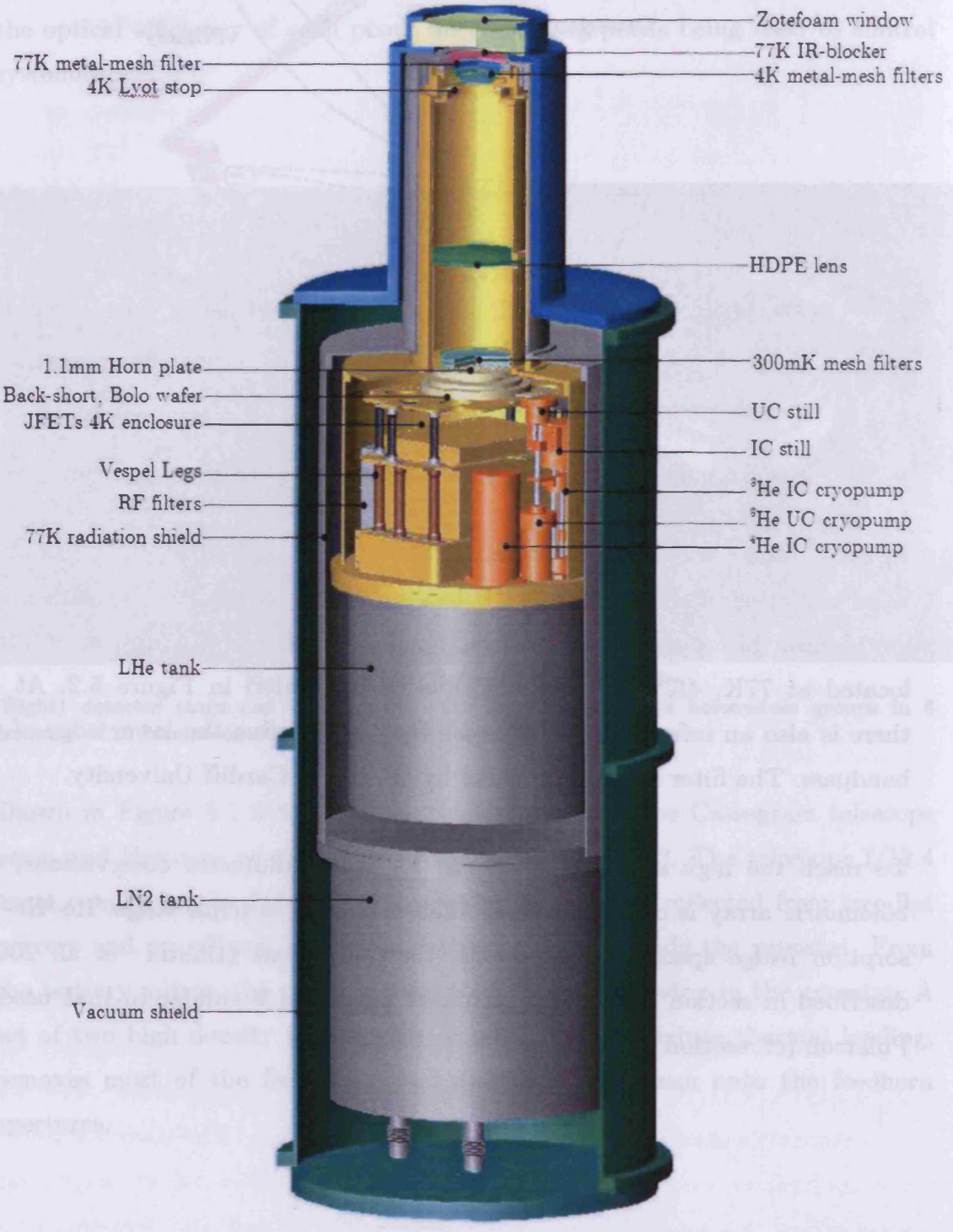

Figure 5.2: Bolocam on-axis optics and cryogenic layout.

Bolocam at the CSO can be operated in several different scanning modes, including drift scanning, raster scanning, and chopping. At 1.1mm in raster un-chopped scanning mode, the sensitivity per pixel has been calculated to be $100\,\mathrm{mJy}\sqrt{\mathrm{sec}}$ giving a mapping speed is of $13\,\mathrm{arcmin.hr^{-1}.mJy^{-2}}$. By chopping the secondary, these values are respectively $143\,\mathrm{mJy}\sqrt{\mathrm{sec}}$ and $6\,\mathrm{arcmin.hr^{-1}.mJy^{-2}}$. With its AC-biased readout electronics, Bolocam is capable of mapping at a speed[1] an order of magnitude higher than other instruments (e.g., SCUBA, SuZIE). The instrument spectral bands have been specifically chosen to:

- Distinguish between the decrement, null and an increment spectral signature of the Sunyaev-Zel'dovich effects towards galaxies clusters, and separate the SZ kinetic and thermal components.
- Study the thermal dust emission from nearby and high-redshifted galaxies, notably in the far infrared background[2] detected by COBE on fields currently observed by SCUBA[3], MAMBO[4] and IRAS (cf. Table 1.3).
- Perform blank-field observations at 2.1 mm that are adequate to study the power spectrum of the CMB secondary anisotropy around $\ell \sim 10{,}000$, where the thermal SZ effect is expected to dominate.

Up until 2003, Bolocam was operated at the CSO in engineering time. Very recently, it has become integrated as a facility instrument.

5.2 JFET amplifiers in Bolocam

By measuring the helium boiloff with and without JFETs, we were able to identify the dissipated power of the JFET modules (~250 mW) as the main cause of the excess helium consumption (~30 %). In this section we describe the role of JFETs, and their location in the instrument.

---

[1] given by $N_{pix}\Omega_{beam}/sensitivity^2$

[2] Dust from close to high-redshifted galaxies re-emit stardust photon in the FIR - locally, a third of stardust is believed to be re-emitted in the far-infrared, which then redshift into the sub-millimetre domain.

[3] Sub-millimeter Common User Bolometric Array

[4] MAx planck Millimeter BOlometric instrument

As normally encountered in low signal application, JFETs are used to couple the high bolometer impedance with the low impedance of the wires, acting as a buffer. Pairs of unity-gain JFETs are mounted in a differential source-follower configuration (cf. Figure 5.3). This in turns reduces considerably the susceptibility of electrical microphonics pickups, electro-magnetic interference and RC roll-off[1].

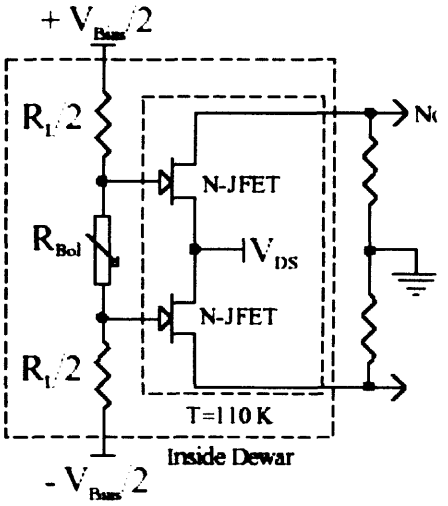

Figure 5.3: Differential JFET pair circuit.
It consists in a source-follower configuration with $R_L = 20M\Omega$.

In most bolometric systems, the JFETs are situated close to the detector stage in order to reduce microphonics pickups along long wires. From measurements, Bolocam JFETs best noise performances occur at a temperature of ~140K.

5.3 Original thermal model

5.3.1 Description

The high operating temperature of the JFETs and its proximity to the baseplate or the detectors, imply a careful thermal design of the baseplate assembly. Another difficulty arises from the differential JFET-pair assembly making up to 576 wires that need to be thermalized and secure. To the

[1] The resistance of the bolometer in parallel with the capacitance of the wiring make a circuit that can shunt some of the bias current. It can result in shifting the phase of the voltage across the bolometer, although its amplitude remains unchanged.

thermal design mechanical supports are also required. To implement the JFET stage, heat-sinks are available at four different temperatures: the nitrogen cold finger (cf. Figure 5.2), the 4K baseplate, and the triple-stage sorption fridge at ~360mK and ~260mK from the intermediate head and the ultra-cold head respectively. In Bolocam, it is obvious to divert the JFET operating temperature from the nitrogen cold finger.

In the original design, Bolocam JFET stage was suspended from the 4K baseplate by G10 walls (cf. Table 5.2) used due to its very low conductivity. A complex architecture was put together to optimize the mechanical and thermal support of the JFET-stage using the cold-finger as a cold source. This can be summarized as follows, based on the illustration given in Figure 5.4. The nitrogen rod provides a heatsink to attach the 77K plate, secured to the 4K baseplate by four G10 walls. From this platform, is suspended an aluminium frame using an additional set of four G10 walls. This frame supports the six JFET modules, and reaches their operational temperature by dissipating power. In this way, a mechanically rigid and almost thermally isolated path from 140K to 4K is achieved, the key to providing a temperature gradient and surfaces to which one can tightly secure the 576 signal wires.

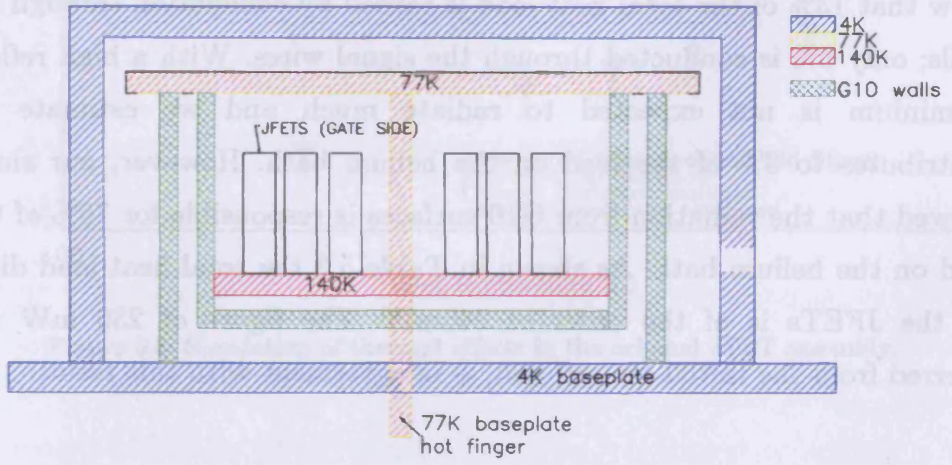

Figure 5.4: schematic of the original JFET stage design.

Table 5.1: Thermal conductivity from NIST - http://cryogenics.nist.gov/

Material	Thermal conductivity Nitrogen/Helium ($W.cm^{-1}$)
Copper	1620 / 690
Aluminium	730 / 220
Brass	170 / 60
Constantan	52 / 8.8
Stainless Steel	30 / 3.2
G10	1.5 / 0.17

Table 5.2: emissivity of used material from NIST - http://cryogenics.nist.gov/

Material	Typical emissivity
Matt black paint	0.5 to 0.8
Clean metal	0.01 to 0.15
Super-insulation	< 0.05

5.3.2 Thermal Analysis

In general, heat is exchanged mainly through radiation and conduction (cf. section 2.3.1) and their pathway needs to be minimized to reduce the helium boil-off. To assess the thermal model of the original design, we need a qualitative model of the heat transfer. Following the schematics of Figure 5.4 there are three main conductive paths and the three main radiative surfaces. Conduction occurs via the G10 walls from 77K to 4K and through the wires on both sides of the JFET modules from 140K down to 4K – each module contains 50 JFETs. In parallel, we identified the emissive G10 walls at 140K and 77K, and the aluminium walls at 77K as dominant radiative surfaces. Our analysis is summarized in Table 5.3, and plotted in Figure 5.5. Our results show that 13% of the total heat load is caused by conduction through the G10 walls; only 6% is conducted through the signal wires. With a high reflectivity, aluminium is not expected to radiate much and we estimate that it contributes to 3% of the load on the helium bath. However, our simulation showed that the radiation from G10 surfaces is responsible for 76% of the heat load on the helium bath. As shown in Table 5.3 the total heat load dissipated by the JFETs is of the order of 245mW. The figure of 230 mW that we inferred from the initial boil-off test, is in agreement with this result.

Table 5.3: Thermal model of the original design

Material	Heat transfer	Heat load in %	Heat load in mW
G10	Conduction	13%	32
Manganin (wires)	Conduction	06%	14
Aluminium	Radiation	03%	08
G10	Radiation	76%	191
TOTAL			245mW

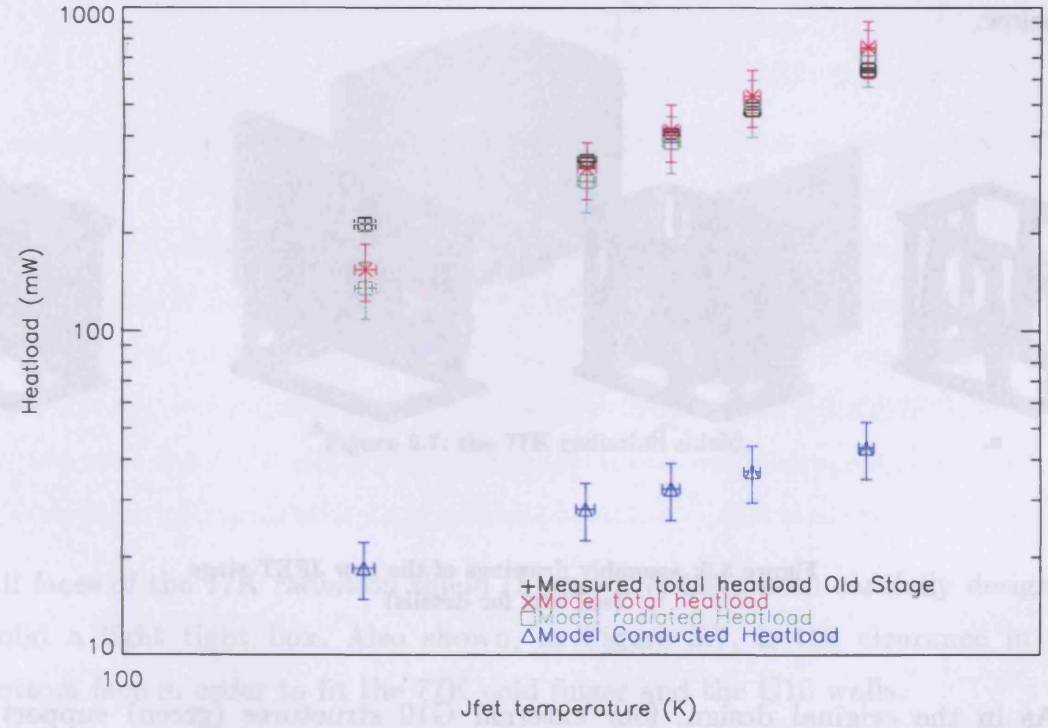

Figure 5.5: Simulation of thermal effects in the original JFET assembly.

5.4 New design

As a first step, we investigated Kevlar as an alternative to G10 walls. However, the absence of surfaces to thermalize and attach the wires led us to abandon this idea. Instead, we provided a mean to intercept the radiative heat before it reaches the 4K baseplate. This was achieved by housing the JFET stage in a 77K enclosure. The main constraint on the design is that of space. In height, the size of the entire enclosure is limited by the position of the focal plane; the width is limited by the presence of the triple-stage refrigerator and the RF filters as shown schematically in Figure 5.2. In addition to the size constraints, our design must include surfaces providing a thermal gradient to secure the wires to reduce microphonic pickup. Finally, the new design must be as simple as possible to assemble and disassemble.

The assembly is described below in few simple steps illustrated in Figure 5.6 below.

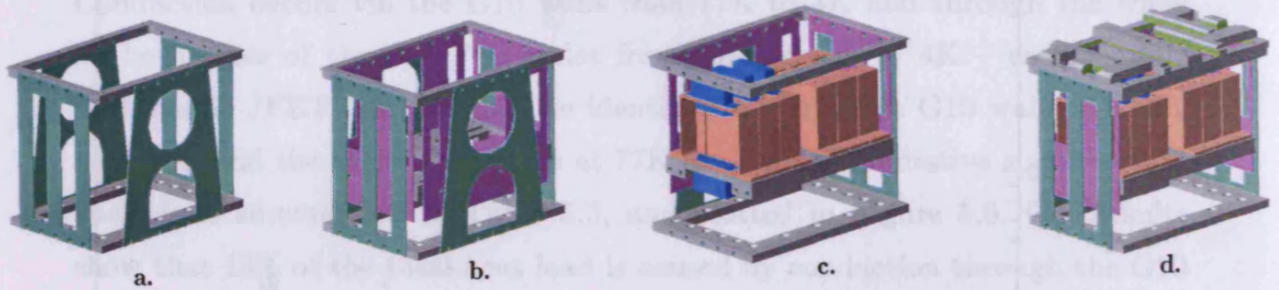

Figure 5.6: assembly drawings of the new JFET stage (see text for details)

As in the original design, four external G10 structures (green) support an aluminium frame in contact with the cold finger. This provides a 77K platform above the baseplate. The G10 walls provide both a thermal gradient and a surface to secure the wires. The shape of the walls has been drawn to minimize the conductivity, the radiative surface and to ensure a strong mechanical support. The four G10 walls (in purple) are suspended from the

frame sitting at 77 Kelvin. From the bottom of those is screwed a second aluminium frame to provide a solid base to the JFETs modules (in pink). By the self heating of the JFETs, this frame reaches a temperature of ~140 Kelvin under normal operation. A complex aluminium structure located on top of the 77K frame (Figure 5.6d) serves as a tight-down surface for the gate-side wires sticking up from the JFETs modules (as shown in Picture 5.2).

In order to prevent the radiated heat from evolving into the 4 Kelvin environment, the assembly (Figure 5.6d) is enclosed in a gold plated aluminium thermal shield (Figure 5.7) attached to surfaces at 77 Kelvin. The inside faces are painted with a mixture of Stycast and charcoal to absorb humidity and limit emission.

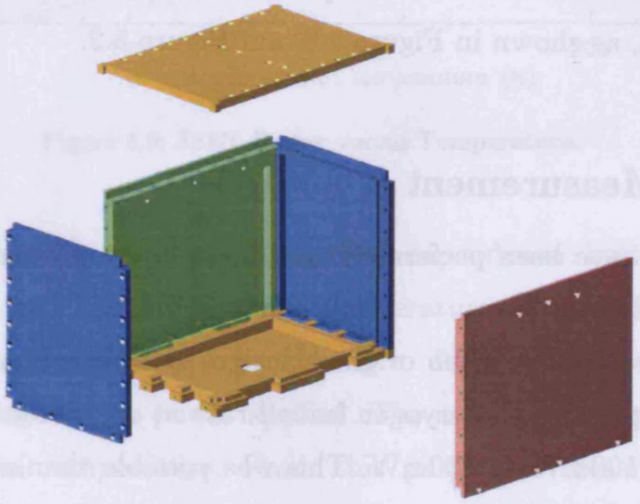

Figure 5.7: the 77K radiation shield.

All faces of the 77K radiation shield (Figure 5.7) have been carefully design to build a light tight box. Also shown, in Figure 5.7, is the clearance in the bottom face in order to fit the 77K cold finger and the G10 walls.

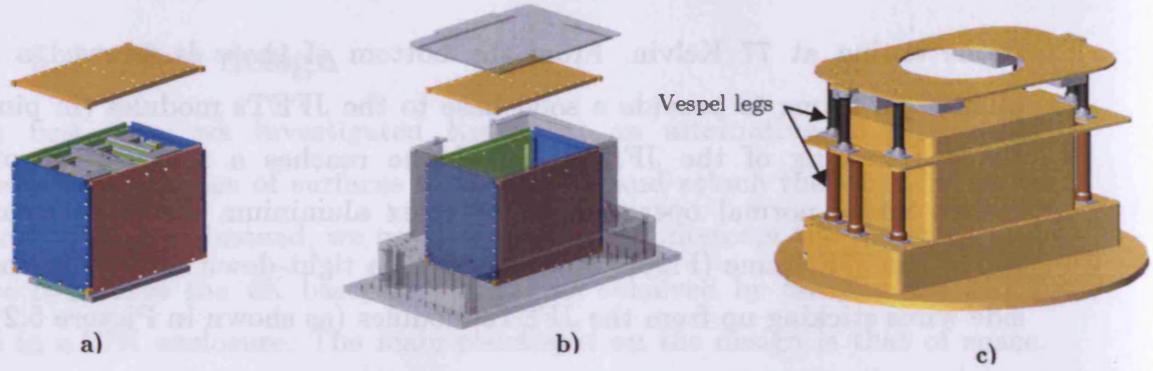

Figure 5.8: final assembly of the JFET sage onto the 4K baseplate.

A final radiative isolation is achieved with a 4K radiation shield that encloses the 77K radiation shield. The 4K enclosure is also painted in black as described above. Shown in Figure 5.8c is the final design assembled on the 4K baseplate. The 4K radiation shield provides supports to the Vespel legs of the detector stage, as shown in Figure 5.8 and Figure 5.2.

5.5 Measurement & analysis

Various tests have been performed to analyze in details the thermal behaviour of the assembly.

First of all, we analysed the original design by measuring the temperature of the JFET stage, and the cryogen boiloff-rate at a different dissipative power, ranging from 100mW to 800mW. This was possible thanks to a heater placed on the JFET stage to simulate their operating dissipated power.

Then, we performed the same measurements with the new design. The procedure was three-fold. We tested the new design described in section 5.4,

- with neither any signal wires nor JFET modules,
- without any wires, JFET modules or the 77K radiation shield,
- with the signal wires plugged in, and the JFETs modules operating.

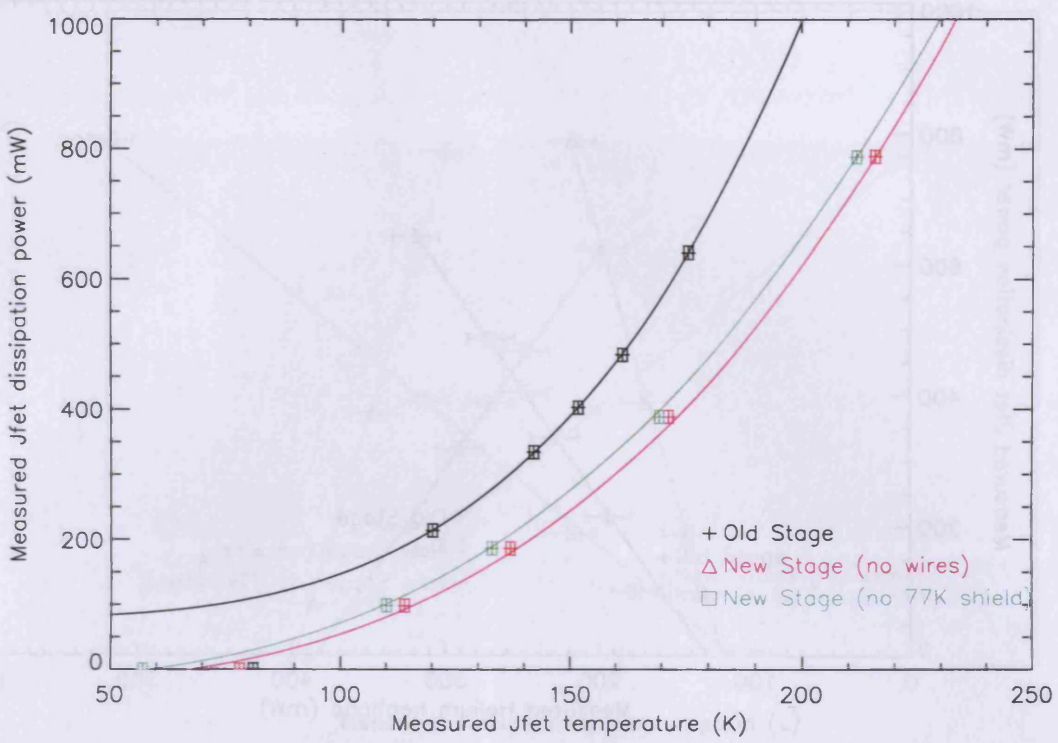

Figure 5.9: JFET Power versus Temperature.

The analysis consisted of determining the dependence between the JFET dissipated power and the JFET stage temperature as plotted in Figure 5.9. The JFET stage temperature in the two designs appeared to respond differently to change in the power applied. The new design requires less power to reach a certain temperature. From this particular measurement (Figure 5.9), we notice that the absence of the 77K radiation shield (green line) does not show a significant impact on the design. This is not surprising since the radiated energy would affect the colder surrounding parts.

For a better understanding of the role played by the 77K radiation shield, we investigate in Figure 5.10 the relationship between the dissipated power and heat-load calculated from the measured helium boil-off. For the same power applied on the JFET stage, the new design results in a smaller load, compared to the original design. The green curve shows the performance of the 77K intermediate radiation shield in intercepting the radiative heat before it hits the 4K parts. This shows without any doubt that the new design has had a beneficial impact on the thermal performance.

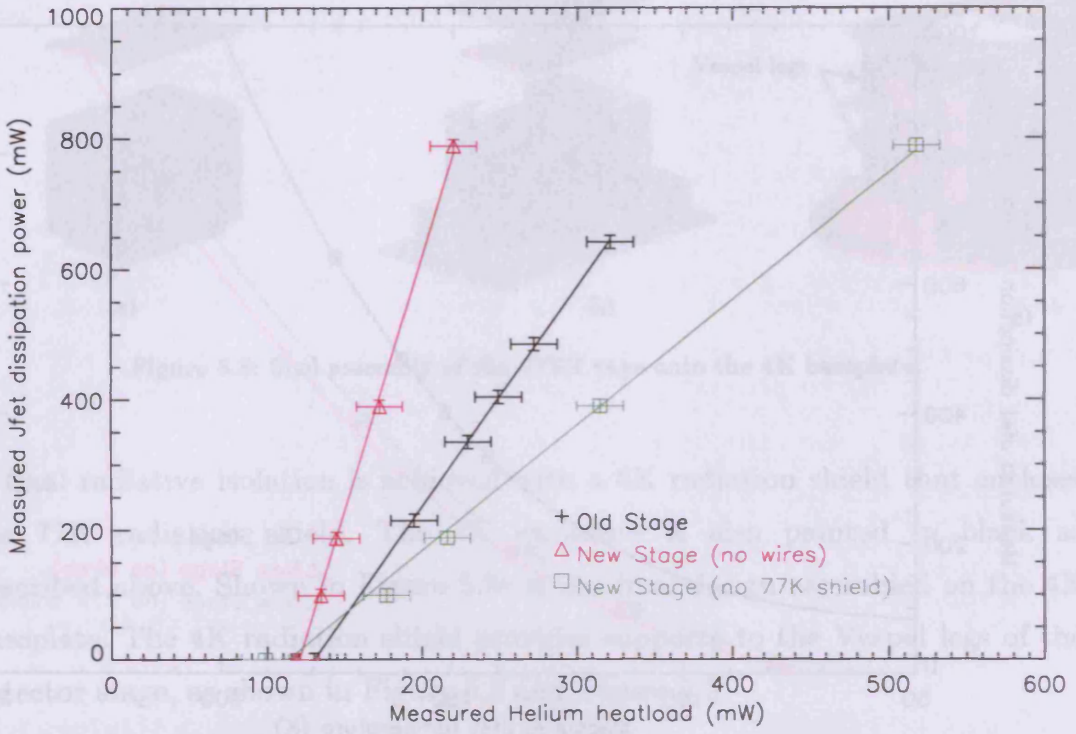

Figure 5.10: Helium heat load vs. JFET dissipated power.

To quantify the actual benefit of the new design, we measured the helium flow rate, characteristic of the boil-off. Acquired in STP [1], we calculated the consumption of liquid helium per day as a function of the power applied on the JFET stage. Function of the dissipated power and the measured temperature, the results are shown in Figure 5.11 and Figure 5.12. From the graph shown in Figure 5.11 we can conclude that the new JFET design results in half the liquid helium consumption than the original design. Figure 5.12 reinforces the initial need for re-designing the JFET stage.

This new design is shown in Picture 5.2.

[1] Standard Temperature and Pressure

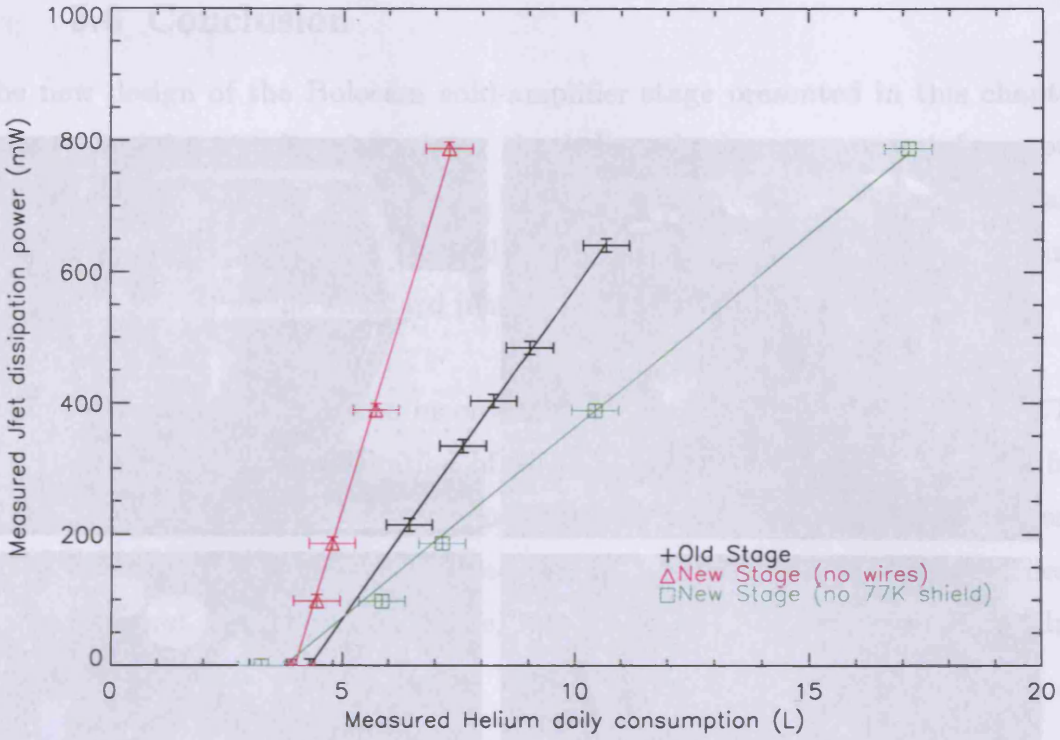

Figure 5.11: daily helium consumption vs. JFET power.

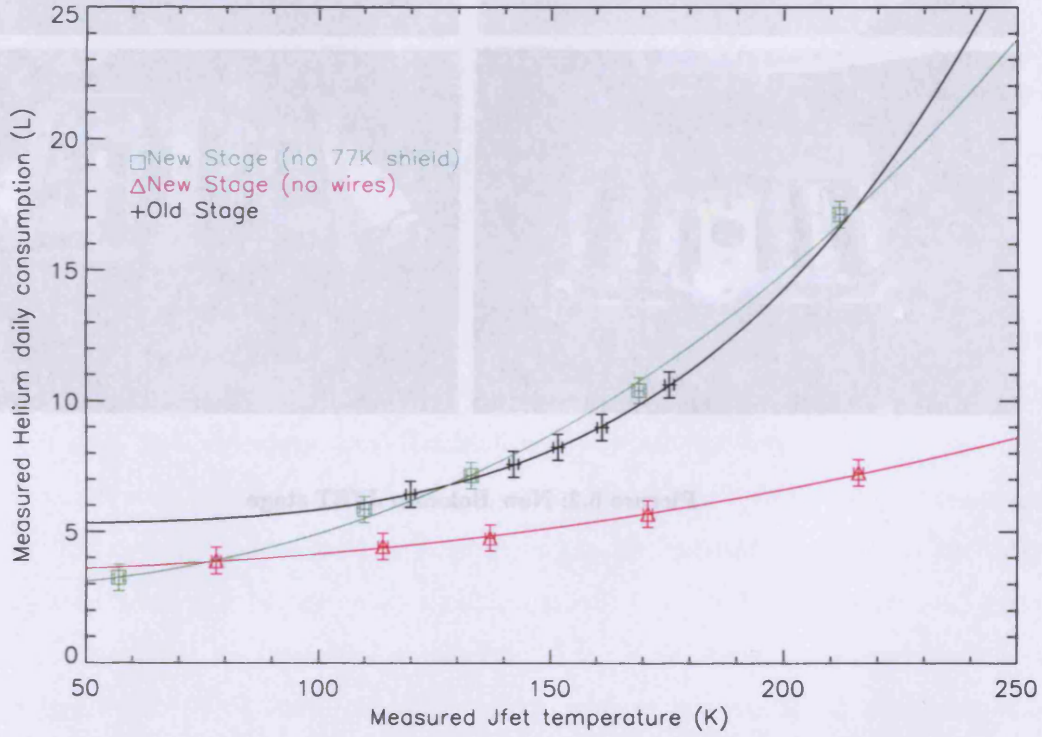

Figure 5.12: daily helium consumption vs. JFET temperature.

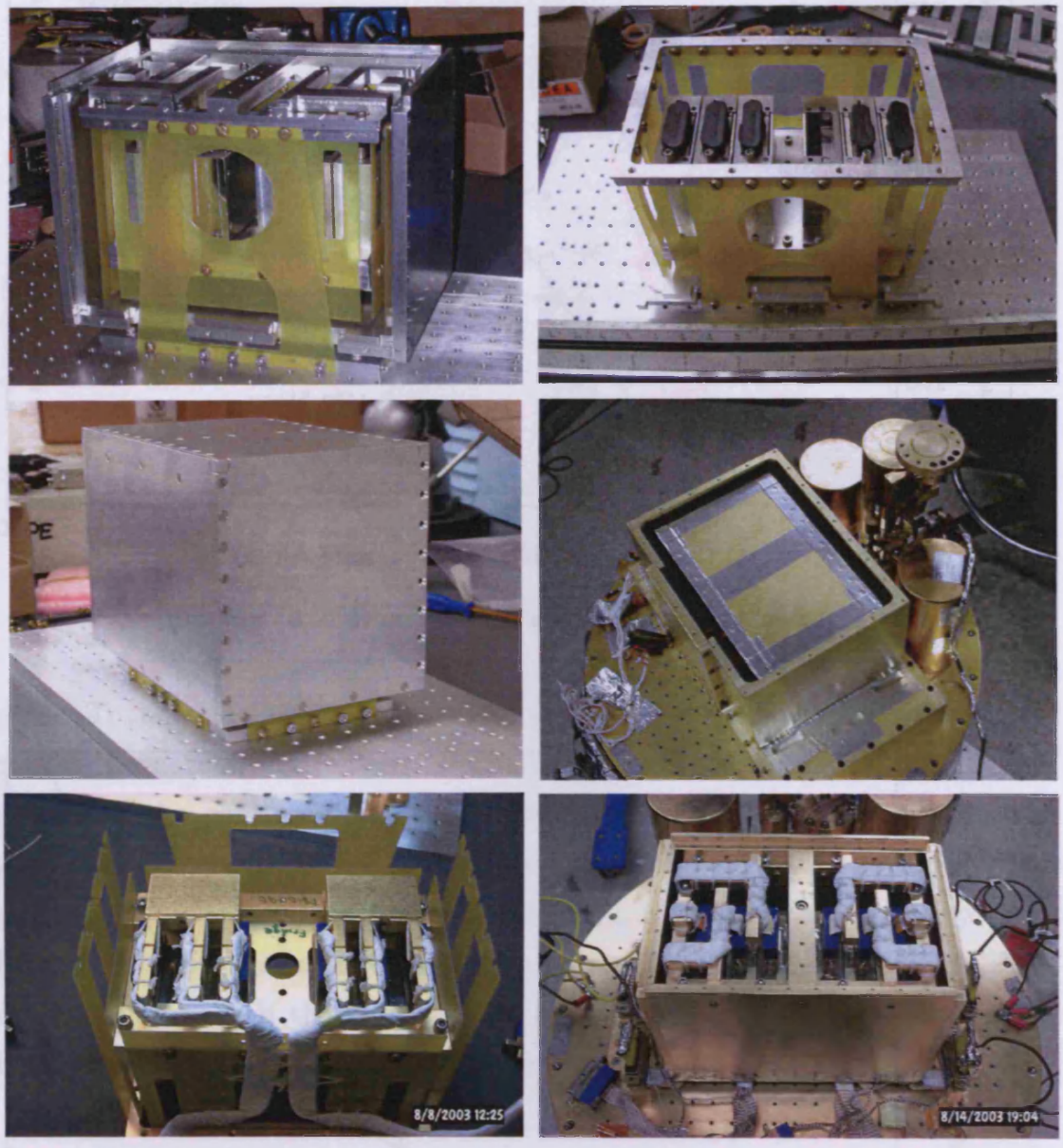

Picture 5.2: New Bolocam JFET stage

5.6 Conclusion

The new design of the Bolocam cold-amplifier stage presented in this chapter has resulted in a reduced load on the helium bath, as expected from our simulation. The reduction in boil-off has been measured to be 4 litres per day, a factor two lower than the original assembly. The improved JFET housing has been adopted as the standard instrument configuration.

In the near future, the inconvenience of operating this type of JFETs can be avoided. A new generation of JFETs modules has been engineered for SPIRE (Griffin et al. 2000). They present the advantage of dissipating very little power and therefore can be placed directly on the 4K baseplate. These devices are not to be discussed here, but we stress that development in this area exists.

Appendix

A. Gaussian Optics

At millimetre wavelengths traditional geometrical optics is not appropriate to analyse the propagation of an electromagnetic wave. The relatively small dimensions of the optics when measured in wavelengths result in an important diffraction effect that must be taken into account. At these wavelengths, quasi-optical approach (also called Gaussian optics) must be used to study the beam propagation. An exhaustive study can be found in Goldsmith (Goldsmith 1998), on which the following overview is based.

The propagation of a Gaussian beam is analysed in cylindrical coordinates in terms of its beam radius, wavelength, confocale distance, and its wavefront characteristics (radius of curvature, phase difference). The intensity distribution and power density of the incoming radiation have a Gaussian form given by:

$$E(r,z) = \left(\frac{2}{\pi\omega^2(z)}\right)^{0.5} .e^{\left(\frac{r^2}{\omega^2(z)} - jkz - \frac{j\pi r^2}{\lambda.R(z)} + j\phi_0(z)\right)} \qquad (A.1)$$

where R is the radius of curvature of the beam, ϕ the phase delay with respect to a plane wave, ω the beam waist radius, and r the distance from the axis of propagation z, as illustrated in Figure A.1 and Figure A.2 below.

The analysis if simplified when the beam is considered at its beam waist, radius at which the field falls to 1/e points relative to its on-axis value. The beam waist characterises the fundamental Gaussian beam where the field distribution and power density are maximum and the wavefront is planar (no phase difference, radius of curvature tends to infinity). As the radiation propagates from the beam waist location (z=0) the field amplitude and power density decrease as shown in Figure A.2. The beam radius, radius of curvature, and the phase expand slowly within the confocal distance (also called the Rayleigh range), then linearly in the far field.

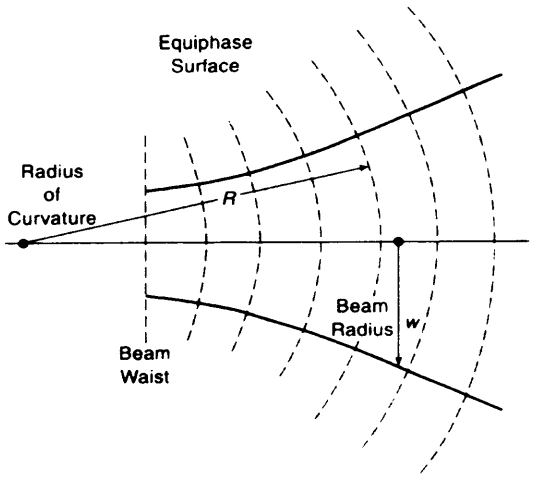

Figure A.1: Spherical wavefront relative to a plane wave (Goldsmith 1998).
The schematic represents a cut through the beam, showing equi-phase surfaces, beam radius, and radius of curvature.

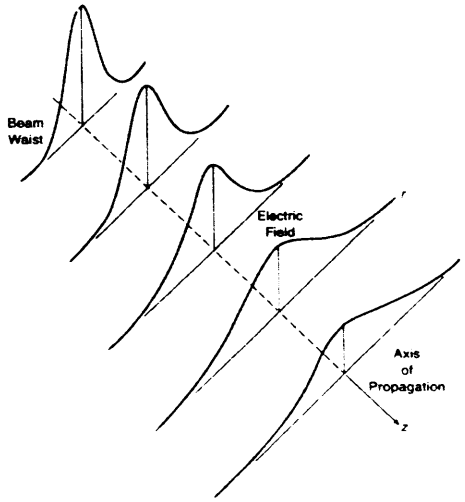

Figure A.2: Propagation of a Gaussian beam (Goldsmith 1998).
It shows the increase in the beam radius and decrease of the peak amplitude as the distance from the waist increase.

The confocal distance, function of the wavelength λ and the beam waist ω_0, is given by:

$$Z_c = \frac{\pi\omega^2}{\lambda} \tag{A.2}$$

When the propagating beam encounters an optical surface (lenses, mirrors...) it is important to consider how the beam couples to the aperture. One often

refers to as the edge taper which is the intercepted relative power density. The edge taper can be expressed in dB by:

$$T_e(\mathrm{dB}) = -10\log\left(\frac{-2r_s^2}{\omega^2}\right) \tag{A.2}$$

In practice, it is usual to truncate the beam well below the on-axis value in order to decrease the effect of diffraction by the truncation. Usually a truncation of a beam by a surface one-and-half time or twice the beam diameter (respectively -18 dB and -34.7 dB) is sufficient enough. Such an edge taper truncates the Gaussian beam in the region where the power density is very small (see Figure A.4).

Consequently, it is convenient to oversize the optical elements (lenses, mirrors) in order to truncate the incoming beam in such a way that the most power collection is achieved (referred to as the aperture efficiency). For example, the illumination of a surface four times larger than the beam radius ideally covers 99.97% of the normalised power distribution of the radiation; a surface three times larger than the beam radius intercepts 98.6% of the collected power.

In analysing an on-axis Cassegrain antenna, the blockage of the incoming radiation by the secondary mirror must be taken into account. The situation is described below:

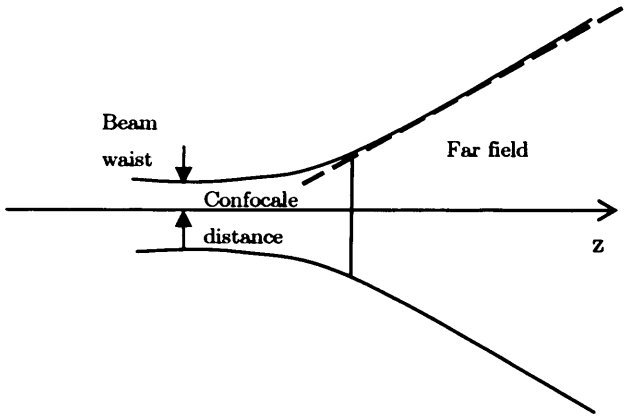

Figure A.3: Quasi-optical beam. Expansion as a function of the distance z from the beam waist.

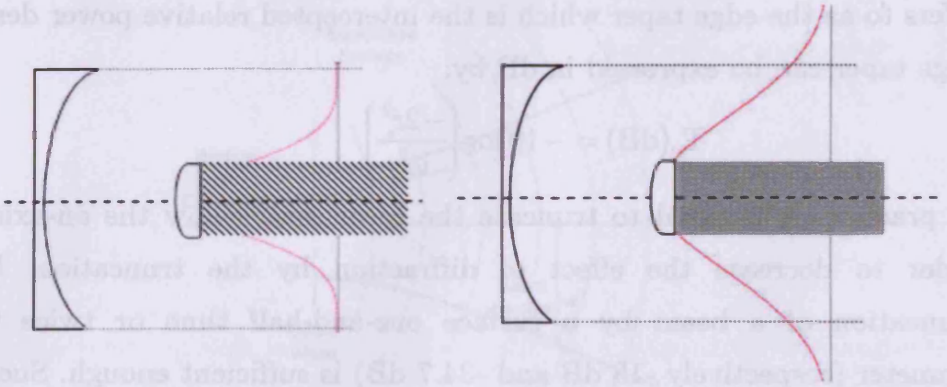

Figure A.4: Aperture illumination of an on-axis Cassegrain telescope. (left) Strong edge taper, poor efficiency. The secondary mirror blocks the Gaussian beam at its higher density of power. The primary mirror integrates the power only at the edge of the beam. (Right) Weak edge taper, high efficiency. The main part of the beam at its higher power density is not stopped by the secondary. The aperture efficiency at the primary is therefore much better. Nevertheless the extremes of the beam are truncated, which results in a weak edge taper. This situation is preferred to the previous one.

We summarize here the basic formulae of Gaussian beam propagation:

- the confocal distance that limits the far and near fields:

$$Z_c = \frac{\pi\omega^2}{\lambda} \tag{A.3}$$

- The beam radius expansion after propagating a distance z from the waist:

$$\Omega = \omega\sqrt{1+\left(\frac{Z}{Z_c}\right)^2} \tag{A.4}$$

- The beam waist size transformation through a lens:

$$\omega_0^{OUT} = \frac{\omega_0^{IN}}{\sqrt{\left(D_{IN}/f - 1\right)^2 + \left(\frac{Z_c}{f}\right)^2}} \tag{A.5}$$

- The beam waist location transformed through a lens:

$$D_{OUT} = f + \frac{D_{IN} - f}{\left(\frac{D_{IN}}{f} - 1\right)^2 + \left(\frac{Z_c}{f}\right)^2} \tag{A.6}$$

- The edge taper in dB:

$$T_e = 8.686\alpha \tag{A.7}$$

B. Violation of the Golden Rule

The result obtained in Figure 3.11 is derived from a simple geometrical analysis of the optics. Shown in Figure B.1 are the beam trajectories within the beam-combiner. The cold on-axis Cassegrain is simplified to a concave lens, and P represent the unfolded path of the incoming beam from the afocal warm Cassegrain telescopes, and f represent the equivalent focal length of the beam combiner (i.e. the lens in this case). In the figure below, we denote the point N as being the off-axis beam. We work out a relationship between its position to the on-axis reference (point F) as a function of the baseline and the pointing angle γ.

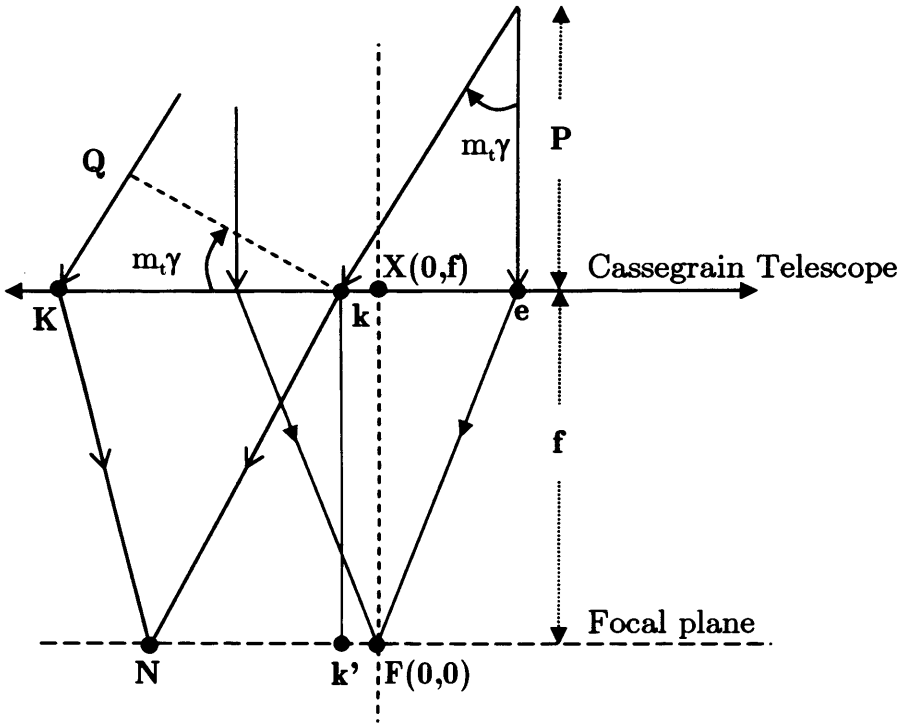

Figure B.1: Geometrical path in the cold beam-combiner. The cold on-axis Cassegrain is represented by a concave lens.

From the sizes of the cold flat mirror F_{TL} (transversal length) and cold primary mirror D_P we can work out $|Kk| = D_P - F_{TL} = 301$ mm , from which follows $|QK| = |Kk| m_t\gamma$. The spatial delay (cf. section 2.1.1) is proportional to the baseline $\tau_g = \gamma B$ (using small angles approximation). The distance between X and K is function of both the baseline and the pointing angle. We write:

$$|XK|(\gamma, B) = -\frac{|Kk|}{2} - P(B).\tan(m_t\gamma) \qquad (B.1)$$

where P(B) is the unfolded path to the focal plane of a ray entering the system. Thus, the distance between N and F can be worked out from simple trigonometry in the triangle (kNk') leading to:

$$|NF|(\gamma, B) = \frac{-a(\gamma, B) - \sqrt{\Delta(\gamma, B)}}{2a(\gamma)} \tag{B.2}$$

with:

$$a(\gamma) = 1 - \left(\frac{|Kk|}{|QK|(\gamma)} \right) \tag{B.3}$$

and:

$$\Delta(\gamma, B) = b^2(\gamma, B) - 4.a(\gamma)c(\gamma, B) \tag{B.4}$$

where the coefficients a and b are given by:

$$b(\gamma, B) = -2|SK|(\gamma, B) - |Kk| \tag{B.5}$$

$$c(\gamma, B) = XK^2(\gamma, B) + f^2 - {|QK|^2(\gamma)}/{4} \tag{B.6}$$

C. Electronics for temperature control

We describe in this section the electronics based on R. Tucker's design, for controlling temperatures of MBI-P. The discussion is two fold: the diode circuit (sensitive to temperature ranging from room temperature to ~3K) and the GRT electronic circuit (sensitive to temperature comprised between ~3K and ~200mK).

- Diode circuit:

A LM334 current source from National Semiconductor [7] is used to generate a 10μA constant current through the diode.

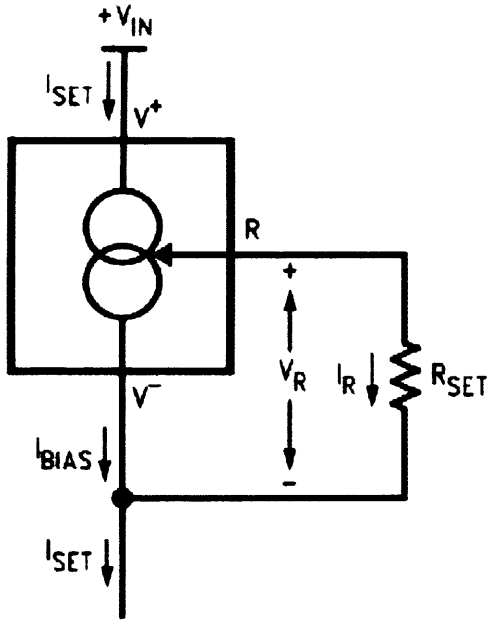

Figure C.1: Diode current generator.
The current flowing through the LM334 (I_{SET}) is the sum of the current flowing through R_{set} (I_R) and I_{BIAS}. RSET is set to 6.8k which produces a 10μA output current.

- GRT

The Germanium Resistance Thermometer is composed of a doped Germanium chip mounted strain-free on a gold plated copper can. This can is hermetically sealed and encloses helium gas used as a contact between the chip and the can. At temperatures below 4K, the helium liquefies. As a result, the best thermal contact with the outside environment is achieved through the wires. The GRT is embedded in an OFHC post. Shown in is the detailed electronic circuit. Figure C.2 and Figure C.3 illustrate the circuit and an explanation is provided afterwards.

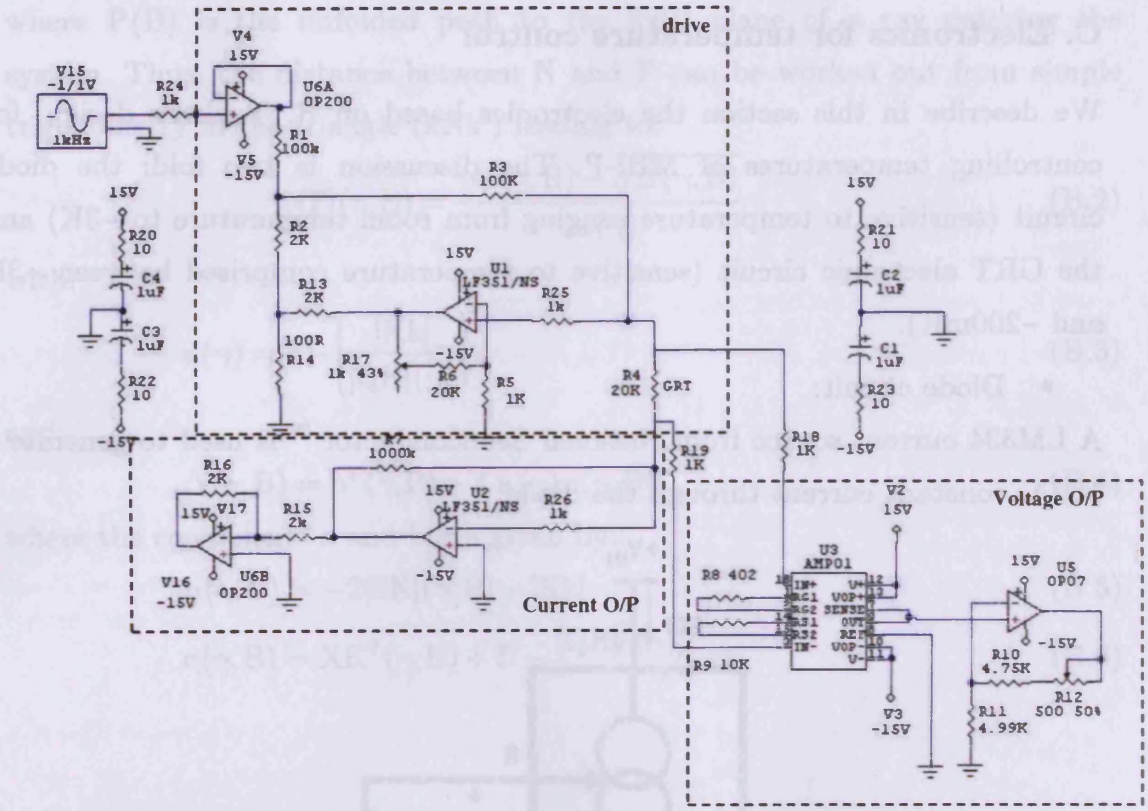

Figure C.2: GRT readout electronics (see text for details)

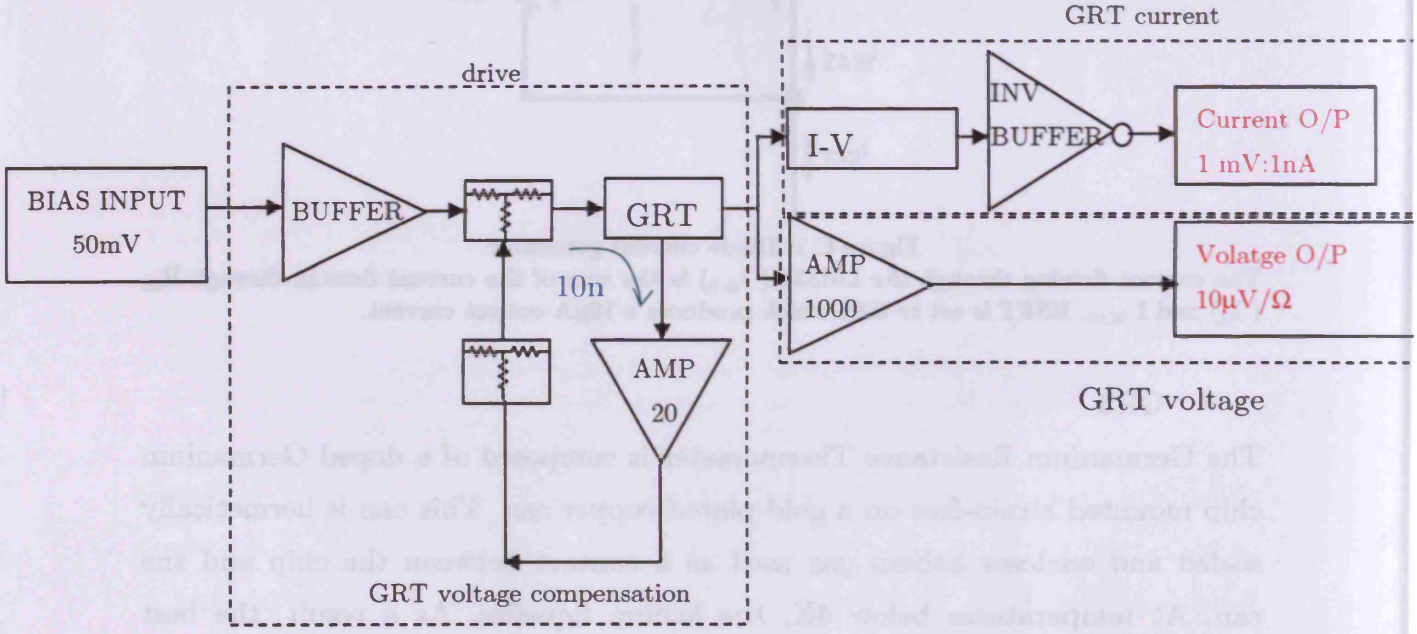

Figure C.3: Layout of the GRT readout circuit.

Circuit Description:

- BIAS Input:

The excitation current is brought from the Lock-in oscillating output set at 50mV rms and 300 Hz. One keeps in mind to avoid the odd harmonics of the 50 Hz main supply.

- Unity gain buffer (Voltage follower):

This common circuit is used to isolate the whole circuit from the source. Since the impedance of the operational amplifier is very high, it gives a good isolation of the output from the source.

- Feedback loop:

This loop is used to keep constant the current flowing through the GRT. Indeed, since the resistance of the GRT is expecting to vary, the depending current is subject to fluctuations. Therefore, the tuneable non-inverting OP-AMP circuit compensates for the voltage by acquiring the offset as the GRT resistor is increased.

A bias input of 50mV drives 10nA.

- I-V converter:

A usual OP-AMP circuit is used to convert the current flowing through the GRT into a voltage, giving a convenient reading possibility.

The achieved ratio is 1mV corresponding to 1 an.

- Inverting buffer:

Since the output of the I-V converter is negative, an inverting buffer is used to give a sensible positive output.

- AMP*1000:

Firstly, an instrumentation amplifier is used at a high gain of 500 to amplify the GRT voltage. Then, an OP-AMP amplified this last voltage by a factor of 2, giving a total amplification of 1000.

The voltage O/P is proportional to the GRT resistance as 10μV/Ω for a $500mV_{rms}$ input.

D. Technical drawing of the beam combiner

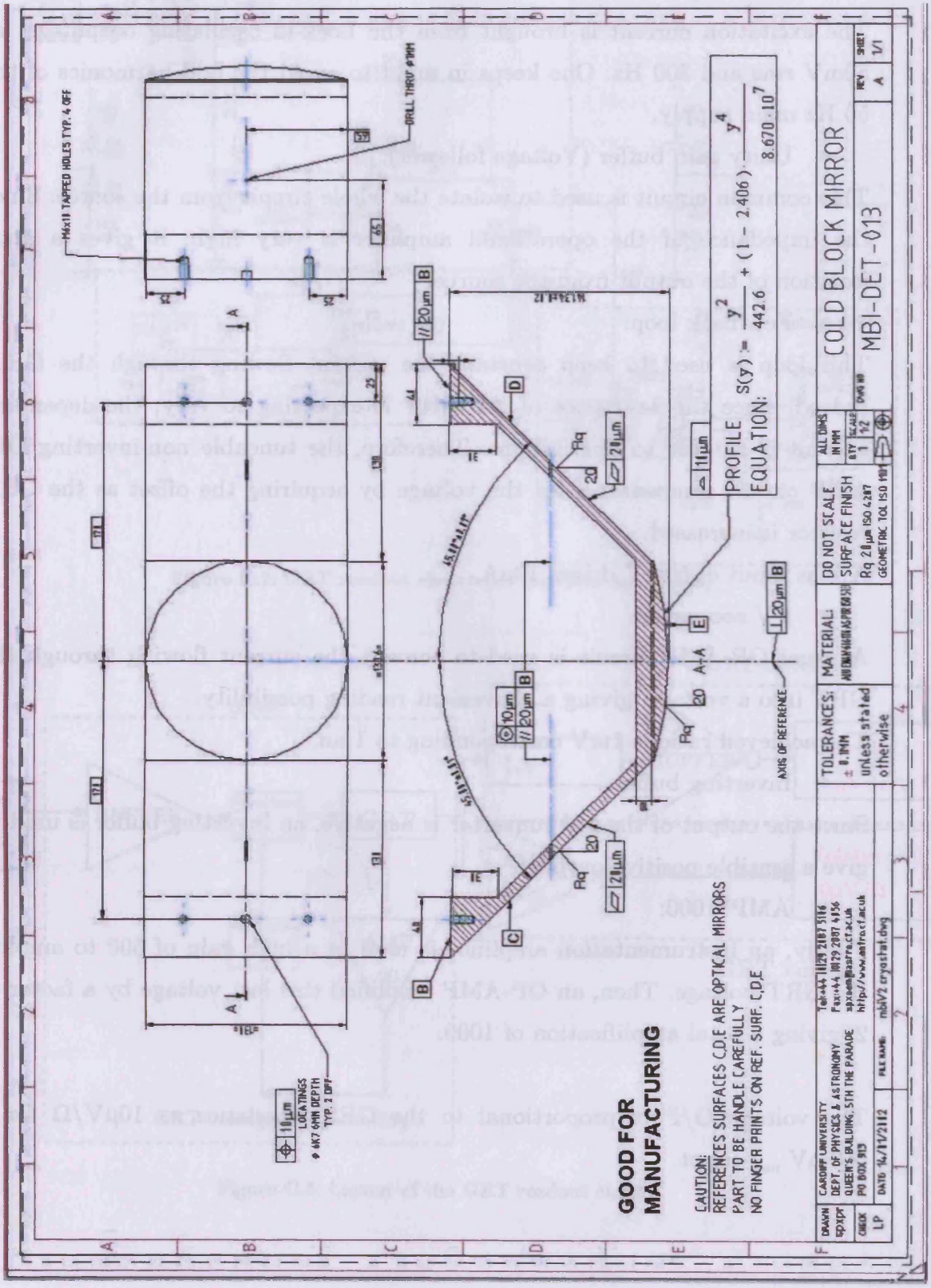

References

Armstrong, J.W., Srameck, R.A., Radio sci., 17.1579, **(1982)**

Bennett, C.L., et al., 'Preliminary separation of galactic and cosmic microwave emission for the COBE DMR', Astrophys. J., 396:7B, **(1992)**

Bennett, C.L., et al., **'**First year Wilkinson microwave anisotropy probe (WMAP) observations: preliminary maps and basic results**'**, Astrophys. J. Suppl., 148:1, **(2003)**

Bhatia, R.S., 'The effects of closed cycle coolers on infrared detectors for space missions', PhD thesis, University of London **(1998)**

Bhatia R.S., et al. *'The susceptibility of incoherent detector systems to cryocooler microphonics'*, Elsevier Cryogenics, 39: (8) 701-715, **(1999)**

Bhatia, R.S., et al., "A Three-Stage Helium Sorption Refrigerator for Cooling of Infrared Detectors to 280 mK", Cryogenics, Vol. 40, pp. 685-691 **(2000)**.

Bhatia, R.S., et al., ' Closed-cycle cooling of infrared detectors for Polatron', proceedings of the 11th international Cryocooler Conference, USA CA, Ed R.G. Ross, Jr. Plenum Press, NY, 577-586 **(2001)**

Birkinshaw, M., 'The Sunyaev-Zel'dovich effect', Phys. Rept. 310:97-195, **(1999)**

Bowden, M., et al., 'Scientific optimization of a ground-based CMB polarization experiment', MNRAS.349..321B, **(2004)**

Brandt, W.N., et al., 'Separation of foreground radiation from CMB anisotropy using multi-frequency measurements', Astrophys. J.,424:1-21, **(1994)**

Carilli, C. L., Lay, O. and Sutton, E. C., ALMA Memo, 21, **(1998)**

Carlstrom, J.E., et al., 'The CSO-JCMT Submillimeter Interferometer', ASP Conference Series, Vol. 59:35c, **(1994)**

Carlstrom, J.E., et al., 'Cosmology with the Sunyaev-Zel'dovich Effect', Annual Reviews of Astronomy & Astrophysics, Vol. 40, p. 643-680, **(2002)**

Chattopadhyay, G., Philhour, B., Carlstrom, J.E., Church, S., Lange, A.E., Zmuidzinas, J., ' A 96Ghz ortho-mode transducer for Polatron', IEEE microwave and guided wave letters, vol.8, No.12, **(1998)**.

Church, S.E., 'Predicting residual levels of atmospheric sky noise in ground-based observations of the CBR', MNRAS, 272..551C, **(1995)**

Church, S., et al., 'Quest on DASI: a south pole CMB polarization experiment', NewAR, 47.1083C, **(2003)**

Coulman, C.E., Radio Astronomical Seeing, eds. J. Baldwin and S. Wang, p. 11, **(1990)**

Fixsen, D.J., et al., 'The CMB spectrum from the full COBE-FIRAS data set', Astrophys. J., 473:576-587 **(1996)**

Gawiser, E., Silk, J., 'The CMB radiation', Phys. Rept., 333:245-267, **(2000)**

Gawiser, E., Smoot, G., 'Contribution of extragalactic Infrared sources to CMB foregrounds anisotropy', Astrophys. J., 480:L1-L4, **(1997)**

Glenn, J., PhD thesis, University of Arizona, **(1997)**

Goldsmith, P.F., 'Quasi-optical Systems – Propagation and Applications', IEEE press, **(1998)**

Gom, B.G. and Naylor, D.A., 'Modelled V-I Performance of a ^{3}He Composite Bolometer Detector', Int. J. of Inf. and Mm. Waves 20, No. 7, 1225-1238 **(1999)**

Griffin, M.J, Holland, W.S., 'the influence of background power on the performance of an ideal bolometer', Int. J. Infrared Mill. Waves, 9, 861, **(1988)**

Griffin, M.J., Swinyard, B.M., Vigroux, L., 'The SPIRE Instrument for Herschel', Proc. Symp. The promise of the Herschel Space Observatory, 37-44, **(2000)**

Harrison, D.L., et al., 'A measurement at the first acoustic peak of the CMB with the 33GHz interferometer', MNRAS, 316L:24H , **(2000)**

Hecht, E., 'Optics', fourth edition, ed. Wesley-Longman, ISBN-0805385665, **(2002)**

Hedman, M. M., et al., 'A Limit on the Polarized Anisotropy of the Cosmic Microwave Background at Subdegree Angular Scales', Astrophys. J., 548:L111, **(2001)**

Hobson M.P., Lasenby A.N., Jones, M., 'A Bayesian method for analysing interferometer observations of CMB fluctuations', MNRAS, 275:863H, **(1994)**

Holdaway, M.A., MMA Memo. No. 84, **(1992)**

Holdaway, M.A. and Owen, F.N., MMA Memo. No. 126, **(1995)**

Hu, 'Dark synergy: gravitational Lensing and the CMB', Phys.Rev. D65:023003, **(2002)**

Hu, W., White, M., 'The damping tail of cosmic microwave background anisotropies', Astrophys. J., 479:568, **(1997a)**

Hu, W., White, M., 'A CMB Polarization Primer', New Astronomy 2, 323, **(1997b)**

Hu, W., Sugiyama, N., and Silk, J. 'The Physics of Microwave Background Anisotropies', Nature 386, 37, **(1997)**.

Jones, R Clark, J. Opt. Soc. Am. 43, 1, **(1953)**

Jones, W.C., et al., 'A bolometric polarization sensitive bolometric detector for observation of the CMB', SPIE, 4855:227J, **(2003)**

Kamionkowski, M., Kosowsky, A., Stebbins, A., 'Statistics of cosmic microwave background polarization', Phys. Rev. D, 55-12, 7388 **(1997)**

Keating, B.G., et al., 'limit on the large angular scale polarization of the CMB', Astrophys. J., 560L:1K, **(2001)**

Keating, B.G., et al., 'BICEP: A large Angular Scale CMB Polarimeter', SPIE.4842..284K, **(2003)**

Knox, L., 'Determination of Inflationary Observables by Cosmic Microwave Background Anisotropy Experiments', Phys.Rev. D., 52:4307-4318, **(1995)**

Kogut, A., et al., First-Year WMAP Observations: Temperature-Polarization Correlation', Astrophys. J. Suppl., 148..161K, **(2003)**

Kosowsky, A., 'Introduction to microwave background polarization', New Astronomy Reviews, Volume 43, Issue 2-4, p. 157-168 **(1999)**

Kosowsky, A., 'The cosmic microwave background', Pub. Modern Cosmology 219-263 **(2002)**.

Kovac, J., et al., 'Detection of polarization in the CMB using DASI', Nature, 420..772K, **(2002)**

Lamarre, J.M., 'Photon noise in photometric instruments at far-infrared and sub-millimetre wavelength', Applied Optics, 25, pp. 870-876 **(1986)**

Lay, O.P., 'Phase Calibration and Water Vapor Radiometry for Millimeter-Wave Arrays', A&A Supplement series, Vol. 122, 547-557, **(1997)**

Liddle, A. "Fingerprinting the Universe - future CMB experiments," Contemporary Physics, 39(2) 95, **(1998)**

Mather, J C, 'Bolometer noise: non-equilibrium theory', Appl. Opt. 21, 1125, **(1982)**

Mauskopf, P.D., private communication **(2002)**

Mauskopf, P.D., 'Sensitivity of direct-detector interferometers compared to focal plane arrays', submitted (preprint) to Elsewier Science **(2003)**

Mauskopf, P.D., Bock, J.J., Del Castillo, H., Holzapfel, W.L., Lange, A.E., 'Composite infrared bolometer with Si3N4 micromesh absorbers ', Applied Optics, 36, pp. 765-771, **(1997)**

Nakajima, T., "Sensitivity of a ground-based infrared interferometer for aperture synthesis imaging", PASP, 113, 1289, **(2001)**

Netterfield, C.B., et al., 'A measurement by BOOMERANG of multiple peaks in the angular power spectrum of the cosmic microwave background', Astrophys. J., 571..604N, **(2002)**

Page, L., et al., 'WMAP Observations: Interpretation of the TT and TE Angular Power Spectrum Peaks', Astrophys. J. Suppl., 148..233P, **(2003)**

Penzias, A.A., Wilson, R.W., Astrophys. J. 142:419-421, **(1965)**

Philhour, B. J., 'Measurement of the Polarization of the Cosmic Microwave Background', PhD thesis, Caltech **(2002)**

Philhour, B.J., 'The Polatron: A Millimetre-Wave Cosmic Microwave Background Polarimeter for the OVRO 5.5 m Telescope', astro-ph/0106543, **(2001)**

Piccirillo, private communication

Polnarev, A.G., Sov. Astro., 29, 607, **(1985)**

Pooley, G.G., URSI/IAU Symp., Radio Astronomical seeing, IAP, Beijing, p. 64, **(1990)**

Richards, P L, 'bolometer for infrared and millimetre waves', J. Appl. Phys. 76-1, **(1994)**

Rieke, G., 'Detection of Light from the UV to the sub-millimetre', 2nd ed., ISBN #0-521-01710-6, **(2003)**

Roddier F., Ridgway S. T., 'Filling factor and Signal-to-noise ratio in optical interferometric array', PASP, 111:990-996, **(1999)**

Sachs , R.K., Wolfe, A.M., Astrophys.J., 147, 73, **(1967)**

Seljak, U., Zaldarriaga, M., 'Signature of Gravity Waves in the Polarization of the Microwave Background'. Phys. Rev. Let., 78:2054-2057 **(1997)**

Silk, J., Nature, 215:1155, **(1967)**

Spergel, D.N., et al., 'First-Year WMAP Observations: Determination of Cosmological Parameters', Astrophys. J. Supp., 148..175S , **(2003)**

Smoot, G. F., et al., 'Structure in the COBE differential microwave radiometer first-year maps', Astrophys. J., 396:L1, **(1992)**

Sunyaev, R.A., Zel'dovich, Ya. B., 'The Observations of Relic Radiation as a Test of the Nature of X-Ray Radiation from the Clusters of Galaxies', Comments on Astrophysics and Space Physics, Vol. 4, p.173, **(1972)**

Tango, W.J., Twiss, R.Q., 'Michelson Stellar Interferometry', prog. Opt., 17, 239-277, **(1980)**

Tegmark, M., http://www.hep.upenn.edu/~max/index.html

Tegmark, M., Efstathiou, G., 'A method for subtracting foregrounds from multi-frequency CMB sky maps', MNRAS, 281:1297T **(1996)**

Tegmark, M., et al., 'Foregrounds and forecasts for the CMB', Astrophys. J., 530:133T-165, **(2000)**

Thompson, Moran, Swenson, "Interferometry and Synthesis in radio-astronomy", ISBN 1-57524-087-4, **(1998)**

Toffolatti et al., 'Foreground contributions to 0.2-2° CMB anisotropies', Astrophys. Lett. & Comm, 32:125T , **(1995)**

Traub, W.A., 'Combining beams from separated telescopes', Applied Optics, Vol.25, No4, **(1986)**

White, G.K., 'Experimental Techniques in low-temperature physics', Oxford science publication', 3rd ed. **(1968)**

White, M.J., Srednicki, M., 'Window Functions for CMB experiments', Astrophys.J.443:6, **(1995)**

White, M.J., Hu, W., 'The Sachs-Wolfe effect', Astron. Astrophys., 321:8-9, **(1997)**

White, M.J., Scott, D., Silk, J., 'Anisotropies in the cosmic microwave background', Annu. Rev. Astron. Astrophys. 1994. 32: 319-70, **(1994)**

White, M.J., et al., 'Interferometric observation of CMB anisotropies', Astrophys. J., 514:12, **(1999)**

Wilson, R.N., 'Reflecting Telescope optics I', A&A library, ISBN-3540589643, **(1996)**

Zaldarriaga, M., 'Fluctuations in the cosmic microwave background', PhD thesis, Massachusetts Institute of Technology, **(1998)**

Zmuidzinas, J., 'Cramer–Rao sensitivity limits for astronomical instruments: implications for interferometer design', J. Opt. Soc. Am. A/Vol. 20, No. 2 **(2003)**